

Phase-resolved investigation of fast third-order
optical nonlinearities in photonic devices at
telecommunication wavelengths

Von der Fakultät der Mathematik und Physik
der Gottfried Wilhelm Leibniz Universität Hannover

zur Erlangung des Grades

Doktor der Naturwissenschaften

Dr. rer. nat.

genehmigte Dissertation

von

M.Sc. Anatoly Sherman

geboren am 19.05.1978 in Beltsy

2010

Referent: Prof. Dr. Uwe Morgner

Korreferent: Prof. Dr. Piet. O. Schmidt

Tag der Promotion: 08.11.10

Abstract

Photonic devices are widely used in optical communication systems and all-optical switching in roles of waveguides, multiplexers, interconnectors, wavelength converters, and others. By designing these devices, characterization of its third-order optical nonlinearities, such as nonlinear refractive index n_2 and nonlinear absorption β , is very important. For example, for use of optical fibers in telecommunication branch, it is desirable to have insignificant nonlinearities in order to transfer data with minimum distortion. On the other hand, optical fibers with high optical nonlinearities are often beneficial when building a laser system. The determination of the nonlinear properties of on-chip photonic devices due to fast optical nonlinearities, particularly nonlinear figure-of-merit ($n_2/\beta\lambda$, λ : wavelength), is highly important for high bit rate data transfer. There are various methods to measure third-order optical nonlinearities, but few of them allow measurements of n_2 and β simultaneously. In addition, many of these methods are not applicable to optical waveguides, since they are based on transversal effects. A further disadvantage of most approaches is the dependence on laser parameters, such as pulse profile.

The purpose of this research is to develop a versatile tool for investigation of fast optical third-order nonlinearities that is also applicable to waveguiding devices. The tool relies on the following ideas. Using a four-wave mixing scheme, a nonlinear mixing product is generated in the waveguide and is phase sensitively detected by employing a heterodyne technique. Phase-sensitive detection allows, in principle, simultaneous measurement of n_2 and β . The problem of such absolute measurements is the dependence on laser parameters and the comparison of the complex nonlinear field to the excitation fields. For these reasons, the complex nonlinear field from the waveguide under test is compared with the nonlinear field from a bulk sample with well known optical properties. Both mixing products from the waveguide and the bulk samples are generated simultaneously and under the same experimental circumstances. Depending on the longitudinal position of the bulk relative to the imaged spot from the waveguide's output, the nonlinear contribution from the bulk sample changes. By this procedure, the mixing products from both samples can be directly compared to each other. The tool allows for direct deduction of the nonlinear figure of merit in all-photonic devices and for measurements of weak optical nonlinearities, for example, in a short piece of hollow-core photonic crystal fiber.

Key words: Third-order optical nonlinearities, Four-wave mixing, Heterodyne detection

Zusammenfassung

Photonische Bauelemente finden Anwendung in optischen Kommunikationssystemen und rein optischen Schaltern, z.B. als Wellenleiter, Multiplexer oder Wellenlängenkonverter. Bei der Entwicklung photonischer Komponenten spielt die Charakterisierung ihrer optischen Nichtlinearitäten dritter Ordnung, d.h. des nichtlinearen Brechungsindex n_2 und der nichtlinearen Absorption β , eine wichtige Rolle. Beim Einsatz von Glasfasern im Telekommunikationsbereich ist es z.B. wünschenswert, geringe Nichtlinearitäten zu haben, um die Daten mit minimaler Verzerrung zu übertragen. Auf der anderen Seite sind z.B. bei der Weißlichterzeugung optische Fasern mit starken optischen Nichtlinearitäten erwünscht. Die Bestimmung der schnellen nichtlinear-optischen Eigenschaften On-Chip-photonischer Bauelemente, vor allem den nichtlinearen Figure-of-Merit ($n_2/\beta\lambda$, λ : Wellenlänge) ist sehr bedeutsam für die hoch-bitratige Datenübertragung. Es gibt unterschiedliche Methoden zur Messung optischer Nichtlinearitäten dritter Ordnung, aber nur mit wenigen davon können n_2 and β gleichzeitig gemessen werden. Außerdem sind viele dieser Methoden nicht anwendbar, um Nichtlinearitäten in optischen Wellenleitern zu bestimmen, da sie auf transversalen Effekten beruhen. Ein weiterer Nachteil der meisten Ansätze ist die explizite Abhängigkeit von Laserparametern, wie z.B. dem Impulsprofil.

Ziel dieser Arbeit ist die Entwicklung einer Messtechnik für die Untersuchung von schnellen optischen Nichtlinearitäten dritter Ordnung, die auch für Wellenleiter geeignet ist. Die entwickelte Messtechnik basiert auf folgenden Grundideen. Mittels Vierwellenmischung werden im Wellenleiter Mischfelder erzeugt und mit Hilfe der phasensensitiven Heterodyntechnik detektiert. Heterodyndetektion ermöglicht im Prinzip eine simultane Bestimmung von n_2 und β . Problematisch bei einer solchen Absolutmessung ist die oben erwähnte Abhängigkeit von den Laserparametern sowie der Vergleich der komplexen Amplitude des Mischsignals mit denen der Anregungsfelder. Aus diesem Grund wird die Amplitude und Phase des Mischfeldes aus der untersuchten Wellenleiterprobe auf die Amplitude und Phase des Mischfeldes aus einer Bulkprobe mit bekannten optischen Eigenschaften bezogen. Beide Mischfelder aus dem Wellenleiter und der Bulkprobe entstehen hierbei simultan und unter den gleichen experimentellen Umständen. Durch longitudinale Verschiebung der Bulkprobe relativ zu einer 1:1-Abbildung der aus dem Wellenleiter austretenden Strahltaile wird das Mischfeld aus der Referenzprobe variiert. So können die Mischfelder aus den beiden Proben separiert und schließlich miteinander verglichen werden. Die Messtechnik ermöglicht eine direkte Bestimmung von nichtlinearem Figure-of-Merit in

rein optischen Komponenten (all-photonic devices) und Messungen von sehr kleinen Nichtlinearitäten, z.B. in einem kurzen Stück Hohlkernfaser.

Schlagwörter: Optische Nichtlinearitäten dritte Ordnung, Vier-Wellen-Mischung, Heterodyn-Detektion

Table of Contents

1. Background and thesis structure	8
1.1 Background	8
1.2 Thesis structure	11
2. Introduction	12
3. Experimental setup	22
3.1 Setup for nearly-degenerate FWM	22
3.2 Heterodyne detection	28
3.3 Measurement of waveguide's nonlinearity using heterodyning	40
3.4 Technique for elimination of the parasitic signal when investigating weak optical nonlinearities	44
3.5 Summary & Conclusion	54
4. Referencing to a Bulk Sample: Investigation of third-order nonlinearities in waveguides, independent of laser parameters	56
4.1 Summary & Conclusion	66
5. Experimental demonstration of ReBuS	68
5.1 Experimental results for waveguides	69
5.2 Phase-resolved concept	76
Precis	83
Outlook	85
References	88

Chapter 1

Background and thesis structure

1.1 Background

The field of nonlinear optics has been known for more than 50 years. One of the first experiments in this field was performed by Franken and co-workers in 1961 [Fran61]. Since then, a number of nonlinear optical effects were observed and extensively studied. An observation of the change of refractive index of a material as a result of light-matter interaction and thereby the influence of light on itself were published back in the sixties [e.g. Bass62, Eckh62, Terh62, Gior65, Stol78]. It is not a coincidence that progress in investigation of nonlinear optical effects is related to the progress in laser science. A first demonstration of a nonlinear effect was performed shortly after the first laser was implemented [Maim60].

The fast development in nonlinear optics opens a gate to many applications in the field of nonlinear spectroscopy and material science. A revolutionary event for the communication industry happened in 1966 when Kao and Hockham promoted the idea to reduce the losses in an optical fiber to below 20 dB/km [Kaoh66]. With the growth of low loss glass fibers in the seventies [Kapr70, Payn74, Miya79], the transmission of information by light over long distances became feasible. Today, the standard wavelength range for this purpose is 1500 nm to 1600 nm with losses as low as 0.2 dB/km [Corn01].

Nonlinear optics has generated new fields of research in the past and continues to do so. For example, a relatively recent invention of a new type of fiber [Knig98], where dispersion and nonlinear effects can be designed depending on the fiber microstructure, has been extensively employed and has a high potential for the communication branch [Creg99, Knig98].

The photonic crystal fiber (not to be confused with a fiber made from crystalline material) is a type of optical fiber that is based on the properties of photonic bandgap [Knig98 Russ06]. It obtains its waveguide properties from an arrangement of very small structures with different index of refraction, e. g. air holes, which are located along the whole fiber. The ability to design the waveguide's properties, such as dispersion and attenuation, depending on the air holes' size, shape and location in the waveguide is a significant advantage over standard (step-index) optical fiber.

Hollow-core photonic crystal fiber (HC-PCF) is a type of fiber that guides most of the light in air [Creg99, Humb04]. Due to this fact, HC-PCF has very weak optical nonlinearities compared to standard fibers or solid-core photonic crystal fibers. HC-PCFs can be produced from different types of materials, i.e. fused silica or polymer material [Smit03, Argy06]. This type of fiber is a promising candidate for various applications in linear and nonlinear optics, e.g. transmission of high-power optical signals for long distances without data distortion or fiber damages [Ouzo03], particles guidance [Renn99], highly sensitive sensors [Rita04], THz applications [Vinc09], high-power supercontinuum generation [Song10], and guiding of UV radiation [Fevr09].

Photonic devices are employed in the fields of telecommunication branch and all-photonic signal processing (i.e. based on silicon-on-insulator SOI). They perform diverse functionalities like waveguiding, switching, interconnecting, multiplexing, add drop filtering, and wavelength conversion [Alme04, Cott99, Dinu03, Gopi04, Tsan02]. For different applications, different strengths of nonlinearity are desired: for light-by-light guiding (all-photonic switching), a strong nonlinearity is required, whereas for long haul transmission the nonlinearity should be as weak as possible.

Since optical technologies enable high bit rates compared to other technologies, most data will be transferred by light. Currently, the speed of data transmission per wavelength channel is dozens of Gb/s and it is growing continually [Koos09, Rams09]. To transmit the data with

high speed, it is desirable to have devices that respond fast enough to the short light pulses. Therefore, an investigation of fast optical properties of these devices is so important.

1.2 Thesis structure

The thesis is structured as follows:

An introduction to different types of third-order optical nonlinearities and a few commonly existing methods for their measurements are provided in chapter 2. Several mechanisms for nonlinear optical interactions are explained and the parameters describing the third-order optical processes are presented.

Setup for measurement of fast third-order nonlinearities is developed and implemented. In section 3.1 a configuration for measuring nonlinearities by means of a nearly-degenerate four-wave mixing (FWM) generation is discussed. Heterodyne scheme for discrimination of the nonlinear (FWM) signal against the excitation fields is shown in section 3.2. Measurement of optical nonlinearity using heterodyning is demonstrated for waveguide in section 3.3. When investigating waveguide samples of a length $\approx 10\text{-}20$ mm, different parasitic signals can hamper the detection. In section 3.4 a technique for elimination of the concurrent parasitic signal is developed.

In chapter 4 a concept of Referencing to a Bulk Sample (ReBuS) is explained. ReBuS allows detection of optical nonlinearities by direct comparison with additional sample and without measuring the laser parameters, such as peak amplitudes of the excitation fields.

In section 5.1 ReBuS combined with heterodyning is experimentally demonstrated by employing two types of waveguide samples. In section 5.2 the concept for phase-resolved detection of fast optical nonlinearities that allows deduction of nonlinear-figure of merit, is demonstrated.

Chapter 2

Introduction

The time scale of the nonlinear response can change from at least milliseconds to femtoseconds or less [Boyd92], depending on the nature of the nonlinearity. The fastest mechanism¹ for nonlinear interaction is due to nonresonant electronic nonlinearity that has a response time of sub-femtoseconds.

We deal with fast optical nonlinearities, i.e. nonlinearities that have response time much smaller than the pulse duration, so that it can be assumed that the medium responds instantaneously to the applied field. Nonlinear optical effects can be described by a power series of the dielectric polarization [Arms62]:

¹ Other mechanisms are slower. For example, the response time of the process due to molecular orientation is of the order of 10^{-12} s [Boyd92]. The response time due to electrostriction is 10^{-9} s to 10^{-10} s [Boyd92]. There are other mechanisms that are responsible for optical nonlinearities, e.g. photorefraction. The dynamics of this process is even slower, of about 0.1 s to 10 s.

$$\tilde{P} = \chi^{(1)}\tilde{E} + \chi^{(2)}EE + \chi^{(3)}EEE + \dots \quad (2.1)$$

where \tilde{P} is a dielectric polarization, E is an applied field, and coefficients $\chi^{(i)}$ are the susceptibilities of order i of the medium. The terms that are proportional to an even power of the susceptibility coefficients vanish for materials with inversion symmetry whereas nonlinear effects associated with odd powers of the susceptibility occur in all materials. Therefore, processes due to the susceptibility of the third-order $\chi^{(3)}$, which is the lowest odd order of the optical nonlinearity, are so interesting for investigation. In Eq. (2.1), the third-order susceptibility $\chi^{(3)}$ is treated as a scalar quantity.

The nonresonant electronic nonlinearity is due to the nonlinear response of the bound electron as a result of an applied optical field. The nonlinearity is not particularly large relative to other types of the nonlinearities [Boyd92]; however it occurs in any dielectric material. In a classical picture, the recovery time of this process is estimated to be the time the electron needs to move around a nucleus, which is about 10^{-15} s to 10^{-16} s [Boyd92].

About linear and nonlinear processes

Linear absorption occurs when the frequency of the excitation field coincides with the resonance frequency of the medium. This is schematically shown in Fig. 2.1a. For nonlinear optical resonances, several frequencies are involved, so that the sum or difference of their frequencies equals the resonance frequency. In Fig. 2.1b the energy diagram due to the third-harmonic generation is shown. By employing a degenerate four-wave mixing scheme, the equivalent energy diagram is described by Fig. 2.1c. In degenerate four-wave mixing scheme, the frequencies of all involved fields in the nonlinear process are equal.

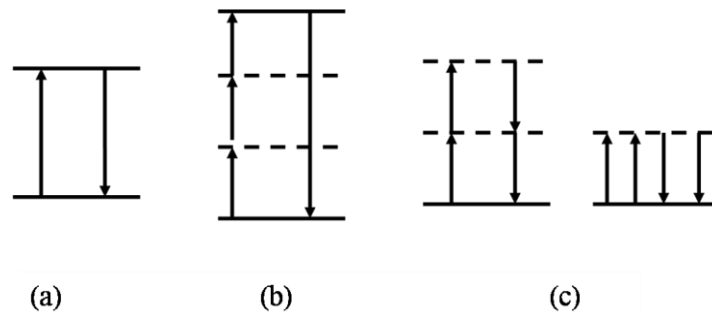


Fig. 2.1. (a) linear resonant process, (b) third-harmonic generation, (c) degenerate four-wave mixing process (FWM). By employing the degenerate four-wave mixing scheme, the frequencies are equal.

Resonant and nonresonant optical nonlinearities

Nonresonant optical nonlinearities occur far from resonances of the material and, as was mentioned, are very fast. For short enough pulses, only electronic nonlinearity contributes to nonlinear processes, since only electrons can follow the fast changes of the optical field. Resonant optical nonlinearities rapidly vanish far from the material resonance. For example, for fused silica, the resonances are in UV range, and the value of nonlinear refractive index n_2 is constant around wavelength of 1550 nm [Mila98]. Near material resonance, both nonlinear refractive index and nonlinear absorption are enhanced [Harb02].

Third-order nonlinear optical coefficients

Besides the linear properties of the photonic devices, its nonlinear properties are important if the functionality is based on nonlinear effect [e.g. Steg89, Gopi04]. The nonlinear properties are described by the nonlinear refractive index n_2 and the nonlinear absorption coefficient β , that are proportional to the real and imaginary parts of the third-order susceptibility, respectively ($n_2 = \text{Re}(\chi^{(3)})/n_0^2c$, $\beta = \text{Im}(\chi^{(3)})k_0/n_0^2c$, where n_0 - linear refractive index, c - speed of light, k_0 - wavenumber). In particular, the ratio of both, the so-called nonlinear figure-of-merit $\text{NFOM} = \frac{n_2}{\beta\lambda} = \frac{k_0 n_2}{\beta} \frac{1}{2\pi}$, where λ is a wavelength, is widely used as a criterion for selecting suitable, low-loss materials for on-chip optical switching devices [e.g. Lenz00, Dinu03, Gopi04]. The dimensions of n_2 and β are m^2/W and m/W , respectively, since the intensity dependent refractive index change is $\Delta n = n_2 I$ (I is intensity in W/m^2) and the nonlinear loss due to nonlinear absorption is $\Delta\alpha = \beta I$ ($\Delta\alpha$ in m^{-1}).

The definition of NFOM comes from the following equation [Lenz00]:

$$\varphi_{NL} = \frac{k_0 n_2}{\beta} \cdot \ln(1 + \beta IL) = \text{NFOM} \cdot 2\pi \cdot \ln(1 + \beta IL) \quad (2.2)$$

where φ_{NL} is a nonlinear phase that is accumulated as a result of nonlinear interaction of light, L is a length of the device under the test, and I is an initial peak optical intensity. Eq. (2.2) is obtained by solving the equations $\frac{dI}{dz} = -\beta I^2$ and $\frac{d\varphi_{NL}}{dz} = k_0 n_2 I$. A nonlinear transmission can be defined from Eq. (2.2) as $T_{NL} = 1/(1 + \beta IL)$. The purpose in designing a nonlinear material is to have high value n_2 and low value of β , i.e. having NFOM as high as possible, since unwanted nonlinear losses are associated with nonlinear absorption β [Harb02]. Fig. 2.2 shows NFOM as a function of $1 - T_{NL}$ (in percent), which gives an intuition of how the value of NFOM is chosen. For instance, by designing a device that has a (nonlinear) phase accumulation π with $1 - T_{NL}$ of 0.2 (20 %), an NFOM of about 2 is required. Allowing the same nonlinear transmission for $\varphi_{NL} = 2\pi$, a higher NFOM (5) is required. Usually, an NFOM of more than 3 is desired for all-photonics switching applications. Although, SOI (silicon-on-insulator) does not have high NFOM (0.3 ~ 0.8 [Dinu03, Tsan02, Linz07]), silicon material is still an attractive candidate for telecommunication wavelength, due to the high compatibility with microelectronics [e.g. Sore06, Dekk07, Witz10].

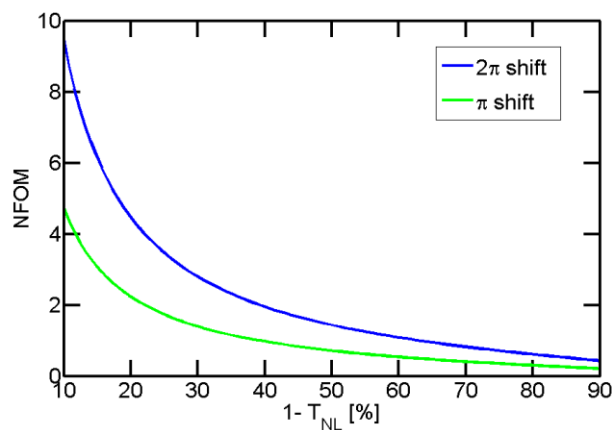


Fig. 2.2. Nonlinear Figure of Merit (NFOM) as a function of $1 - T_{NL}$ for phase accumulations $\varphi_{NL} = \pi$ and $\varphi_{NL} = 2\pi$. The large phase accumulations are due to high peak optical intensity or long lengths. For small nonlinear absorption NFOM is large.

For $\beta IL \ll 1$, Eq. (2.2) is simplified to

$$\varphi_{NL} = k_0 n_2 I L = n_2 L \frac{k_0 P}{A_{\text{eff}}} \quad (2.3)$$

where A_{eff} describes the spatial distribution of the light on the sample, i.e. A_{eff} is mode field area², and P is a peak optical power³.

For optical fiber waveguides, the nonlinear coefficient γ [Agra89] is broadly exploited to determine their optical nonlinearities. From Eq. (2.3) the nonlinear coefficient γ is defined as

$$\gamma = n_2 k_0 / A_{\text{eff}} \quad (2.4)$$

By solving the propagation equation for optical fiber waveguides, the nonlinear term due to the four-wave mixing (FWM) process is given by [Stol82, Agra89]

$$E_{\text{FWM}} = \gamma E_1^2 E_2 L \quad (2.5)$$

where E_1 and E_2 are the peak amplitudes of the excitation fields, E_{FWM} is the amplitude of the (FWM) nonlinear process, and L is the length of the fiber. Eq. (2.5) shows that in order to determine the nonlinear coefficient γ , one has to measure the peak amplitudes of the excitation fields. In this work, the measured parameters are γ or n_2 for optical fibers and nonlinear figure-of-merit for samples with non-negligible nonlinear absorption.

² This term is used for optical fibers.

³ Intensity is related to the power by $I = P / A_{\text{eff}}$.

Existing methods for measurements of the nonresonant optical nonlinearities

Many methods have been developed to characterize nonresonant third-order optical nonlinearities [e.g. Bloe06, Hein97, Kato95, Malo98, Sami10, Sarg94, Shei89]. The merit of a method depends on specific property that is measured and on nature of the nonlinearity. Not all methods are applicable for all types of photonic devices. A few of the commonly used experimental methods: four-wave mixing, interferometry, and z -scan are briefly discussed.

By the measurements mentioned below, the peak amplitudes of the excitation fields are measured for the determination of nonlinear optical coefficients in waveguides. However, it is not an easily measurable quantity, since it requires characterizing of the laser pulse. The z -scan method is applied for the measurements of nonlinearities in bulk materials. Additionally, to be able to detect both n_2 and β simultaneously, the phase of the nonlinear field relative to the excitation fields has to be measured.

Four-Wave Mixing

Four-Wave Mixing (FWM) is a nonlinear parametric process in which excitation fields with three different frequencies ν_1 , ν_2 and ν_3 interact with the material via its third-order susceptibility $\chi^{(3)}$. As a result, new fields at frequencies $\pm \nu_1 \pm \nu_2 \pm \nu_3$ are generated. The ν_1 , ν_2 and ν_3 have different optical frequency (nondegenerate FWM), i.e. frequency difference between the fields is in THz range [e.g. Thie01]. Phase-matching three different laser wavelengths in an experiment is not practical. Self-focusing and cross-phase modulation (XPM) are special cases of FWM with the same optical frequencies (Fig. 2.1c). Nearly degenerate four wave mixing is a nonlinear process, in which the three excitation fields have nearly the same optical frequency, so that $\nu_3 - \nu_2, \nu_2 - \nu_1 \ll \nu_1, \nu_2, \nu_3$. This means that Fig. 2.1c also describes the nearly degenerate FWM. The nonlinear coefficient γ is extracted by measuring the peak amplitudes of the excitation fields, the generated FWM field, and the length of the sample.

Interferometry

A typical approach is to put a sample in one path of the arms of an interferometer and to observe an interference fringe distortion [e.g. Mora75, Webe78]. Due to the nonlinearity of the sample, the beam that propagates in the sample's arm experiences an intensity dependent phase delay relative to the second arm. As a result, the interference fringes are curved.

The interferometric methods usually provide high sensitivity, but they require a precise alignment and high quality fringes. However, to satisfy these conditions is not always easy. In addition, the measurement of peak amplitudes of the excitation fields is required.

Z-Scan

The z -scan method is based on self-focusing effect [Shei89]. One measures the transmittance of the nonlinear medium as a function of sample's z -position, as schematically shown in Fig. 2.3. A transversal change of the light in far-field is measured through a finite aperture. Further details are described in caption of Fig. 2.3.

The main advantage of the z -scan method is that it can measure both n_2 and β coefficients and is extensively employed for measurements of nonlinearities in bulk materials. Due to spatial variation of the beam, z -scan is not applicable for measurements of optical nonlinearities in waveguides.

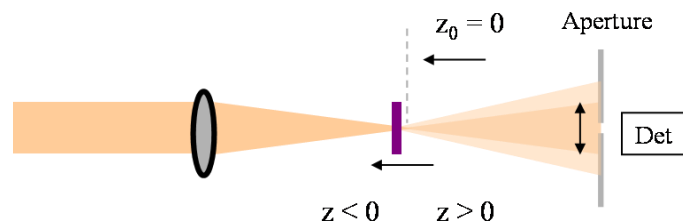


Fig. 2.3. Schematic setup of the z -scan method. *Transversal* change of the beam as a result of the self-focusing effect is detected through the aperture. Let us assume that the sample has a positive nonlinear refractive index. When the sample is located far from the focus, a normalized transmittance ($T(z)/T(z \gg z_0)$) remains constant. When the sample is located in the vicinity of the focus, but ahead of it ($z < 0$), the self-focusing effect collimates the beam and leads to decreased transmittance measurement. By shifting a sample to $z > 0$ and staying in vicinity of the focus, the beam collimation results in increase of the measured transmittance.

Z-scan, self-focusing and fully degenerate four wave mixing

If all of the excitation fields have the identical frequency ($\nu_1 = \nu_2 = \nu_3$), this process is called (fully) degenerate four-wave mixing (DFWM) [Fish83]. The disadvantage of DFWM is that in order to discriminate between the fields without measuring the transversal change of the beam, the involved fields have to have a non-collinear geometry. Therefore, DFWM is not

suitable for measurement of optical nonlinearities in waveguides, since in waveguides all fields co-propagate. For collinear geometry of DFWM, the excitation and nonlinear fields can be physically distinguished only by transversal effects.

The self-focusing is a fully degenerate four wave mixing so that the prominent z -scan method is based on fully degenerate FWM. Waveguiding samples have the same beam profile along the propagation axis, as schematically shown in Fig. 2.4. In waveguide, except the fact that shifting the waveguiding sample along the propagation direction is not practical, the transversal beam change of the nonlinear signal is suppressed by waveguiding mechanism. Therefore, the measurements that are based on transversal changes are not suitable for measurements of optical nonlinearities in waveguides.

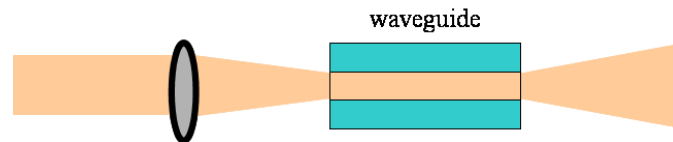


Fig. 2.4. Waveguide has the same beam profile along the propagation axis. Methods that are based on the transversal beam changes are not applicable for waveguides.

Nearly degenerate four wave mixing

In this work, the nearly degenerate four wave mixing is defined as a process, at which two of the excitation fields have equal frequency $\nu_1 = \nu_3$, and the third excitation field has a frequency ν_2 , which is close to ν_1 so that $\nu_2 - \nu_1 \ll \nu_1, \nu_2$. The excitation fields at frequencies ν_1 and ν_2 generate nonlinear FWM products at side lobes frequencies of $2\nu_1 - \nu_2$ and $2\nu_2 - \nu_1$. Sometimes the above described process is called a nearly degenerate three wave mixing, since signals at three different frequencies are involved in this process ($\nu_1, \nu_2, \nu_{\text{FWM}}$). Due to the small frequency difference ($\nu_2 - \nu_1 \ll \nu_1, \nu_2$) the nearly-degenerate FWM process is phase matched [Sto182].

The benefit of the nearly-degenerate FWM upon the nondegenerate-FWM is that the fields are phase matched. However, due to the practically equal optical frequency difference between the involving waves, it is usually a formidable task to separate the newly generated signals [e.g. Suth96]. The benefit of the nearly-degenerate FWM upon the fully-DFWM process is that the collinear geometry can be employed [e.g. Malo98]. Therefore, the nearly-degenerate FWM allows for the investigation of the waveguide samples [e.g. Hofm96, Borr99].

To sum up

For the determination of the fast nonresonant optical nonlinearities by commonly employed methods, it is necessary to measure the laser parameters, such as peak amplitudes of the excitation fields. Z-scan method is based on self-focusing and not suited for waveguide characterization. The nearly-degenerate FWM process is applicable for investigation of nonlinearities in waveguides. The coefficients, such as nonlinear refractive index and nonlinear absorption coefficient are presented. The nonlinear figure-of-merit is important parameter for all-photonic devices. A few frequently employed measurement techniques: interferometry, z-scan, and four-wave mixing, as well their main advantages and drawbacks are discussed.

Chapter 3

Experimental setup

This chapter treats the design and implementation of the experimental setup for investigation of nonlinearities in waveguides. In section 3.1 the configuration for measurements of nearly-degenerate FWM by collinear geometry is discussed. In section 3.2 a heterodyne technique that allows to discriminate a FWM signal is shown. The experimental demonstration of the FWM with heterodyning is presented by employing a short piece of fiber in section 3.3. A novel technique that allows measurements of weak optical nonlinearities, i.e. in hollow-core waveguides, is developed. This is discussed in section 3.4.

3.1 Setup for nearly-degenerate FWM

Laser system

The laser system is schematically shown in Fig. 3.1. The fiber cavity includes an Erbium-doped fiber, which has a normal dispersion ($D = -22$ ps/(nm·km), D - dispersion parameter)

and two fibers with anomalous dispersion; SMF-28 ($D = +18 \text{ ps}/(\text{nm}\cdot\text{km})$) and Flexcor 60 ($D = 5.5 \text{ ps}/(\text{nm}\cdot\text{km})$). The fiber oscillator is pumped by a 980 nm fiber pigtailed laser diode through the 980/1550nm-wavelength-division-multiplexer (WDM). To control the passive mode-locking mechanism, two polarisation controllers are inserted to manipulate the light polarisation [Hund06]. A Faraday isolator provides for unidirectional operation. The average output power of the laser oscillator is about 12 mW.

To increase the output power of the laser system, an Erbium-doped fiber amplifier (EDFA) with identical components is placed behind the oscillator. A 99:1-coupler is inserted in the first stage of the amplifier system for diagnostic output of the signal coming from the oscillator. The pumping of the Erbium-doped fiber occurs in the amplifier in propagation direction. This is achieved with the help of a pump-diode and via a 980-1550 WDM-coupler. Two polarization controllers are inserted behind the 99:1-coupler and behind the Erbium-doped fiber to ensure the maximal amplification.

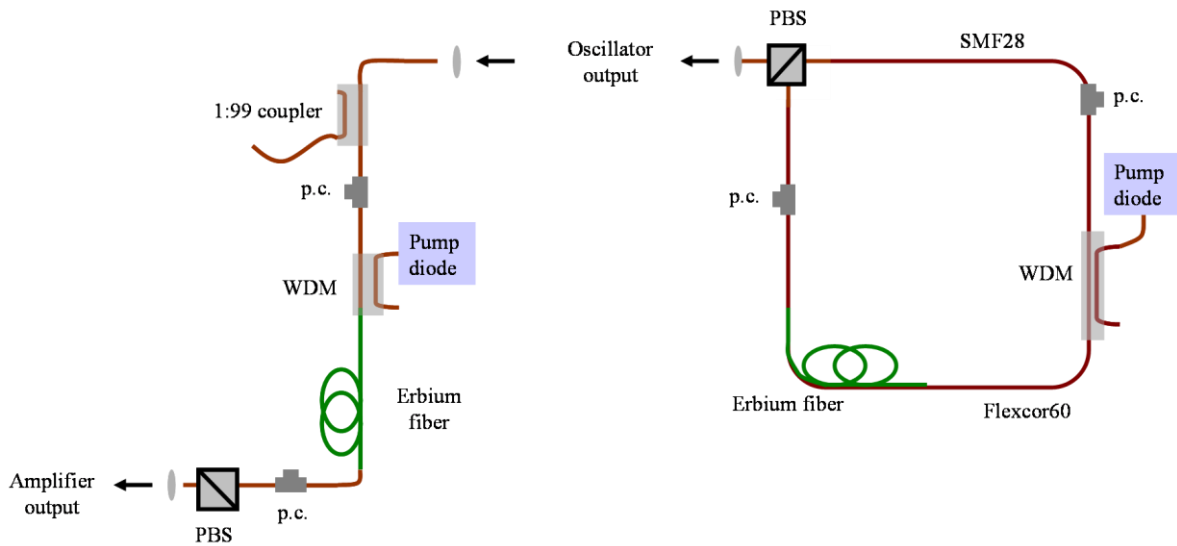


Fig. 3.1. Right: experimental setup of the Erbium-doped oscillator. Left: experimental setup of the Erbium-doped amplifier. p.c. – polarization controller, PBS – polarization beam splitter, iso – Faraday isolator, WDM - 980/1550 nm wavelength division multiplexer, the pump diode operates at at 980 nm.

The laser system delivers a frequency comb with a central wavelength of $\lambda_0 = 1580 \text{ nm}$. The average optical power of the 100 fs pulses after amplification is 50 mW and the repetition rate (f_r) is 56 MHz. The measured interferometric autocorrelation is shown in Fig. 3.2. The spectrum of the laser behind the Erbium-doped fiber amplifier (EDFA) is shown in Fig. 3.3 and its spectral width is about 40 nm. Short pulses are highly desirable since the nonlinear

optical signal is enhanced with the optical peak power. The laser medium in this work is Erbium-doped fiber [Mear87]. A fiber diode-pumped laser system is employed around the wavelength of 1580 nm. The mode-locking of the laser occurs passively and is based on the nonlinear polarization rotation [Tamu93].

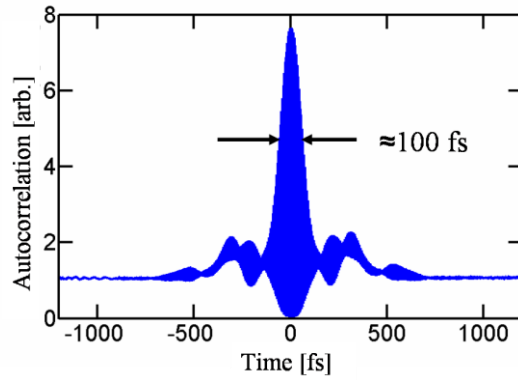


Fig. 3.2. Autocorrelation function of amplified pulses as measured behind the EDFA and acousto-optical modulator. The “pedestal” is due to the higher dispersion terms of the acousto-optical modulator. Pulse duration of about 100 fs is obtained.

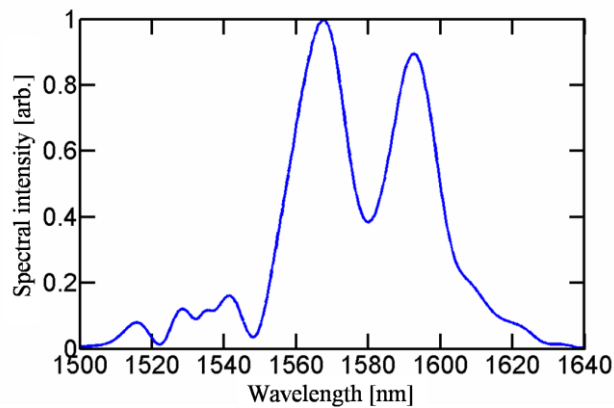


Fig. 3.3. Output spectrum behind the laser system.

Nearly-degenerate FWM

As was mentioned in chapter 2, for the nearly-degenerate FWM process, two excitation fields with similar optical frequencies ν_1 and ν_2 are used. The excitation fields with frequency difference in MHz range are produced by acousto-optical modulators (AOMs). The spectrum of the laser with the optical carrier frequency ν_0 is slightly shifted to new frequencies of $\nu_1 = \nu_0 + 63.351$ MHz and $\nu_2 = \nu_0 + 46.649$ MHz, respectively.

As a result of the modulation between the excitation fields, sidebands at the frequencies $\nu_1 + (\nu_1 - \nu_2)$, $\nu_1 - (\nu_1 - \nu_2)$ and $\nu_2 + (\nu_1 - \nu_2)$, $\nu_2 - (\nu_1 - \nu_2)$ are developed. The distinguishable frequency components, i.e. those different from the frequencies of the excitation fields, are two FWM products at $\nu_{\text{FWM}} = 2\nu_1 - \nu_2$ and $\nu_{\text{FWM2}} = 2\nu_2 - \nu_1$. The frequency components of the involved fields are shown in Fig. 3.4. The FWM product at lower frequency ($2\nu_2 - \nu_1$) might be referred to as Stokes and at higher frequency ($2\nu_1 - \nu_2$) as Anti-Stokes (this denotation is usually used in Raman scattering when the frequency difference $\nu_1 - \nu_2$ lies in the THz range [Hick86, Grev05]).

We concentrate on the detection of the nonlinear FWM product at frequency $\nu_{\text{FWM}} = 2\nu_1 - \nu_2 = 80.053$ MHz.

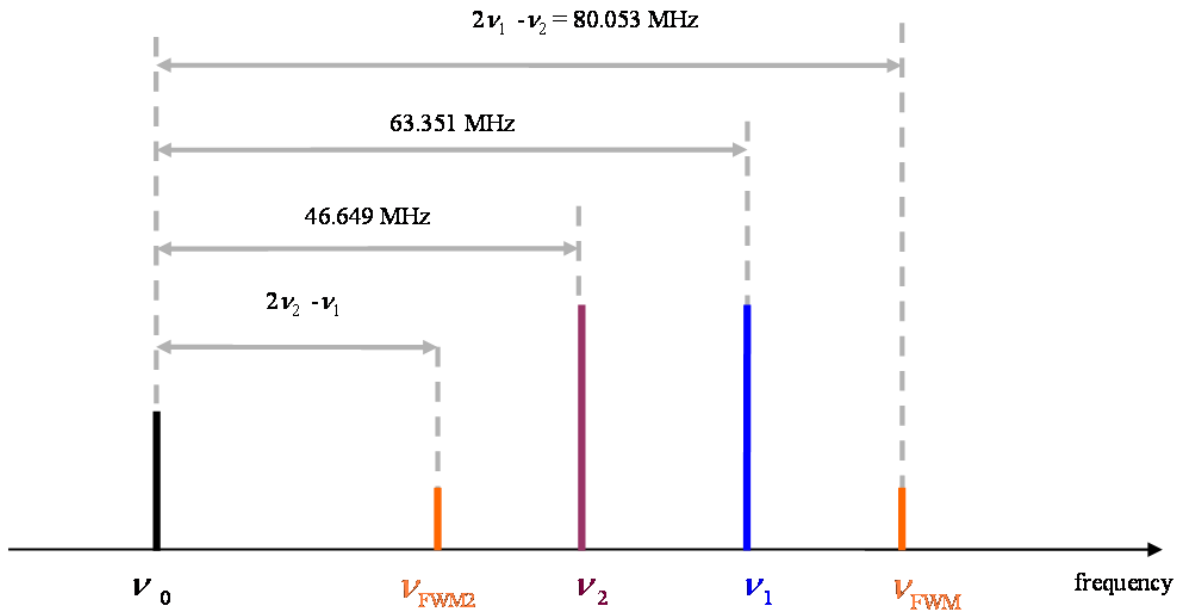


Fig. 3.4. Stick diagram of the involved frequencies. ν_0 is the frequency of the laser (corresponds to $\lambda_0 = 1580$ nm). ν_1 and ν_2 are frequencies of the excitation fields and ν_{FWM} and ν_{FWM2} are frequencies of the generated FWM products. We concentrate on FWM at $2\nu_1 - \nu_2$.

To investigate the optical nonlinearities in the waveguides, it is obligatory for all involved fields to propagate collinearly. For this purpose, a nearly degenerate FWM scheme is implemented and its setup is shown in Fig. 3.5. Two beams at excitation frequency ν_1 , ν_2 that are produced by AOM1 and AOM2 are launched into the sample and modulate the refractive index of the material with a frequency $(\nu_1 - \nu_2)$. A free space 35 dB Faraday isolator is employed to prevent the pulses going back into the laser system. This is important in order to avoid unwanted nonlinear effects in the laser system. To achieve a maximally efficient FWM, it is preferable for the excitation fields to have the same polarization. For this purpose, two half-wave plates and two polarizing beam splitters are inserted. The purpose of a half-wave plate that is placed in front of the polarizing beam splitter PBS1 is to regulate the magnitude of the optical power between arm1 and arm2 (Fig. 3.5). The reflected light from PBS1 enters arm1 and is linearly polarized, perpendicularly to the PBS1 plane of incidence. To obtain the same polarization in arm2 (Fig. 3.5), a similar procedure is employed: a half-wave plate behind PBS1 rotates the polarization of the transmitted light. The light is then reflected by PBS2 so that it has the same linear polarization in both arms. The light that passes through PBS2 is used in heterodyne scheme. The beams overlap spatially by using an unpolarizing beam splitter BS1. In addition to the spatial overlap of the beams, the pulses in both arms overlap temporally. For this purpose, a time delay device is inserted in one of the arms (T.D.1 in Fig. 3.5).

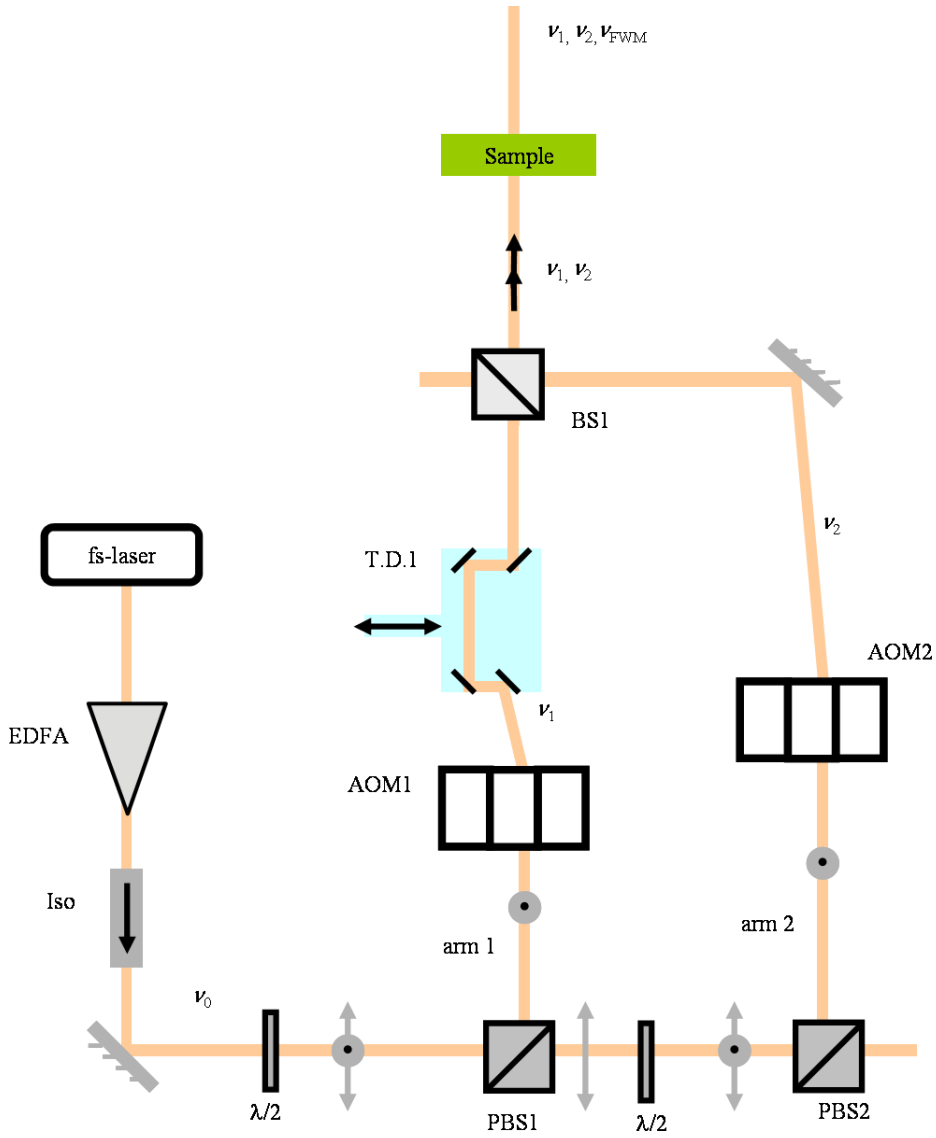


Fig. 3.5. Scheme of the experimental setup for a nearly degenerated FWM in collinear geometry. AOM-acousto-optic modulator. $\lambda/2$ -half-wave plate. T.D- time delay. BS- unpolarizing beam splitter. PBS- polarizing beam splitter. The excitation frequencies at ν_1 and ν_2 (frequency difference in MHz range) co-propagate and enter the sample. As a result of nonlinear interaction, a new frequency at ν_{FWM} is generated.

The phase matching condition is satisfied due to the small frequency difference between the involved fields. The use of the laser system with the short pulses and hence with higher peak amplitudes of the excitation fields (Eq. (2.5)) is preferable to increase the FWM signal. To achieve the optimally enhanced FWM product at $2\nu_1 - \nu_2$, the optical power between ν_1 and ν_2 is distributed with the ratio 2:1 (taking $P_1 + P_2 = 1$, the maximum for $P_1^2 P_2 = P_1^2 (1 - P_1)$ is obtained when $P_1 = 2/3$ and $P_2 = 1/3$).

3.2 Heterodyne detection

To detect the FWM product, it has to be separated from the excitation frequencies that are in MHz distance from ν_{FWM} . The spectral filtering of the generated FWM is carried out in the RF-regime⁴ rather than in the optical regime. This is done with the help of heterodyne principle [Sieg63]. Heterodyning can be described as a down-conversion of the optical signal to the RF range. It is performed with the help of the local oscillator, which has a similar, but not identical optical frequency as the frequency of the signal of interest. In “classical implementation”, the local, i.e. independent oscillator is generated using a different (*hetero* (Greek) - different) source from the source where the signal of interest is generated:

$$\text{Local oscillator: } E_{\text{LO}} \cos(2\pi\nu_{\text{LO}} t + \phi(t))$$

$$\text{Signal of interest: } E_{\text{sig}} \cos(2\pi\nu_{\text{sig}} t + \varphi(t))$$

where E is a (complex) amplitude, ν is a frequency, and $\phi(t)$ and $\varphi(t)$ are time-changing phases due to phase fluctuations of the local oscillator and source of the signal, respectively. The phase fluctuations have different statistics if the signal of interest and the local oscillator are generated using different sources. The amplitude of the local oscillator has an amplitude that is much larger (*dyn* (Greek) - power) than the amplitude of the signal, $|E_{\text{LO}}| \gg |E_{\text{sig}}|$.

Hence, by employing the heterodyne technique and detecting a beat note amplitude

$$E_{\text{sig}} E_{\text{LO}} \cos(2\pi(\nu_{\text{sig}} - \nu_{\text{LO}})t + \varphi(t) - \phi(t))$$

the signal is amplified, i.e. has heterodyne gain.

In my work, the local oscillator frequency is generated using the same laser source. Due to this fact, phase fluctuations are nearly the same for the nonlinear mixing product and the local oscillator fields and hence are common-mode-rejected⁵. This configuration is interpreted as interference between the FWM and the local oscillator fields, where both arms have identical optical path lengths, so that the local oscillator and the nonlinear signals are highly correlated. It is worth to note that if the local oscillator would have been generated by an independent

⁴ RF-regime - radio frequency regime, frequencies that are much lower than the optical frequencies.

⁵ Common-mode rejection - rejection of the fluctuations due to the same nature in both signals.

source, the former would noticeably contribute to the interferometric noise since both signals are not correlated.

By heterodyning between the local oscillator and the FWM signal at frequency ν_{FWM} , the detected optical power is given by

$$P_{\text{opt}} \propto |E_{\text{FWM}}|^2 + |E_{\text{LO}}|^2 + \text{Re}[E_{\text{FWM}}E_{\text{LO}}^*] \cos(2\pi(\nu_{\text{FWM}} - \nu_{\text{LO}})t) \quad (3.1)$$

where P_{opt} is the optical power and t is time. The first two terms in Eq. (3.1) are zero-frequency ‘DC’ terms and the third ‘AC’ term is the down-converted to RF frequency $\nu_{\text{FWM}} - \nu_{\text{LO}}$ term with the beat note amplitude $E_{\text{FWM}}E_{\text{LO}}$.

By employing the heterodyne technique, the signal is amplified. On the one hand, it is preferable to have large amplitude of the local oscillator to increase the beat note amplitude $E_{\text{FWM}}E_{\text{LO}}$. On the other hand, by increasing the power of the local oscillator, its laser amplitude noise increases as well and signal-to-noise ratio decreases. Ideally, the dominant noise should be due to the light of the signal of interest, i.e. due to the FWM. The FWM field co-propagates with the excitation fields. Therefore, the dominant noise is imposed to be due to the excitation fields, since their amplitudes are larger than the amplitude of the FWM (in this work several dozens of dB stronger). The local oscillator and excitation fields come from the same source, so the dominant noise is still due to the excitation fields if the amplitude of the local oscillator is comparable (selected criterion twice larger) than from the excitation fields.

The local oscillator has similar amplitude as the excitation fields so that on the one hand, the FWM product is enhanced by the local oscillator, and on the other hand, the noise caused by the local oscillator does not dominate.

Due to correlation between the local oscillator and FWM, the beat note at $\nu_{\text{FWM}} - \nu_{\text{LO}}$ has a narrow RF spectrum that merely reflects weak noise contributions from the AOM driving signals and from interferometric path length fluctuations, e. g. due to acoustics. Due to the correlation, any phase fluctuations of the optical carrier frequency of the laser are cancelled-out by this detection scheme.

The setup for heterodyne technique is shown in Fig. 3.6. The local oscillator frequency is slightly shifted in respect to the FWM signal frequency and the beat note between these two is detected. The light that passes through the polarizing beam splitter PBS2 is used for the local oscillator arm (arm3, Fig. 3.6). The optical carrier frequency ν_0 is shifted to $\nu_{LO} = \nu_0 + 80\text{MHz}$ with the help of the acousto-optical modulator AOM3. The polarization of the local oscillator field is adjusted to be the same as the polarization of both excitation fields by using a half-wave plate. For the temporal overlap with the four-wave mixing pulses, a time delay device (T.D.2) is inserted into the arm of the local oscillator. Both beams spatially overlap on the beam splitter BS2.

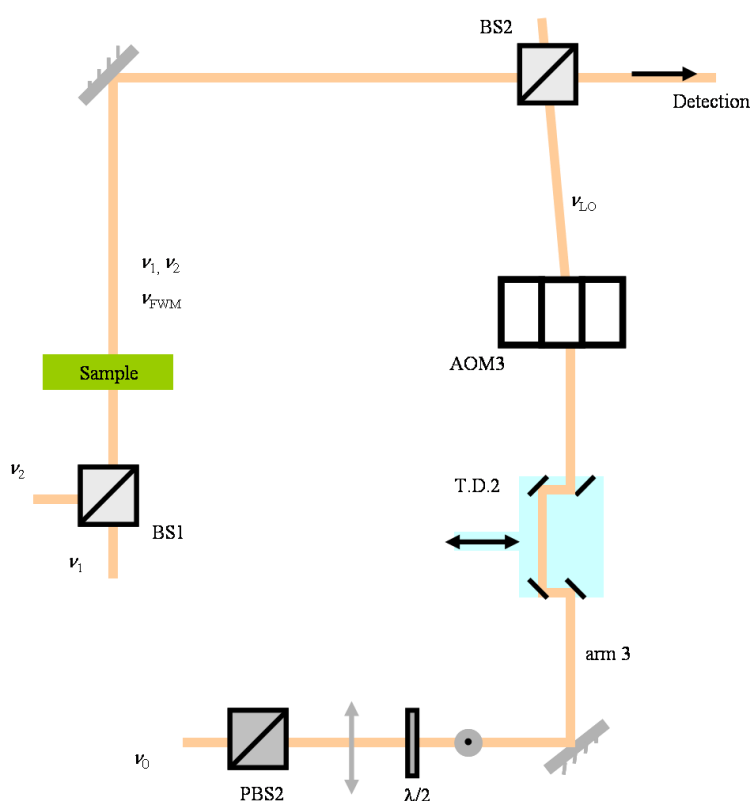


Fig. 3.6. The schematic setup for heterodyne scheme. The local oscillator is generated using the same laser source as for the excitation frequency and hence they are highly correlated. The nonlinear signal at ν_{FWM} and local oscillator at ν_{LO} are superimposed on BS2 and the beat note at $\nu_{FWM} - \nu_{LO}$ (in kHz range) is detected.

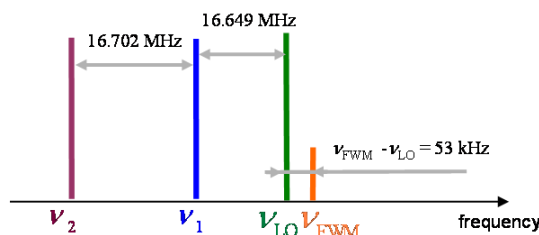


Fig. 3.7. Stick diagram including local oscillator.

The choice of the local oscillator frequency $\nu_0 + 80$ MHz is convenient, since the beat note between the local oscillator and one of the four-wave mixing frequencies $\nu_{\text{FWM}} = \nu_0 + 80.053$ MHz, is in the kHz range ($\nu_{\text{FWM}} - \nu_{\text{LO}} = 53$ kHz). The detection in kHz range is a good compromise since on the one side low-frequency noise (e.g. flicker or acoustical noise) is low and on the other side the photodiode is fast enough so that no signal roll-off occurs. The beat note is detected by means of a photodiode with low-pass filter.

Other approaches to filter the FWM product

In principle, the optical frequency components could be resolved spectrally using a bandpass filter. However, extremely narrow optical filter with parameters $\nu \approx 190$ THz and a bandpass of about 10 MHz would be necessary. Achieving these parameters using standard optical bandpass filters is a formidable task. For example, a number of optical filters (e.g. based on fiber Bragg grating) should be equal to the number of the comb lines, which is around 10^5 (spectral width of about 7 THz divided by the repetition rate of 56 MHz). Another option for spectral filtering is to use a Fabry-Perot (FP) resonator. However, for FP based filters, the dispersion over the spectral width of the laser has to be compensated.

Detection unit

The beat note amplitude can be detected using several photoreceivers⁶. The detection is carried out by InGaAs photodiode. The selected InGaAs FGA10 photodiode [Thor01] has an

⁶ The use of avalanche photodiode is advantageous, when the noise behind the photodiode, i.e. transimpedance amplifier is the dominant noise, which is not the case in this work. In the avalanche photodiode, signal amplification occurs in the photodiode itself, which ‘saves’ the use of the electronics. Using similar arguments as for the avalanche photodiode, detection of the beat note amplitude by employing a photomultiplier also does not have any advantages. Moreover, the clear disadvantage of the photomultiplier is that its quantum efficiency at 1580 nm is much lower compared to the photodiode.

active area of 1mm^2 to avoid the generation of the parasitic nonlinearities⁷ in the semiconductor material. Due to the fact that the beat note frequency ($\nu_{\text{FWM}} - \nu_{\text{LO}}$) is in the kHz range, a transimpedance amplifier with a low pass filter is used.

The beat note amplitude $E_{\text{FWM}}E_{\text{LO}}$ is detected using the InGaAs photodiode and the output voltage of the photodiode is recorded with the help of the lock-in amplifier. Two techniques for the generation of the reference input to the lock-in are discussed.

The detected photocurrent i_{pc} is related to the optical power P_{opt} that reaches the photodetector by the following expression

$$i_{\text{pc}} = \eta \cdot q \cdot \frac{P_{\text{opt}} \lambda}{hc} \quad (3.2)$$

where η is the quantum efficiency, q is the electron charge, h is the Planck constant, and c is the speed of light. The ' hc ' denominator is equal to $1.24 \text{ eV} \cdot \mu\text{m}$ and the quantum efficiency of InGaAs at $\lambda_0 = 1580 \text{ nm}$ is 90%. This yields the conversion factor between the photocurrent and the optical power in units of Ampere / Watt

$$i_{\text{pc}} [\text{A}] = 1.15 [\text{A/W}] \cdot P_{\text{opt}} [\text{W}] \quad (3.3)$$

The AC component of the photocurrent (at frequency $\nu_{\text{FWM}} - \nu_{\text{LO}}$) is proportional to the beat note amplitude $E_{\text{FWM}}E_{\text{LO}}$ as

$$i_{\text{FWM-LO}} \propto E_{\text{FWM}}E_{\text{LO}} \quad (3.4)$$

The operational amplifier, which often called op-amplifier (or op-amp), is used to amplify the beat note amplitude coming from the photodiode. The self-integrated low-pass filter with resistor R_{amp} is inserted in the feedback loop on the OP amplifier, so that the output voltage is given by

$$V_{\text{PD}} = i_{\text{FWM-LO}} R_{\text{amp}} \quad (3.5)$$

⁷ This will be discussed in section 3.4.

We see that the OP amplifier converts current to voltage, i.e. its transfer function is V_{PD} / i_{FWM-LO} . This type of amplifier is called a transimpedance amplifier. The electrical circuit of the transimpedance with a low-pass filter is schematically shown in Fig. 3.8. The transimpedance can be changed by choosing different resistors R_{amp} (the maximum V_{bias} voltage is 5 V and the voltage divider was used to match the lab voltage of 15 V).

Following Eq. (3.3)-(3.5), the value of the output voltage of photodiode V_{PD} is proportional to the AC component of the photocurrent i_{FWM-LO}

$$V_{PD} \propto i_{FWM-LO} \propto E_{FWM} E_{LO} \quad (3.6)$$

From Eq. (3.6) it is observable that the variables: output voltage of the photodiode V_{PD} and $E_{FWM} E_{LO}$ are proportional to each other.

When observing small signals, spurious mixing processes in the detection unit can hamper the measurements. Therefore, a careful choice of the electronics behind the photodiode is an important issue and is discussed below.

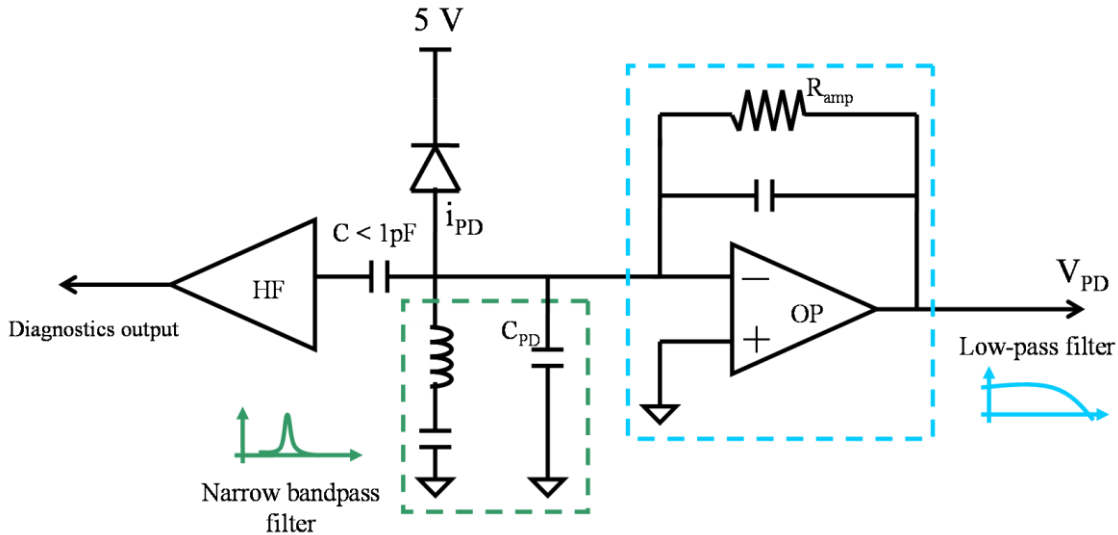


Fig. 3.8. A schematic draw of the inserted electronics behind the photodiode. OP: OP amplifier. HF: HF amplifier, C_{PD} - capacitance of the photodiode and OP amplifier. The detection of the photocurrent i_{in} is carried out by low-pass filter. The photocurrent i_{PD} is amplified by the gain V_{PD} / i_{PD} . The gain of the transimpedance amplifier can be varied by changing the value of the resistance R_{amp} . A narrow bandpass filter is included for diagnostics of the beat notes amplitudes at higher (\sim MHz) frequencies.

To measure the transfer function of the transimpedance amplifier, a laser diode is modulated with the help of RF-generator. The transfer function of the OP transimpedance amplifier is shown in Fig. 3.9. It is observable that a signal at frequencies higher than 280 kHz is sufficiently filtered.

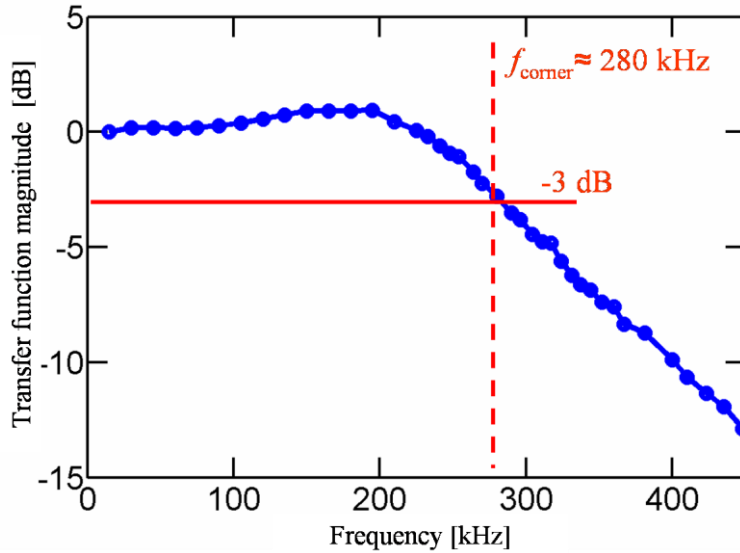


Fig. 3.9. The transfer function magnitude of the photodiode behind the transimpedance amplifier. This transimpedance amplifier with self-integrated low-pass filter ($f_{\text{corner}} = 280 \text{ kHz}$) is used for the detection of the beat note frequency $\nu_{\text{FWM}} - \nu_{\text{LO}}$.

The frequencies higher in MHz range can not be efficiently detected behind the low-pass filter. For purpose of the elimination of the parasitic signal (will be discussed in section 3.4, shown in Fig. 3.20), it is important to diagnose the beat notes between the local oscillator and the excitation fields ($\nu_{\text{LO}} - \nu_1 = 16.649 \text{ MHz}$ and $\nu_1 - \nu_2 = 16.702 \text{ MHz}$) with PD1. The detection of other higher frequencies is unwanted (it increases the noise level). Hence, to detect only frequencies $\nu_{\text{LO}} - \nu_1$ and $\nu_1 - \nu_2$, a narrow bandpass filter is desirable. To this end, the alternative diagnostic output from the photodiode in form of the narrow bandpass filter is created.

The transfer function of the diagnostic output is shown in Fig. 3.10. It has a resonance frequency of 16.67 MHz and a FWHM (Full Width at Half Maximum) of about 500 kHz. To achieve these parameters, the parameters of the inductance and capacitance are carefully chosen. The LC series circuit together with the capacity of the photodiode (and the OP amplifier) is coupled through the small capacitance ($< 1 \text{ pF}$) to the high-frequency (HF) amplifier. The small value of the capacitance is chosen in order to prevent the influence of the

HF-amplifier on the low-pass (ordinary) output. Using such narrow bandpass filter with HF-amplifier, the beat note amplitudes between the local oscillator and the excitation components at $\nu_{LO} - \nu_1 = 16.649$ MHz and $\nu_1 - \nu_2 = 16.702$ MHz, respectively, are efficiently detected and the other high frequencies are suppressed.

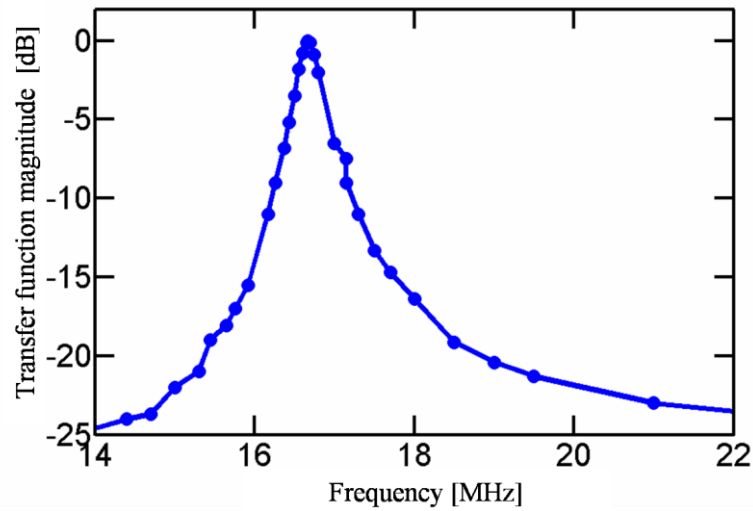


Fig. 3.10. The transfer function of the diagnostics output with maximum gain at 16.67 MHz. This output will be used to control the value of amplitude of the beat note at $\nu_1 - \nu_2$ when suppressing a parasitic signal (will be discussed in section 3.4).

Lock-in detection

The output voltage of the photodiode V_{PD} is recorded with a lock-in amplifier. The lock-in amplifier is based on phase-sensitive detection, i.e. the detection is made by synchronizing the input signal to the reference signal⁸.

The lock-in amplifier allows for frequency-selected detection of V_{PD} by narrow filtering if the frequency of the input reference f_{ref} is equal to $f_s = \nu_{FWM} - \nu_{LO}$. Two approaches are discussed for generation of the reference signal to the lock-in amplifier (SR830 - up to 100kHz frequency range).

⁸ The voltage input to the lock-in amplifier is given by $V_{PD} \cdot \sin(2\pi f_s t + \phi_s)$, where $f_s = \nu_{FWM} - \nu_{LO}$ and the reference input voltage is $V_{LI} \cdot \sin(2\pi f_{ref} t + \phi_{ref})$. By choosing the reference frequency f_{ref} to be equal to the beat note frequency f_s , internal mixing product of the lock-in is given by

$$V_{PD} \cdot \sin(2\pi f_s t + \phi_{sig}) \cdot V_{LI} \cdot \sin(2\pi f_s t + \phi_{ref})$$

Additionally, by putting a low-pass filter at the lock-in output, only the DC term from the equation above is passed through and the other terms are filtered:

$$V_{PD} \cdot V_{LI} \cdot \cos(\phi_s - \phi_{ref})$$

The lock-in, instead, allows the signal detection with an extreme narrow filtering, up to the bandwidth of the lock-in (acquisition time of the cleanup oscillator), 25 Hz for SR830. In principle, a simple amplifier instead of the lock-in can be used to detect the voltage level V_{PD} . Let us assume that the voltage level V_{PD} (at $\nu_{FWM} - \nu_{LO}$) is 10^{-8} V. A good amplifier has the noise of about 10^{-8} V/ $\sqrt{\text{Hz}}$. For example, by taking a bandwidth of 100 kHz and a gain of 1000, the signal (V_{PD}) will be amplified to 10^{-5} V and an effective noise value $3 \cdot 10^{-3}$ V is much larger than the signal. Additionally, the phase-sensitive detection is not possible with the simple amplifier.

‘Purely electrically’ produced reference input

The reference input voltage to the lock-in amplifier is generated by directly mixing the electrical signals coming from three RF-generators, as shown in Fig. 3.11. Three RF generators are served as AOM drivers and the frequency difference between their RF-signals is the same as between the excitation and local oscillator frequencies (46.649 MHz, 63.351 MHz, and 80 MHz). The RF-signal at frequency 63.351 MHz is sent through the saturated RF-amplifier, which results in the electrical nonlinear signal at doubled frequency (126.72 MHz = 2 x 63.351 MHz). The RF-signals at frequencies 126.72 MHz and 46.649 MHz are mixed to produce the RF-signal at 80.053 MHz. This is mixed with the RF-signal at frequency 80 MHz to generate the reference signal at 53 kHz, which is used as the reference input voltage.

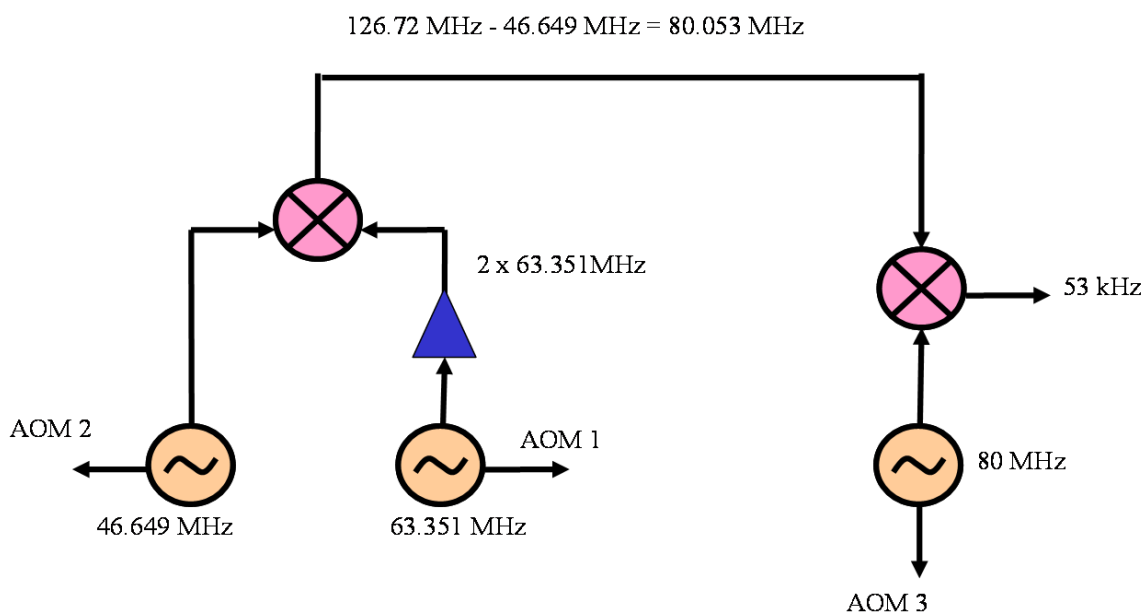


Fig. 3.11. A Scheme for the generation of the reference input voltage to the lock-in amplifier.

A scheme for generation of the reference input directly by the AOM drivers can be used if drift e.g. due to interferometric path length variations or fluctuations of the acoustic wave delay inside the AOMs are low.

‘All optically’ produced reference input

The beat note amplitude $E_{\text{FWM}}E_{\text{LO}}$ (and hence V_{PD}) has phase perturbations that are gained as a result of its travelling through the setup due to interferometer noise, AOM driving signals, and time-varying AOM phase shifts. Therefore, it is desirable to have the reference input voltage, which contains the noise from ‘the same nature’ and hence can be common-mode rejected. The reference input voltage is generated ‘all-optically’ by an additional reference-photodiode PD2, as shown in Fig. 3.12. The reference-photodiode detects the light from the unused output of the beam splitter BS2. The photodiode includes a transimpedance amplifier with the cut-off frequency at 70 MHz. This fast amplifier allows to monitor the difference frequency between both excitation fields at 16.702 MHz and between the local oscillator and one of the excitation fields at 16.649 MHz. These beat notes are filtered with the help of narrow bandpass filters and are sent into the RF-mixer. It mixes both beat notes and outputs the signal at the difference frequency of 53 kHz (16.702 MHz – 16.649 MHz), which is equal to the frequency of the beat note amplitude (see Fig. 3.12). In principle, the diagnostics output instead of PD2 for the generation of the reference signal at 53 kHz can be used. However, the reference signal that is generated using the diagnostics output might act as a spurious signal if it is reflected from the electronics back into the PD1 and reaches the ordinary output. To avoid this scenario, the reference signal is generated by the additional photodiode PD2.

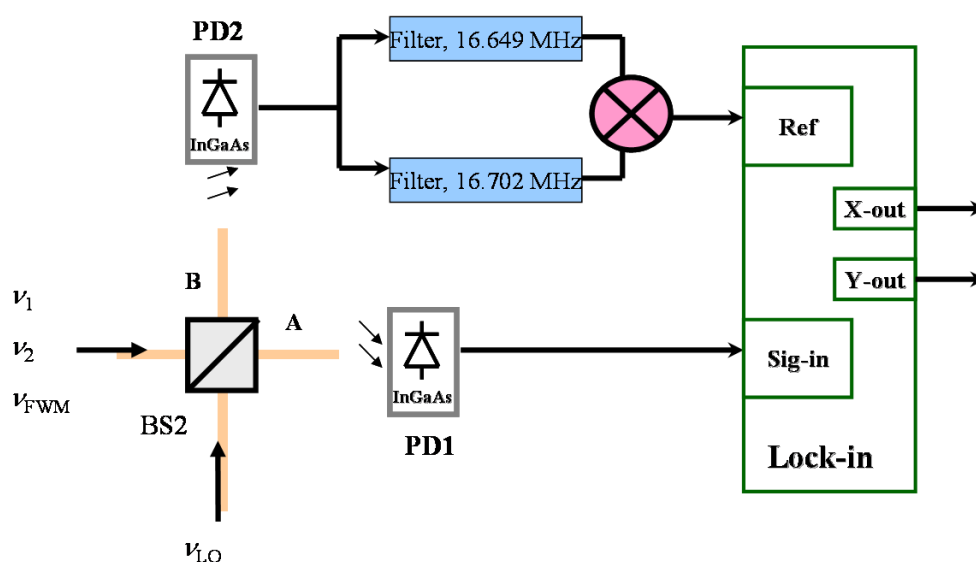


Fig. 3.12. A scheme for generation of the reference input voltage to the lock-in amplifier ‘all-optically’. Interferometric fluctuations are common-mode rejected.

By the ‘all-optically’ lock-in reference input, remaining phase-modulation noise of the AOM drivers and interferometric fluctuations are common-mode-rejected.

Fig. 3.13 shows the variation of V_{PD} (detected by PD1) as a function of time. V_{PD} is detected by the lock-in by directly mixing the electrical signals from the AOM drivers (green) and ‘all-optically’ (blue). It is clearly seen that when the reference input voltage to the lock-in is generated ‘all-optically’, the signal V_{PD} is more stable and different drifts, i.e. due to interferometric noise, are suppressed.

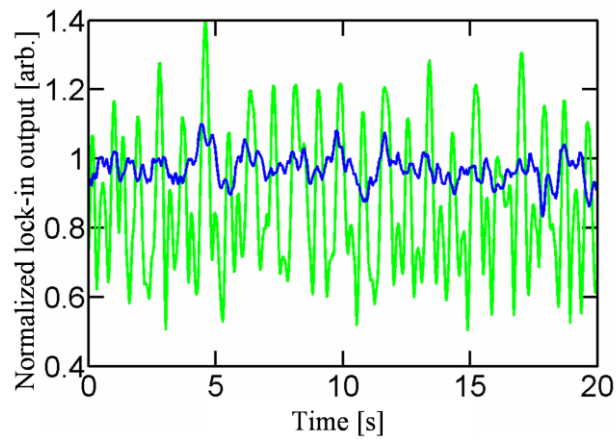


Fig. 3.13. Time variation of the photodiode output V_{PD} as detected ‘all optically’ (blue) and ‘purely electrically’ (green). It is clearly seen that ‘all-optically’ detected signal is more stable.

3.3 Measurement of waveguide's nonlinearity using heterodyning

To demonstrate the sensitivity of the heterodyne detection, a short piece (13.5 mm) of a standard optical fiber SMF-28 as a waveguide is tested. The verification of the FWM generation is done by reducing the optical power behind the EDFA and in front of the photodiode PD1, respectively, as shown schematically in Fig. 3.14.

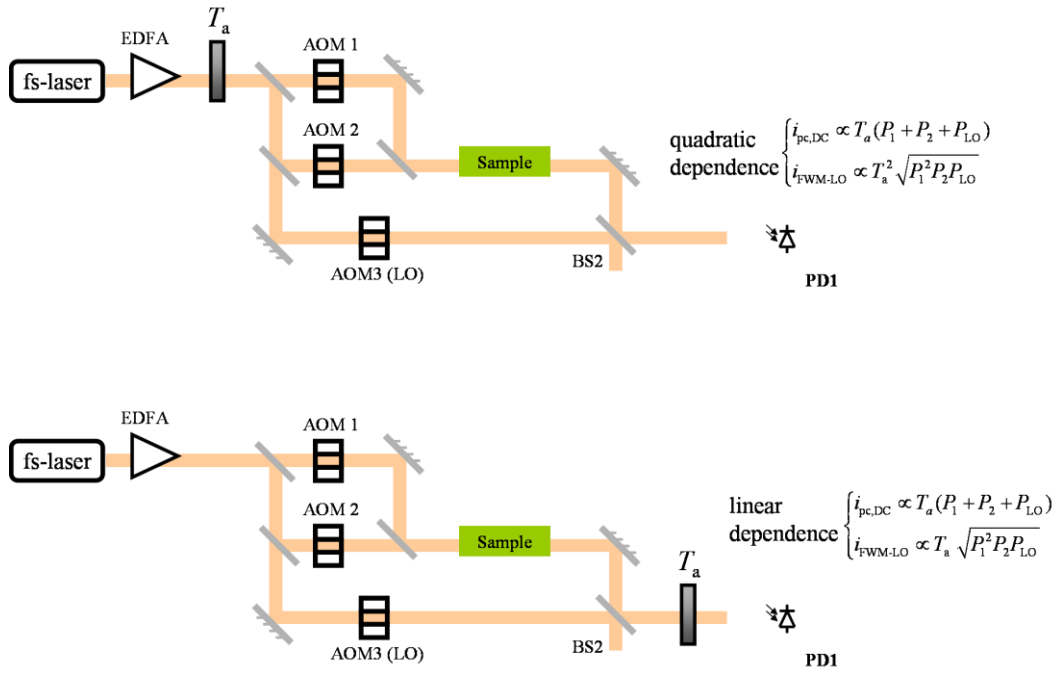


Fig. 3.14. The optical power is reduced by placing the attenuator (T_a) behind the EDFA (top) or in front of the photodiode (bottom).

By attenuating the optical power in different positions within the setup, different potential dependence of the AC photocurrent between the local oscillator and the FWM (i_{FWM-LO}) on the average photocurrent is observed due to the fact that $P_{FWM} \propto P_1^2 P_2 (\sqrt{P} = E)$. The average (DC) photocurrent i_{DC} is given by

$$i_{pc,DC} \propto T_a (P_1 + P_2 + P_{LO}) \quad (3.7)$$

where P_1, P_2, P_{LO} are the measured optical powers from local oscillator and excitation fields that fall on the photodiode PD1, and T_a the attenuation factor (also shown in Fig. 3.14). Note that the contribution to the average photocurrent of the FWM signal is neglected, since its

magnitude is much smaller than from the optical powers from the local oscillator and excitation fields (due to the short fiber, the gained FWM is small).

When the attenuation is performed before the nonlinear interaction occurs (behind the EDFA), the AC photocurrent $i_{\text{FWM-LO}}$ is reduced by each of the excitation and local oscillator optical powers as

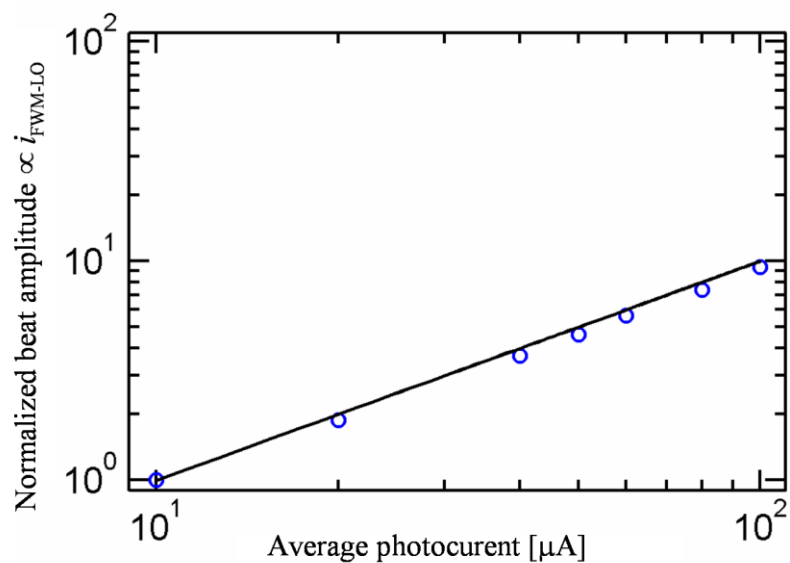
$$i_{\text{FWM-LO}} \propto \sqrt{(T_a P_1)^2 T_a P_2 T_a P_{\text{LO}}} = T_a^2 \sqrt{P_1^2 P_2 P_{\text{LO}}} \quad (3.8)$$

This leads to the quadratic dependence of the beat note photocurrent $i_{\text{FWM-LO}}$ on the transmittance (quadratic power law). When the attenuation takes place after the nonlinear interaction (in front of the photodiode, behind BS2), the FWM optical power and the local oscillator optical powers are attenuated, i.e. the beat note photocurrent $i_{\text{FWM-LO}}$ is attenuated linearly with the transmittance, resulting in a linear power law, since

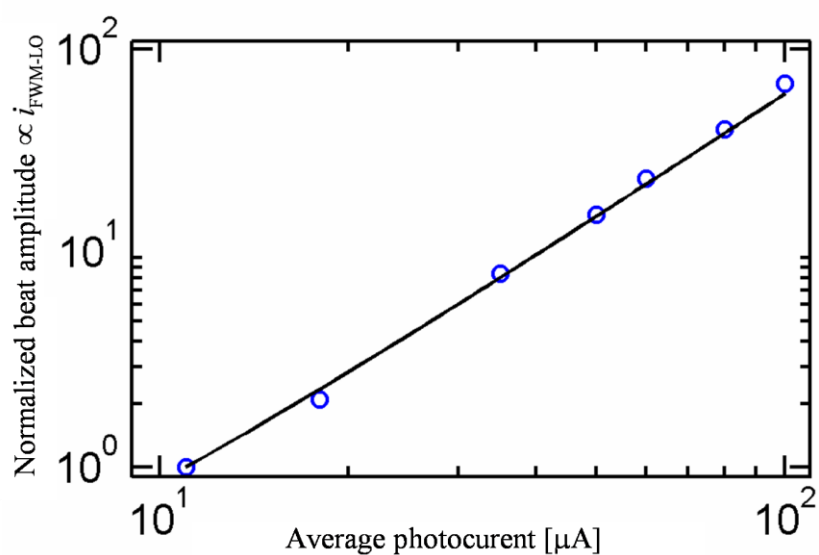
$$i_{\text{FWM-LO}} \propto \sqrt{T_a (P_1^2 P_2) T_a P_{\text{LO}}} = T_a \sqrt{P_1^2 P_2 P_{\text{LO}}} \quad (3.9)$$

Fig. 3.15 shows the beat note amplitude ($\propto i_{\text{FWM-LO}}$) dependence on the average photocurrent i_{DC} for the attenuation in front of the photodiode and behind the EDFA. The linear and quadratic dependences of the beat note amplitude on the average optical power behind the EDFA and in front of the photodiode, respectively, are observed. This provides the experimental evidence that the nonlinearity in fact arises from the SMF-28 fiber.

It is worth to note, that by putting the attenuator in other place within the setup, e.g. behind the waveguide and in front of the BS2, yields the square-rooted dependence, since the optical power of the local oscillator is not attenuated (this case is not shown in Fig. 3.14).



(a)



(b)

Fig. 3.15. Experimental evidence of the nonlinear signal from short piece of fiber (SMF-28). The normalized beat note amplitude ($\propto i_{\text{FWM-LO}}$) is plotted as a function of the average photocurrent i_{DC} . Experimental results are depicted as circles. (a) Attenuation is done after the nonlinear interaction (in front of the photodiode behind BS2). A continuous line reveals a linear power law. (b) Attenuation is done before the nonlinear interaction (directly behind the EDFA). A continuous line reveals a quadratic power law.

The effective nonlinearity of 13.5 mm short SMF-28 is $\gamma_{\text{SMF-28}} = 1.94 \text{ W}^{-1}\text{km}^{-1}$, which is in agreement with the value reported in [Agra89]. The value is obtained by comparing the beat notes, as explained below.

The beat note amplitude between the FWM product and the local oscillator ($E_{\text{FWM}}E_{\text{LO}}$) is 10^{-2} times that of the beat note amplitude between the excitation field at ν_1 and the local oscillator (E_1E_{LO}). This means that the level of the optical power P_1 is 40 dB larger than the level of the optical power from the mixing product. The average optical powers (P_{av}) behind the waveguide are $P_1 = 3 \text{ mW}$ and $P_2 = 1.5 \text{ mW}$, for the excitation fields at ν_1 and ν_2 , respectively. As a consequence, the average optical power of the mixing product behind the waveguide is $P_{\text{FWM}} = 3 \text{ mW} / 10^4 = 3 \cdot 10^{-7} \text{ W}$. As it was shown in chapter 2, for the quantitative determination of effective nonlinearity γ it is necessary to measure the peak optical powers $P_{1,\text{peak}}$, $P_{2,\text{peak}}$ and $P_{\text{FWM,peak}}$. Using $\gamma = \sqrt{P_{\text{FWM,peak}}} / \sqrt{P_{1,\text{peak}}^2 P_{2,\text{peak}}} / L$, the effective nonlinearity is $\gamma_{\text{SMF-28}} = 1.94 \text{ W}^{-1}\text{km}^{-1}$. The conversion between the peak and the average powers for the determination of the effective nonlinearity is done by using the following formula

$$P_{\text{peak}} = \frac{P_{\text{av}}}{f_r} \cdot \frac{1}{\tau_p} \quad (3.10)$$

which ignores the parameters due to the pulse characteristics. For example, for Gaussian-shaped pulses the relation between peak and average power is $P_{\text{peak}} \approx 0.94 \frac{P_{\text{av}}}{f_r} \cdot \frac{1}{\tau_p}$ and for

sech² shape pulses this relation is $P_{\text{peak}} \approx 0.88 \frac{P_{\text{av}}}{f_r} \cdot \frac{1}{\tau_p}$. Eq. (3.10) is a good approximation if

the temporal shape of the pulse does not contain wings.

3.4 Technique for elimination of the parasitic signal when investigating weak optical nonlinearities

By investigating waveguiding samples with weaker optical nonlinearities than of SMF-28 (i.e. HC-PCF), different types of concurrent signals due to the photodiode can hamper the detection. A parasitic concurrent signal is an unwanted background signal, whose frequency is equal to the frequency of the beat note amplitude at $\nu_{\text{FWM}} - \nu_{\text{LO}}$. A technique that eliminates the parasitic signal has been developed in the scope of this thesis.

A basic test to verify that a signal comes from the waveguide can be performed by observing a zero signal at $\nu_{\text{FWM}} - \nu_{\text{LO}}$ when blocking any of the three arms (both arms of the excitation and local oscillator signals), respectively. An additional verification is the linear dependence of the beat note photocurrent on the DC photocurrent in front of the photodiode, as discussed previously in section 3.3. Fig. 3.16 shows the photocurrent due to the concurrent parasitic signal at frequency $\nu_{\text{FWM}} - \nu_{\text{LO}}$ as a function of the average photocurrent, which was varied by attenuating the optical power in front of the photodiode (behind BS2). From the figure is observable that the photocurrent shows a quadratic (and not linear, as in Fig. 3.15a) power law. This means that the parasitic signal is dependent on the optical power and is generated behind the attenuator, i.e. in the detection unit.

The parasitic signal due to the detection unit can be generated either before the conversion the light into the photocurrent (during the photo-detection process) or after it.

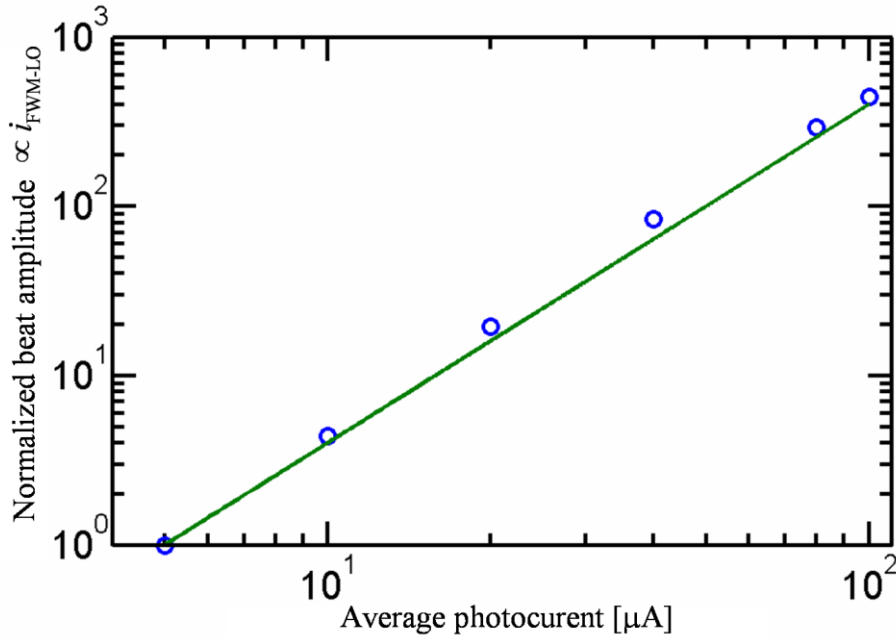


Fig. 3.16. Observation of the parasitic signal that is generated in the detection unit. The normalized beat note amplitude ($\propto i_{\text{FWM-LO}}$) is plotted as a function of the average photocurrent $i_{\text{pc,DC}}$. Experimental results are depicted as circles. The continuous line reveals a quadratic power law, when attenuating the optical power in front of the photodiode. The photocurrent $i_{\text{FWM-LO}}$ is due to the parasitic signal at frequency $\nu_{\text{FWM}} - \nu_{\text{LO}}$. The parasitic signal in the detection unit (photodiode and/or transimpedance amplifier) can hamper the detection.

The first step to eliminate the parasitic signal generated in the photodiode is to use the photodiode, where this effect is the smallest. This happens for photodiodes with large active area, since the detected intensity is small and for this reason the generated parasitic signal due to the nonlinearity in the photodiode is small (Nonlinearity \propto Power/Area). Several photodiodes that are fast enough to detect the beat note with areas of order of mm^2 are selected in order to observe in which photodiode the generated parasitic signal is the smallest. It turned out that a 1mm^2 photodiode of type FGA10 from Thorlabs generates significantly smaller parasitic signal than other tested photodiodes.

The level of the observed parasitic signal from FGA10 photodiode is 45 dB smaller than the mixing product from the SMF-28, but still greater than the expected mixing product from HC-PCF. The mixing product from HC-PCF is expected to be 60 dB (10^3 times in amplitude) smaller than from SMF-28 (HC-PCF has a nonlinearity that is about 10^3 times smaller than SMF-28, since HC-PCF guides most of the light through its hollow core).

To identify the source of the parasitic signal in the photodiode and to see if the parasitic signal is generated before the conversion of the light into the photocurrent, the intensity is changed while keeping the averaged photocurrent constant. The results of this experiment are shown in Tab. 3.1. From the table is observable that the level of the photocurrent at frequency $\nu_{\text{FWM}} - \nu_{\text{LO}}$ is changed only in 10%. Hence, the dominant parasitic signal is generated after the light conversion, i.e. due to the photocurrents, which are independent on the illuminated area on the photodiode.

Active area covered by light [%]	100%	50%	25%
Level of the parasitic signal (normalized).	1	1.1	1.1

Tab. 3.1. The intensity (illuminated active area) is changed by keeping the averaged photocurrent to be constant. No significant change in level of the parasitic signal at frequency $\nu_{\text{FWM}} - \nu_{\text{LO}}$ is observed. Therefore, the photo-detection process does not dominate the generation of the parasitic signal.

The parasitic signal after the light conversion is generated as a result of the interaction of the photocurrents and the illustration of this process is shown in Fig. 3.17. The parasitic signal due to the photocurrents is generated when the photocurrent beat signal at $\nu_1 - \nu_2$ ('a' in Fig. 3.17) and the photocurrent beat signal at $\nu_{\text{LO}} - \nu_1$ ('b') interact and produce a signal ('c') at $(\nu_1 - \nu_2) - (\nu_{\text{LO}} - \nu_1) = (2\nu_1 - \nu_2) - \nu_{\text{LO}}$, i.e. with the same frequency as the desired heterodyne beat signal ('d'). The interaction of the photocurrents can occur either in the photodiode or in the OP transimpedance amplifier.

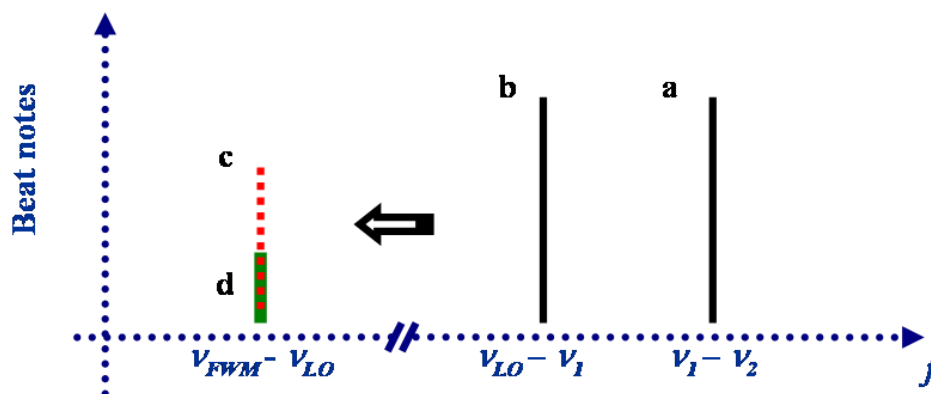


Fig. 3.17. Scheme for visualisation of parasitic signal generation. The photocurrent beat signals between the excitation and the local oscillator fields ‘a’ and ‘b’ generate the concurrent parasitic signal ‘c’ at the same frequency as the desired beat signal ‘d’. The desired signal might be smaller than the concurrent signal. This hampers the detection of the FWM from the sample of interest.

The dominance of the parasitic signal due to the interaction of the photocurrents in the transimpedance amplifier is excluded by performing the experiment, which is schematically shown in Fig. 3.18. The photocurrents at $\nu_{LO} - \nu_1$ and $\nu_1 - \nu_2$ are simulated by producing the currents electrically. Instead of the photodiode, two RF generators are inserted behind the photodiode and in front of the amplifier. The RF generators produce signals at frequencies, which are equal to the frequencies $\nu_{LO} - \nu_1$ and $\nu_1 - \nu_2$. The amplitudes of the currents at the output of the amplifier are adjusted to be the same as the amplitudes of the photocurrents. The measured parasitic signal amplitude at frequency $\nu_{FWM} - \nu_{LO}$ at the output of the amplifier due to the currents is about 50 times smaller than the observed parasitic signal that is produced by the photocurrents (with the photodiode in front of the amplifier). Therefore, the dominant parasitic signal is due to the photocurrents interaction in the photodiode.

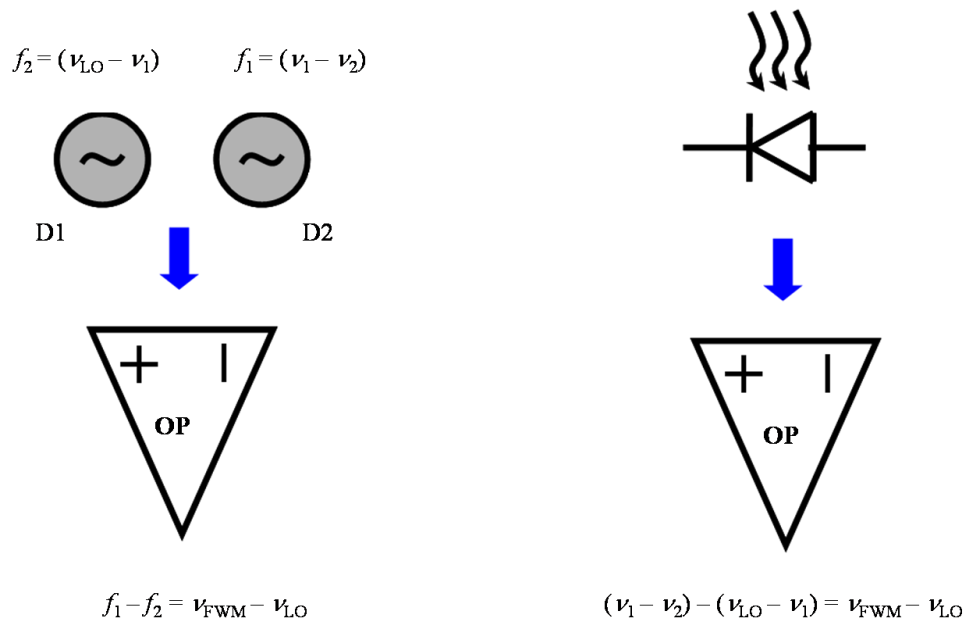


Fig. 3.18. The beat notes between the excitation fields at $\nu_1 - \nu_2$ and between the local oscillator and the excitation field at $\nu_{LO} - \nu_1$ generate the parasitic signal at $\nu_{FWM} - \nu_{LO}$ either in the photodiode (right) or in the transimpedance amplifier behind the photodiode (left). To reveal the dominant process (photocurrents interaction in the amplifier or in the photodiode), the frequencies f_1 and f_2 have been generated electrically behind the photodiode and in front of the amplifier. RF generators are denoted by D1 and D2. The parasitic signal due to currents interaction in the transimpedance amplifier is much smaller than the parasitic signal due to the photocurrents interaction in the photodiode.

The parasitic signal due to the interaction of the beat note photocurrents in the photodiode can be reduced by developing a compensation technique, which details are explained further.

Elimination of the parasitic signal

The technique is based on the elimination of one of the beat photocurrents ('a' or 'b') that is responsible for the parasitic signal generation. The principle of the compensation technique is schematically depicted in Fig. 3.19. As a result of the reduction of one of the beat photocurrents (i.e. $i_a \cdot \cos(2\pi(\nu_1 - \nu_2)t)$, 'a') that is involved in generating the parasitic signal, the concurrent parasitic signal $i_c \cdot \cos(2\pi(\nu_{\text{FWM}} - \nu_{\text{LO}})t)$ is reduced as well.

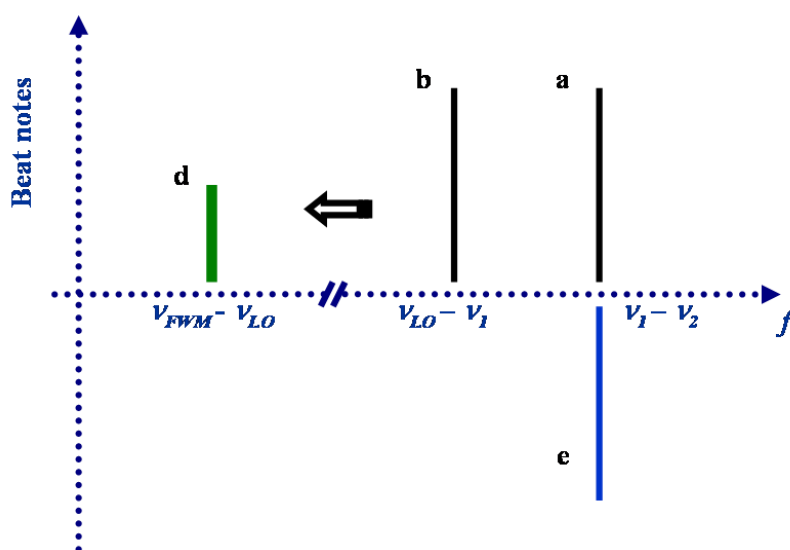


Fig. 3.19. Visualisation scheme for elimination of the concurrent signal. An additional signal 'e' at frequency $\nu_1 - \nu_2$ is sent with the *opposite phase* to the signal 'a' onto the photodiode. By this procedure, the parasitic signal 'c' is eliminated, which allows the detection of the desired signal 'd'.

In order to reduce the beat photocurrent $i_a \cdot \cos(2\pi(\nu_1 - \nu_2)t)$, an additional auxiliary photocurrent $i_e \cdot \cos(2\pi f_e t)$ is generated ('e' in Fig. 3.19). The frequency of the compensation photocurrent 'e' is identical to the frequency of the photocurrent 'a', i.e. $f_e = \nu_1 - \nu_2$ and the amplitudes of both photocurrents have the same strength. The signal 'e' is sent with the opposite phase to the signal 'a' onto the photodiode. By this procedure the photocurrent 'a' and hence the parasitic signal 'c' can be efficiently suppressed.

The required counterphase relation between both photocurrents can be reliably achieved using compensation pulses from the second (unused) output of the beam splitter BS1, which combines the pulses at ν_1 and ν_2 in front of the samples. This is shown in Fig. 3.20. To

achieve the efficient compensation of the photocurrent at $\nu_1 - \nu_2$, two conditions have to be satisfied: the phase difference of 180 degrees and the same amplitude of the photocurrents 'a' and 'e'.

The compensation photocurrent 'e' is generated by sending two additional pulses at frequency ν_1 and ν_2 onto the same position of the photodiode where the other signals are detected. Owing to the long time delay (about 20 ps) with respect to the pulses coming from the arm where the sample is located, these fields do not interfere with the excitation fields but generate an AC photocurrent component at $\nu_1 - \nu_2$. The frequency of this compensation photocurrent is different from the desired signal at $\nu_{\text{FWM}} - \nu_{\text{LO}}$, hence, the value of the latter is not affected by this procedure. If the phase of the current 'e' is chosen to be in counter-phase to 'a', both current components cancel each other for suitably chosen amplitudes. The 180 degrees phase difference is automatically accomplished using the fact that both photocurrents are generated from the fields that split on BS1 and meet again on BS2, i.e. due to the energy conservation law ('compensation arm' and 'sample arm', Fig. 3.20). Therefore, the overall photocurrent on the photodiode PD1 at frequency $\nu_1 - \nu_2$ can be summed up to DC.

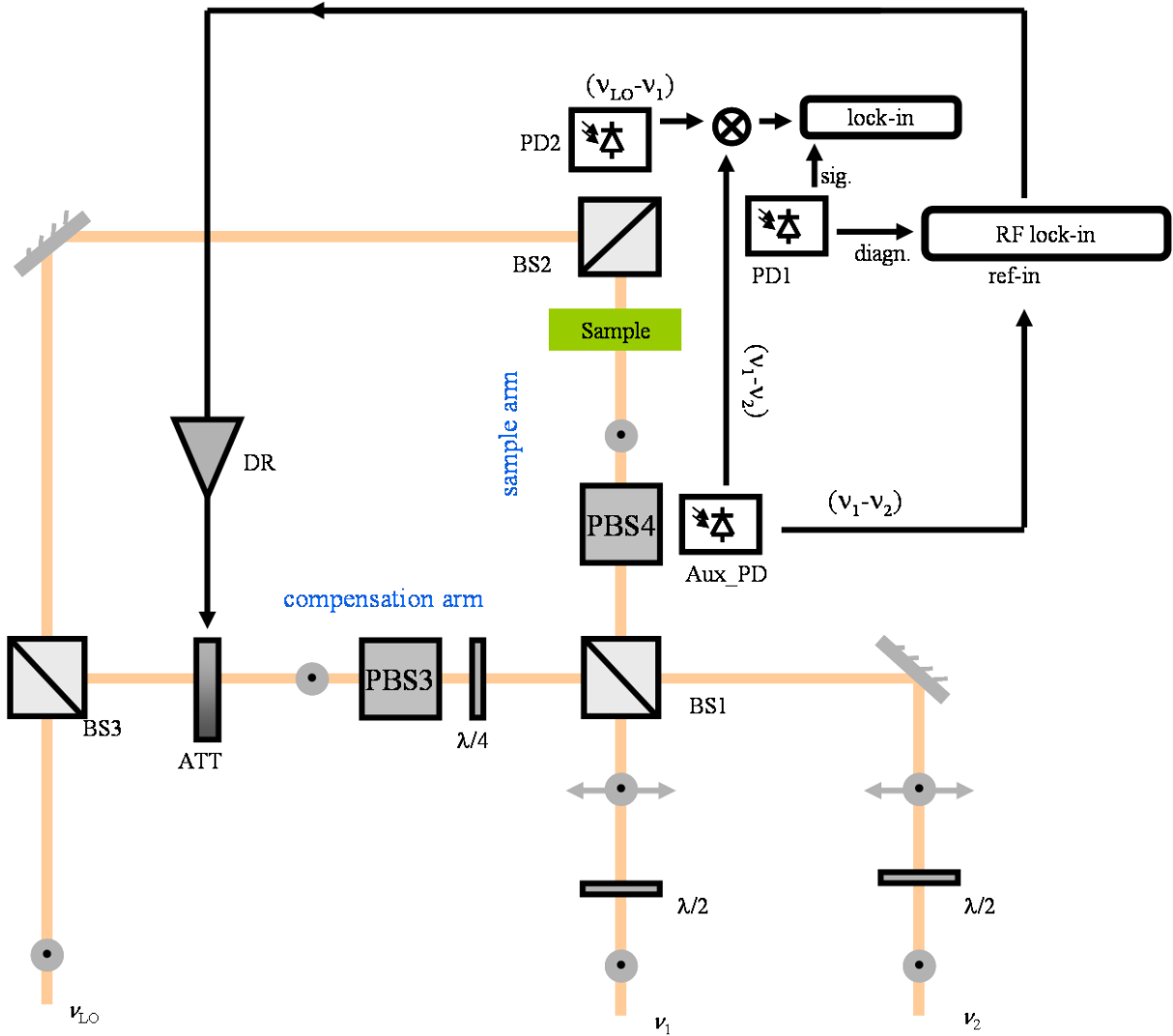


Fig. 3.20. Experimental setup for elimination of the concurrent parasitic signal. The overall photocurrent at $\nu_1 - \nu_2$ is generated from the same fields that split on BS1 and meet on BS2. ATT - Attenuator on motorized stage, DR-Driver to the motorized stage, Aux_PD - InGaAs photodiode for generating the reference signal to the RF lock-in amplifier. The compensation arm is used for the elimination. To fine adjustment of the phase between the photocurrents (' a ' and ' e '), the polarization of the excitation fields at ν_1 and ν_2 is slightly changed using $\lambda/2$ wave plates. In the compensation arm the combination of $\lambda/4$ wave plate with PBS3 changes the phases of the fields at ν_1 and ν_2 , and hence of the compensation signal. The amplitude of the signal is automatically adjusted using a feedback loop. The reference input at $\nu_{FWM} - \nu_{LO}$ to the lock-in is generated by mixing the photocurrents at $\nu_1 - \nu_2$ from Aux_PD and $\nu_{LO} - \nu_1$ from PD2.

A feedback loop is inserted to control the overall amplitude of the photocurrent at $\nu_1 - \nu_2$ and to minimize its value. The amplitude and the phase of the overall photocurrent (at $\nu_1 - \nu_2$) are recorded with the help of the additional RF lock-in amplifier (SR844). The reference input to RF lock-in is provided by using an auxiliary InGaAs photodiode (Aux_PD). This photodiode

is inserted behind the beam splitter that overlaps the excitation fields (BS1). The feedback includes a linear attenuator, which is mounted on the motorized stage. This obtains the error signal (the remaining overall signal at $\nu_1 - \nu_2$) from the RF lock-in output. For the fine tuning of the phase of the overall photocurrent, as a first step, two half-wave plates are inserted in each arm of the excitation fields. They rotate the linear polarized light by a small angle to have the light in both x and y axes, since for the relative phase shifting both components are required. Next, a quarter-wave plate and a polarizing beam splitter are inserted into the compensating arm. This is done in order to change the phase between the x and y components and so to tune the phase difference between the signals coming from both arms to be exactly 180° . Please note that the reference input to the RF lock-in is not generated employing the same photodiode as for generating the reference input for the detection of the beat note at $\nu_{\text{FWM}} - \nu_{\text{LO}}$ (PD2). This is due to the fact that also PD2 photodiode detects the overall photocurrent at frequency $\nu_1 - \nu_2$, which amplitude is zero.

The reduction of the parasitic signal is verified experimentally and the results are shown in Fig. 3.21. The phase of the compensation signal 'e' is 180 degrees to the phase of the signal 'a' and the power of the compensation signal was changed by the attenuator. It can be observed that for the same amplitude of signals 'a' and 'e', both the total signal at frequency $\nu_1 - \nu_2$ and the parasitic signal at frequency $\nu_{\text{FWM}} - \nu_{\text{LO}}$ are eliminated simultaneously.

Using the technique, a suppression of 35 dB of the parasitic signal is achieved. Further suppression can be achieved by employing a faster feedback system (faster response time of the motorized stage). Another option is to compensate the photocurrent at frequency $\nu_{\text{LO}} - \nu_1$. The suppression of 35 dB allows for investigation of samples with mixing products that have 120 dB (40 dB + 45 dB + 35 dB) smaller power than the excitation signals.

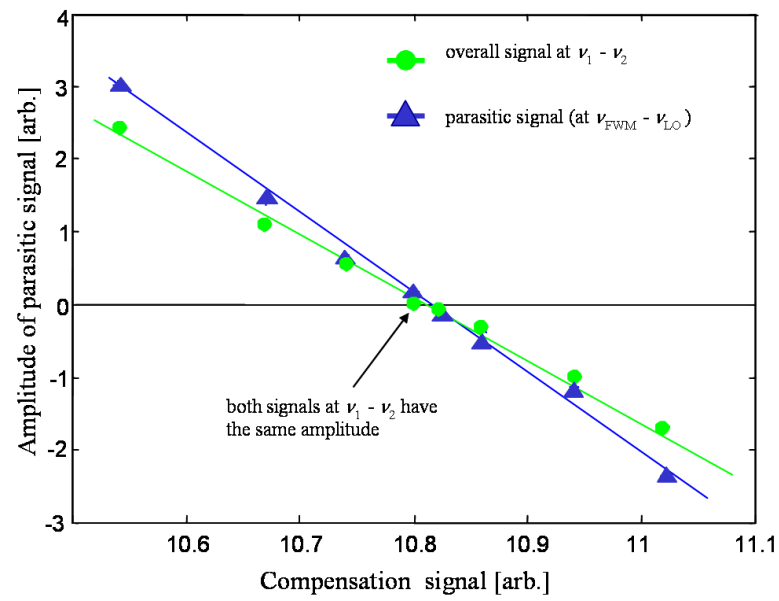


Fig. 3.21. Elimination of the concurrent parasitic signal. By employing the technique explained in text and schematically shown in Fig. 3.20, the overall signal at frequency $\nu_1 - \nu_2$ (green circles) and hence the concurrent parasitic signal (blue triangles) are eliminated.

3.5 Summary & Conclusion

The proposed setup allows to measure optical nonlinearities of the short waveguides by using moderate optical power. Heterodyning allows to detect mixing products that are many orders of magnitude weaker than its excitation fields. The elimination of the concurrent signal allows to detect weak nonlinearities. The measurements of the nonlinearities are done by taking peak amplitudes into account. Exact measurements of these quantities are difficult. Thus methods are desired that do not require characteristics of these laser parameters.

An experimental setup for the measurement of the fast optical nonresonant nonlinearities in waveguides is designed, implemented and tested. The setup configuration is based on the nearly-degenerate FWM scheme in collinear geometry combined with heterodyning. Heterodyne technique assisted to separate the FWM product from the excitation fields, which cancels phase fluctuations of the laser optical carrier frequency. The FWM beat note amplitude is detected by the photodiode with the low-frequency and recorded by the lock-in amplifier. The reference input to the lock-in is generated ‘all-optically’ and hence interferometric fluctuations are common-mode-rejected. The proposed setup is verified by employing a short piece of optical fiber. The technique for elimination of the concurrent parasitic signal arising from the photodiode is developed and implemented. Using the technique, the parasitic signal is suppressed by 35 dB, which opens up a gate for investigation of the samples with mixing products that have 120 dB smaller power than the excitation signals.

Chapter 4

Referencing to a Bulk Sample: Investigation of third-order nonlinearities in waveguides, independent of laser parameters

In this chapter a principle of operation of the method that allows to measure optical nonlinearities without need to measure peak amplitudes of the excitation fields is proposed.

The idea is to compare directly the optical nonlinearity of the waveguide of interest with that of an additional calibrated sample under identical experimental circumstances.

The nonlinearity of the waveguide is measured by referencing its value to the value of the nonlinearity of the bulk sample with well-known optical properties.

To make a comparison of the nonlinearities, the bulk sample is placed behind the waveguide. The contribution of the nonlinearity of the bulk sample to the overall nonlinear signal is switched on and off by shifting it either closer or further away from the waveguide's output. Placing the bulk behind (and not in front of) the waveguide ensures the same spatial beam profile for both samples when the bulk is located (directly) at the waveguide's output. The procedure is depicted in Fig. 4.1.

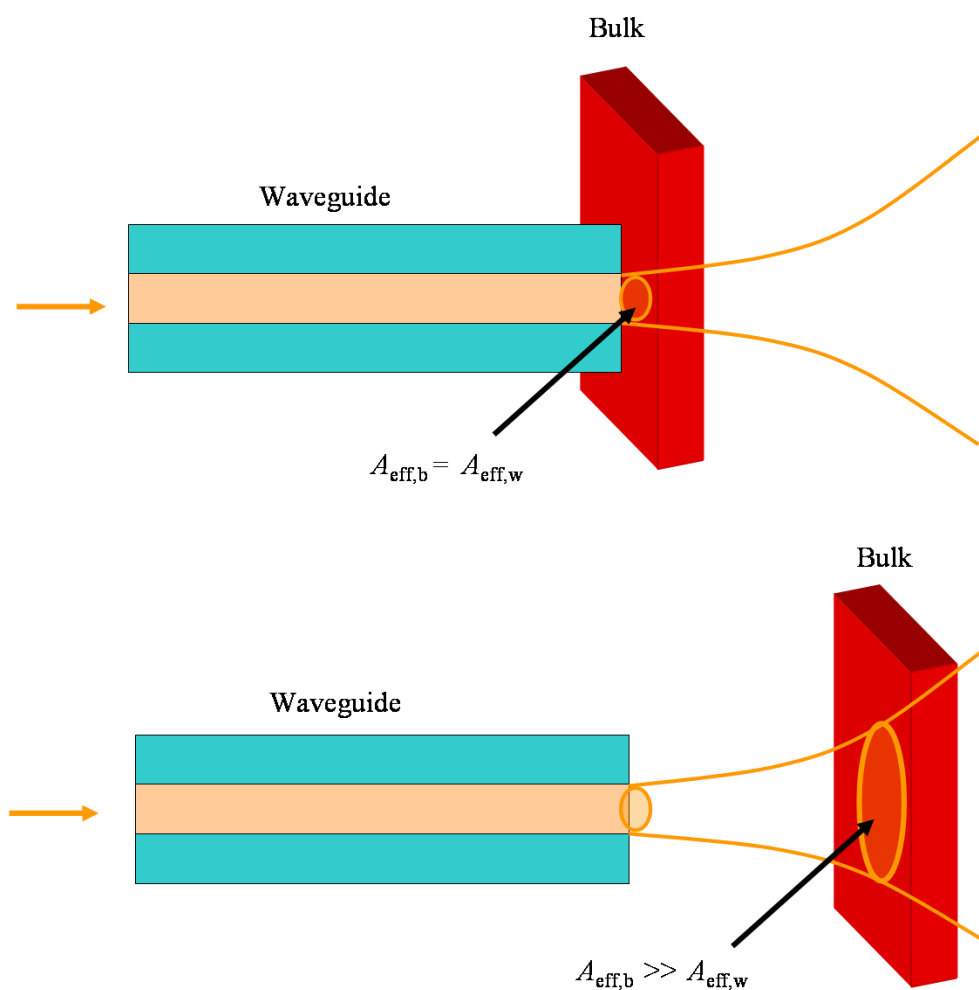


Fig. 4.1. Principle of the Referencing-to-Bulk Sample (ReBuS) method. The overall FWM signal is given by two contributions: one from the waveguide and the other from the bulk sample. The bulk sample is shifted behind the waveguide and as a result, the nonlinear contribution from the bulk sample to the overall nonlinear signal changes. When the bulk sample is located far from the waveguide ($A_{\text{eff,b}} \gg A_{\text{eff,w}}$), its contribution is neglected ($E_{\text{FWM}} \propto 1/A_{\text{eff}}$). When the bulk is located directly behind the waveguide ($A_{\text{eff,b}} = A_{\text{eff,w}}$), it contributes noticeably to the overall signal. Mode field area of the waveguide is denoted by $A_{\text{eff,w}}$. Spatial profile of the beam coming out of the waveguide and entering the bulk sample is denoted by $A_{\text{eff,b}}$. The optical properties of the bulk sample are well-known.

In the following the procedure is described mathematically. For the sake of simplicity it is assumed that both samples (waveguide and bulk) do not have nonlinear absorption, i.e. their nonlinear fields are in phase. Using Eq. (2.5), the FWM field E_{FWM} from the waveguide 'w' is expressed by

$$E_{\text{FWM}} = \left(\frac{n_{2,w} k_0}{A_{\text{eff},w}} \right) E_{1,\text{peak}}^2 E_{2,\text{peak}} L_w$$

where $n_{2,w}$ is a value of interest and describes the nonlinearity of the waveguide. The overall FWM field E_{FWM} from both samples is given by

$$E_{\text{FWM}} = \left(\frac{n_{2,w} k_0}{A_{\text{eff},w}} \right) E_{1,\text{peak}}^2 E_{2,\text{peak}} L_w + \left(\frac{n_{2,b} k_0}{A_{\text{eff},b}} \right) E_{1,\text{peak}}^2 E_{2,\text{peak}} L_b \quad (4.1)$$

where 'w' and 'b' indicate the waveguide and bulk samples.

Eq. (4.1) shows that the FWM signal includes two terms. The first term is proportional to the nonlinear refractive index of the bulk sample $n_{2,b}$ and it is 'well known' value. The second term is proportional to the unknown nonlinear refractive index of the waveguide $n_{2,w}$. When the bulk sample is placed far from the waveguide's output (bottom of Fig. 4.1), its contribution to the overall nonlinear signal is negligible, since the spatial profile of the bulk sample $A_{\text{eff},b}$ is much larger than that of the waveguide $A_{\text{eff},b} \gg A_{\text{eff},w}$. In such case, the overall FWM field is given by

$$E_{\text{FWM, far}} = \frac{n_{2,w} k_0}{A_{\text{eff},w}} E_{1,\text{peak}}^2 E_{2,\text{peak}} L_w \quad (4.2)$$

where $E_{\text{FWM, far}}$ corresponds to the value of the FWM when the bulk sample is far from the waveguide's output.

When the bulk sample is placed directly behind the waveguide's output, so that $A_{\text{eff},w} = A_{\text{eff},b}$, the overall FWM field is given by

$$E_{\text{FWM,close}} = \frac{1}{A_{\text{eff,w}}} \left(n_{2,w} k_0 E_{1,\text{peak}}^2 E_{2,\text{peak}} L_w + n_{2,b} k_0 E_{1,\text{peak}}^2 E_{2,\text{peak}} L_b \right) \quad (4.3)$$

where $E_{\text{FWM,close}}$ corresponds to the value of FWM when the bulk sample is located at the waveguide's output.

The observation of the FWM is made through the detection of the beat note amplitude $i_{\text{FWM-LO}} \propto E_{\text{FWM}} E_{\text{LO}}$. This means the ratio between the measured photocurrents due to the contributions $E_{\text{FWM,close}}$ and $E_{\text{FWM,far}}$ (Eq. (4.2) and Eq. (4.3)) is given by

$$\frac{i_{\text{FWM-LO,close}}}{i_{\text{FWM-LO,far}}} = \frac{E_{\text{FWM,close}} E_{\text{LO}}}{E_{\text{FWM,far}} E_{\text{LO}}} = \frac{E_{\text{FWM,close}}}{E_{\text{FWM,far}}} = \frac{\frac{1}{A_{\text{eff,w}}} \left(n_{2,w} k_0 E_{1,\text{peak}}^2 E_{2,\text{peak}} L_w^2 + n_{2,b} k_0 E_{1,\text{peak}}^2 E_{2,\text{peak}} L_b^2 \right)}{\frac{1}{A_{\text{eff,w}}} n_{2,w} k_0 E_{1,\text{peak}}^2 E_{2,\text{peak}} L_w^2}$$

$$\Downarrow$$

$$\frac{E_{\text{FWM,close}}}{E_{\text{FWM,far}}} = \frac{n_{2,w} \cdot L_w + n_{2,b} \cdot L_b}{n_{2,w} \cdot L_w} = 1 + \frac{n_{2,b} \cdot L_b}{n_{2,w} \cdot L_w} \quad (4.4)$$

Most noticeably from Eq. (4.4): the nonlinear refractive index of the waveguide $n_{2,w}$ is determined without measuring the laser parameters. This happens when the nonlinear refractive index of the bulk sample $n_{2,b}$ and the lengths of both samples (L_b, L_w) are known.

I called this method *Referencing to Bulk Sample* (ReBuS).

By ReBuS, the laser parameters, such as excitation peak amplitude and a need to determine the shape of the pulse are ruled out and easily measurable quantities such the samples' length and the well-known nonlinearity of the bulk material are left.

Imaging system

To ensure the same mode field areas in both samples, i.e. $A_{\text{eff,b}} = A_{\text{eff,w}}$ (Eq. (4.3)), a 1:1 imaging system is used as schematically depicted in Fig. 4.2. The mode field area of the waveguide's output $A_{\text{eff,w}}$ is imaged 1:1 to its focal plane. The bulk sample is longitudinally shifted around the focal plane and as a result its mode field area ($A_{\text{eff,b}}$) changes. The 1:1 imaging approach (Fig. 4.2) yields a clear signal maximum as a function of z-position as opposed to a simple butt-coupling scheme (Fig. 4.1).

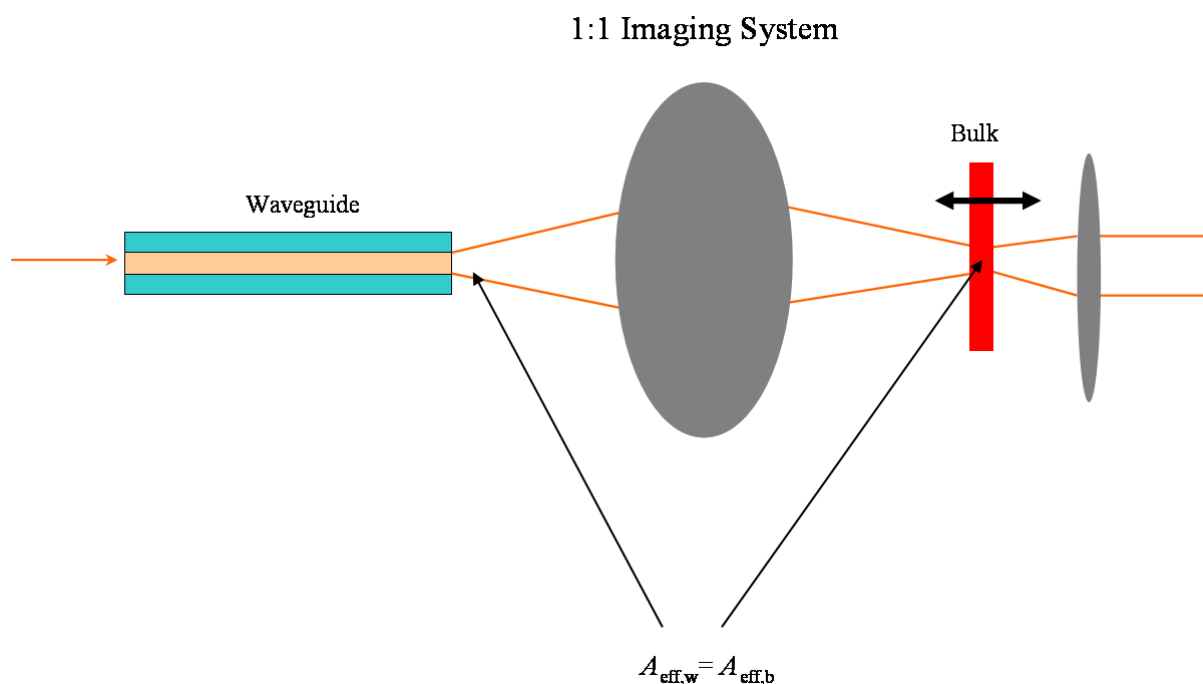


Fig. 4.2. Principle scheme of the 1:1 imaging system. The condition $A_{\text{eff,w}} = A_{\text{eff,b}}$ is satisfied when the bulk is located in focal plane.

Two off-axis parabolic (OAP) mirrors and two flat mirrors are used in order to implement the imaging system. This setup is shown in Fig. 4.3. The employed OAP mirror is a type of mirror that focuses an incident collimated light to an angle of 90° . The mirror is gold coated to maximize reflection at 1580 nm. The advantage of using the OAP mirrors instead of ordinary lenses is that the OAP does not have chromatic aberrations. The alignment of the OAP mirrors is not trivial, since any small deviation of the beam from the proper position on the paraboloid leads to a large imaging error [Burk09]. For this reason, a procedure for the alignment and its verification of the 1:1 imaging system has been developed.

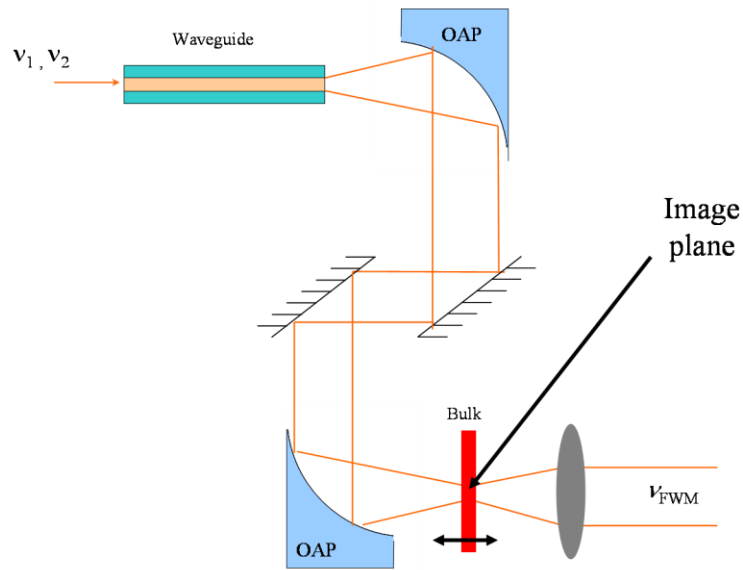


Fig. 4.3. Implementation of the 1:1 imaging system. The 90° off-axis parabolic mirror (OAP) does not have chromatic aberrations opposed to the ordinary lenses. The overall power transmission factor of the 1:1 imaging system is $T_{IS} = 0.81$.

For configuration of the 1:1 imaging system a separate alignment of the two OAP mirrors is necessary. This is done with the help of the setup that is shown in Fig. 4.4. Besides the OAP mirror, the setup includes a retroreflector, a single-mode waveguide, and a beam splitter. The optical properties, such as reflection and transmission coefficients of these components, have been measured previously and hence they are known. The measured power from the beam splitter's reflected light (P_{out} in Fig. 4.4) is equal to the power that is measured in front of the retroreflector (P_{in}) multiplied by the reflection coefficients of the retroreflector, the OAP, and the beam splitter. The coupling efficiency back into the waveguide is not taken into account, since this is unity for aligned properly OAP mirror.

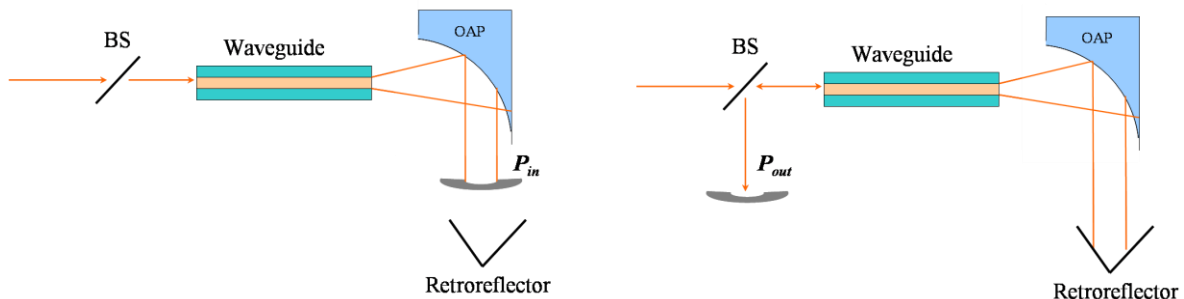


Fig. 4.4. The setup for the alignment of the OAP mirror is shown. The power that is measured from the beam splitter's reflected light (P_{out}) is equal to the power that is measured in front of the retroreflector (P_{in}) multiplied by the reflection coefficients of the retroreflector, the OAP, and beam splitter. The coupling coefficient due to the waveguide is not taken into account, since it is a unity for the aligned properly OAP.

The second OAP mirror is aligned in the similar way with the help of an auxiliary single-mode waveguide with comparable optical parameters. Both flat mirrors (Fig. 4.4) are used to align the collimated light between the OAP mirrors. As a final step to estimate the quality of the 1:1 imaging, a flat mirror is inserted instead of the auxiliary waveguide. The effective coupling efficiency is 90%. The imperfect 1:1 imaging is mainly due to the scattered light from the OAP mirrors. The coupling efficiency of 90% means that the difference in the effective mode areas between both samples is not larger than 10%.

Butt-coupling configuration

In principle, in order to compare between the samples, the bulk sample can be placed directly behind the waveguide. However, the butt-coupling configuration that is depicted in Fig. 4.1 has disadvantages. First of all, to locate the bulk sample directly behind the waveguide output might be difficult, e.g. if the waveguide is angle cleaved. An additional constraint of the butt-coupling configuration is due to Fabry-Perot (FP) resonances that might arise between the waveguide and bulk surfaces, as schematically depicted in Fig. 4.5a. Both excitation fields are modulated due to FP resonances which leads to a modulation of the heterodyne beat amplitude. The amplitude of the FP resonances is increased when the distance ' d_{FP} ' is comparable to the coherence length. With the pulse parameters that are used here, a coherence length of about 30 μm is obtained. This means that when the bulk sample is close to the waveguide's output ($A_{\text{eff,b}} \gtrsim A_{\text{eff,w}}$), these resonances contribute significantly to E_{FWM} . This happens, since the optical excitation fields are modulated in the FP resonator and behave in similar way as a FWM that is generated in the samples.

The FP fringes are indeed observed and are shown in Fig. 4.5b. One observes the amplitude change at heterodyne beat amplitude as a result of shifting the bulk sample toward and away from the waveguide's output. Similar changes were observed when measuring the beat notes between the excitation fields. Instead, by using the 1:1 imaging system, the FP fringes are avoided in such way that on the one hand, the distance between the surfaces of the samples is sufficiently longer than the coherence length to efficiently rule out the FP effects, but on the other hand, the condition $A_{\text{eff,b}} = A_{\text{eff,w}}$ is satisfied.

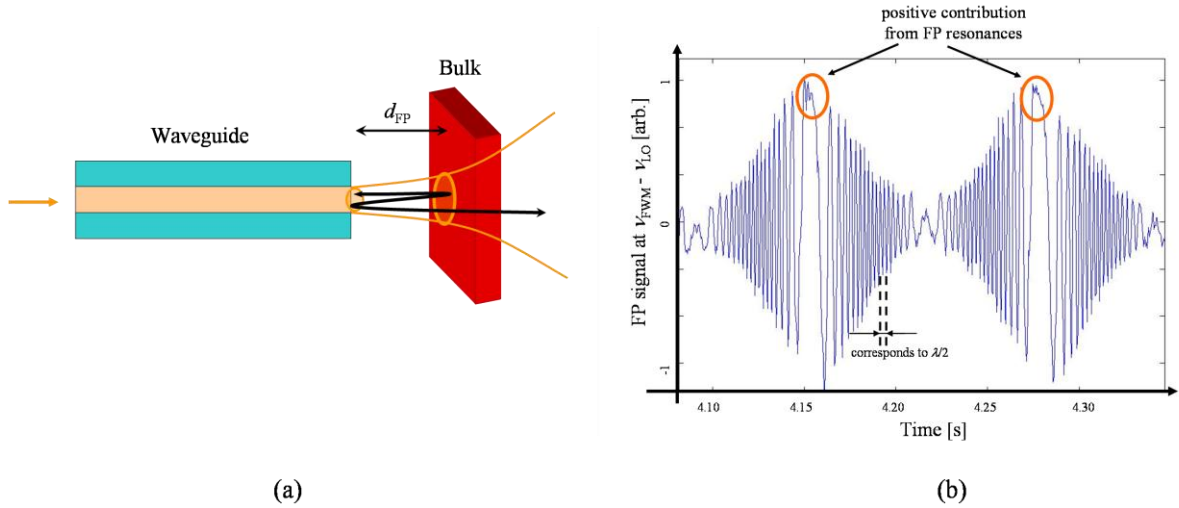


Fig. 4.5 (a). Using the butt-coupling configuration, unwanted Fabry-Perot resonances arise when the confocal parameter of the waveguide is comparable to the coherence length.

Fig. 4.5 (b). The contribution of the unwanted FP resonances to the overall signal at $\nu_{\text{FWM}} - \nu_{\text{LO}}$ varies depending on the distance between the waveguide and the bulk surfaces. For example, a positive contribution from the FP resonances is marked in the figure when the bulk sample is close to the waveguide's output. The distance between global maximum and minimum is equal to the distance between the samples' surfaces. The distance between two neighbouring local maxima is equal to half wavelength. The unwanted FP resonances are avoided using 1:1 imaging system.

Gouy phase shift for the imaging system

A Gouy phase has to be considered when applying a 1:1 imaging system, since an electromagnetic (or acoustic) wave experiences such a phase shift when travelling along the waist region [Rubi38, Boyd80]. The spatial variation of the wave phase $\psi(z)$ relative to the infinite plane wave is given by

$$\psi(z) = -\arctan(z/2N_c) \quad (4.5)$$

This means that the excitation field experiences a phase shift of $-\arctan(z/2N_c)$, when propagating through the focus. The nonlinear and the excitation fields might experience different Gouy phase shifts. For example, for the case of the third-harmonic generation ($\nu = 3\nu_1$), the nonlinear field has Gouy phase shift of $\psi(z) = -3\arctan(z/2N_c)$, so that the phase difference relative to the excitation field is $-2\arctan(z/2N_c)$. However, the FWM nonlinear field at $\nu_{\text{FWM}} = 2\nu_1 - \nu_2$ has Gouy phase shift of

$$\psi(z) = -2 \cdot \arctan(z / 2N_c) + \arctan(z / 2N_c) = -\arctan(z / 2N_c) \quad (4.6)$$

and thus equal to the Gouy phase shift that experience the excitation fields. Therefore, there is no phase flipping between the nonlinear and excitation fields caused by the Gouy phase. This means that the nonlinear fields at $\nu_{\text{FWM}} = 2\nu_1 - \nu_2$ that are generated in the waveguide and in the bulk sample experience the same Gouy phase shift.

Geometrical requirements for the samples using OAP mirrors

The OAP mirrors are free of chromatic aberrations, as it was mentioned earlier. However, this type of mirror can image properly only a single point. Therefore, the spot that comes out of waveguide would preferably have a round-uniformly distributed shape, i.e. the fundamental mode profile so that its image is a single point. Image of the beam profile of the waveguide that guides higher-order modes would not have a single point, so that OAP mirrors are not suitable for the imaging of the waveguides that do not guide single mode.

Fig. 4.6 shows the simulation of the overall FWM signal for two different values of bulk thickness (L_b) and confocal parameter N_c , assuming a Gaussian beam profile⁹. The simulations give an intuition of how the overall FWM signal changes as a function of propagation direction (z), bulk thickness, and confocal parameter of the waveguide. It is observable that the contribution of the bulk sample changes when it is shifted along the focus: overall FWM signal is solely determined by the nonlinearity of the waveguide when the bulk

⁹ The mathematical treatment of the propagation of the light with Gaussian profile along the focus is found in references [Ward69, Bjor75]. For the case of nearly-degenerate FWM, $\nu_2 - \nu_1 \ll \nu_1, \nu_2$, the overall FWM signal as a function of the bulk thickness L_b and the confocal parameter N_c can be expressed as

$$E_{\text{FWM}}(z', L_b, N_c) \propto \int_{-\zeta}^{\zeta} \frac{1}{(1 + \varepsilon'^2)} d\varepsilon'$$

where z' is a position of the bulk sample relative to the focal plane, $\zeta = 2z' / N_c$, and $\varepsilon = 2(L_b - z') / N_c$.

is located far from the focus and for the case where the bulk is close to the waveguide's output, the contribution is not negligible. The bulk sample contributes noticeably to the FWM signal when it is placed within the range $(L_b + N_c)$ around the focal plane. At the focal plane ($z = 0$), the FWM signal due to the nonlinearity of the bulk sample contributes maximally to the overall FWM. For confocal parameter that is shorter than bulk thickness, the value of the confocal parameter should be used for L_b in Eq. (4.4). This is due to the fact that the entire confocal parameter is contained within the bulk sample when the latter is in the vicinity of the focal plane.

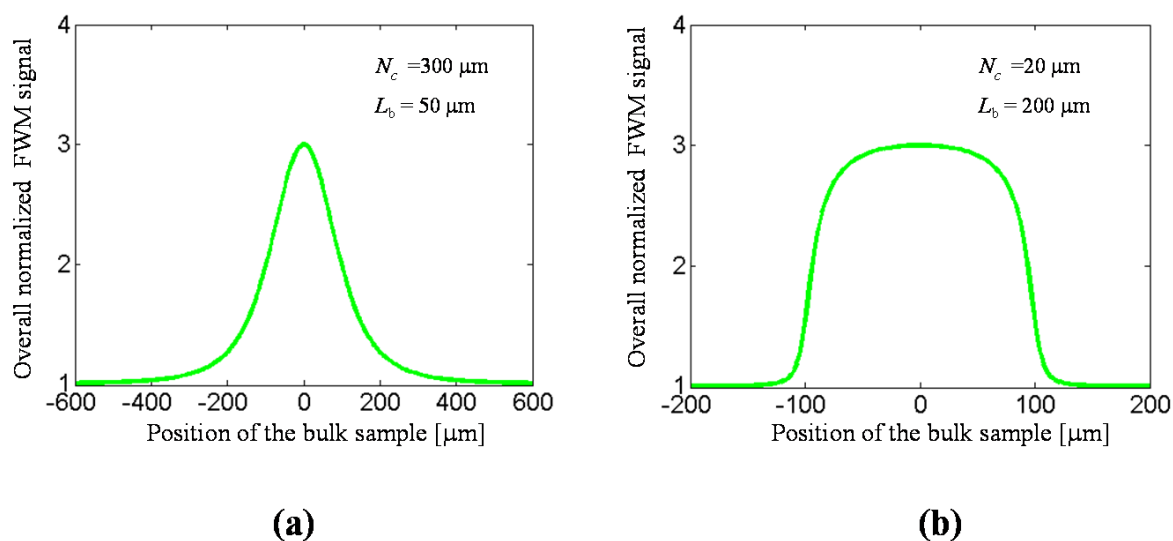


Fig. 4.6. The bulk sample is shifted along the focus ($z = 0$) and its contribution to the overall signal changes. Two cases for different values of confocal parameter (N_c) and bulk thickness (L_b) (for the ratio of 3) for Gaussian profile are shown. (a) the bulk is shorter than the confocal parameter. (b) the bulk sample is larger than the confocal parameter.

4.1 Summary & Conclusion

ReBuS allows investigation of fast nonresonant optical nonlinearity in waveguiding samples without measuring the laser parameters, such as peak amplitudes of the excitation fields by direct comparison to the nonlinearity of the bulk material.

A concept is developed that allows for detection of optical nonlinearities without characterizing the laser pulse. The name is “Referencing to Bulk Sample” (ReBuS): optical nonlinearity of the waveguide of interest is directly compared with an additional bulk sample with well-known optical properties under the same experimental circumstances. In my implementation, the bulk sample is placed at the focal plane of the waveguide’s output by using the 1:1 imaging system with OAP mirrors. This allows to investigate single-mode waveguides. The value of the FWM signal changes depending on the longitudinal position of the bulk with respect to the focal plane. Two measurements are required for the determination of the optical nonlinearity of the waveguide under test: one with the bulk sample shifted to the position where it has the same mode field area as waveguide, and hence contributes noticeably to the overall FWM signal, and the other with being shifted far from that position, and hence not contributing to the FWM.

Chapter 5

Experimental demonstration of ReBuS

In this chapter ReBuS is demonstrated experimentally. The experimental setup that explained in chapters 3 and 4, is schematically shown in Fig. 5.1.

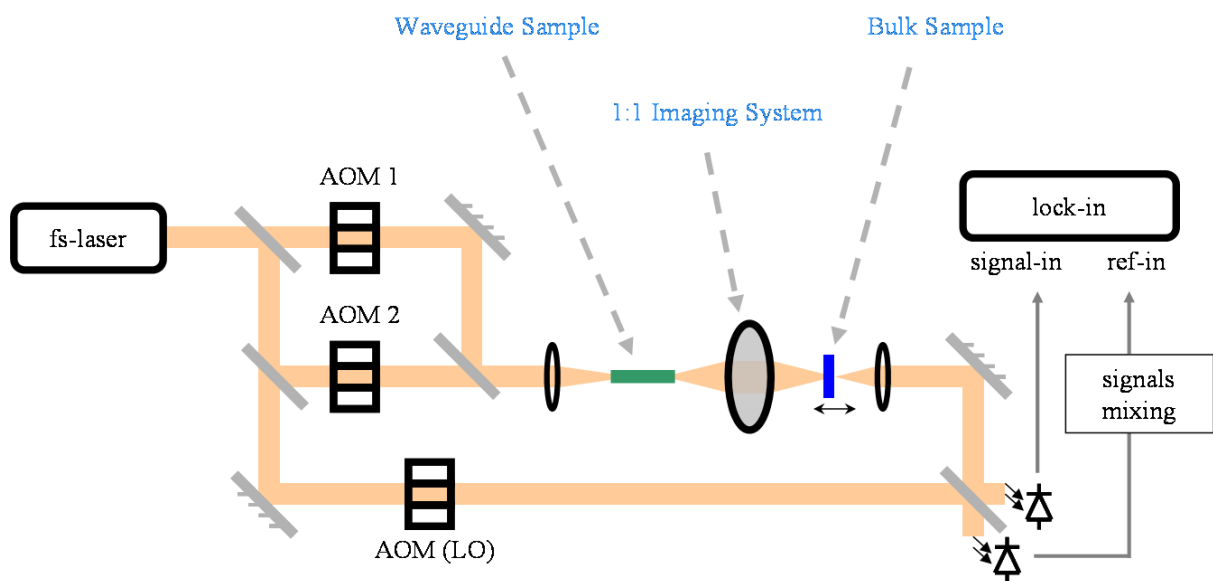


Fig. 5.1. Schematic setup of ReBuS for investigation of fast optical nonlinearities (compensation arm is not shown).

5.1 Experimental results for waveguides

Experimental results for SMF-28

To demonstrate the method experimentally, the nonlinearity of a short piece of standard optical fiber SMF-28 is measured and the results are shown in Fig. 5.2. A bulk made of fused silica material is used as reference sample. Using ReBuS, the nonlinear refractive index of the SMF-28 is found $n_{2,\text{SMF-28}} = 3 \cdot 10^{-20} \text{ m}^2 \text{ W}^{-1}$. This result is in agreement with the values measured in references [Stol78, Kato95]. The value is calculated using the following equation

$$\frac{E_{\text{FWM, close}}}{E_{\text{FWM, far}}} = \frac{n_{2,w} L_w + n_{2,b} L_b T_{\text{tot}}}{n_{2,w} L_w} \quad (5.1)$$

where T_{tot} is a transmission factor due to Fresnel losses of the samples and transmission of the imaging system¹⁰. The length of SMF-28 is $L_w = 9.5 \text{ mm}$ and the length of the fused silica bulk sample is $L_b = 25 \text{ } \mu\text{m}$.

¹⁰ It is necessary to take into account parameters due to the Fresnel losses and the transmission of the imaging system:

$$\frac{E_{\text{FWM, close}}}{E_{\text{FWM, far}}} = \frac{n_{2,w} L_w E_1^2 E_2 \sqrt{T_{\text{IS}}^3 T_{\text{aw}}^3 T_{\text{wa}} T_{\text{ab}} T_{\text{ba}}} + n_{2,b} L_b E_1^2 E_2 \sqrt{T_{\text{IS}}^3 T_{\text{aw}}^3 T_{\text{wa}}^3 T_{\text{ab}}^3 T_{\text{ba}}}}{n_{2,w} L_w E_1^2 E_2 \sqrt{T_{\text{IS}}^3 T_{\text{aw}}^3 T_{\text{wa}} T_{\text{ab}} T_{\text{ba}}}} \quad (5.2)$$

where the indices ‘a’, ‘w’, and ‘b’ stand for air, waveguide and bulk and T_{xy} is a Fresnel transmission coefficient of the surface between the materials x and y , and T_{IS} is the total transmission of the imaging system. The coefficients T_{xy} and T_{IS} enter with different powers in the contributions from the waveguide and the bulk samples, depending on whether they must be applied before or after the generation of the respective FWM field. The contribution of the Fresnel loss from the waveguide entrance surface affects the excitation intensity in both samples whereas the loss of the bulk exit surface reduces both FWM signals by the same factor. Therefore, these both effects cancel out in Eq. (5.1). The remained Fresnel coefficients are due to the light that comes out of the waveguide and enters the bulk sample. Hence, Eq. (5.2) is simplified to Eq. (5.1)

$$\frac{E_{\text{FWM, close}}}{E_{\text{FWM, far}}} = \frac{n_{2,w} L_w + n_{2,b} L_b T_{\text{IS}} T_{\text{wa}} T_{\text{ab}}}{n_{2,w} L_w} = \frac{n_{2,w} L_w + n_{2,b} L_b T_{\text{tot}}}{n_{2,w} L_w} = 1 + \frac{n_{2,b} L_b}{n_{2,w} L_w} T_{\text{tot}} \quad (T_{\text{tot}} = T_{\text{IS}} T_{\text{wa}} T_{\text{ab}})$$

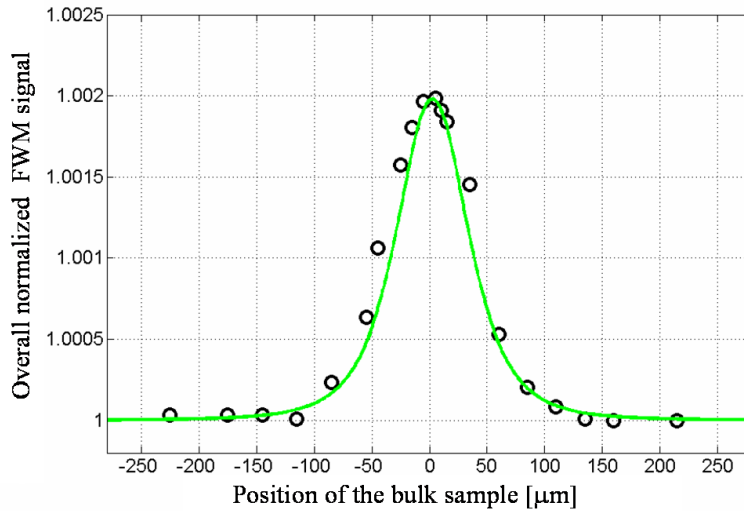
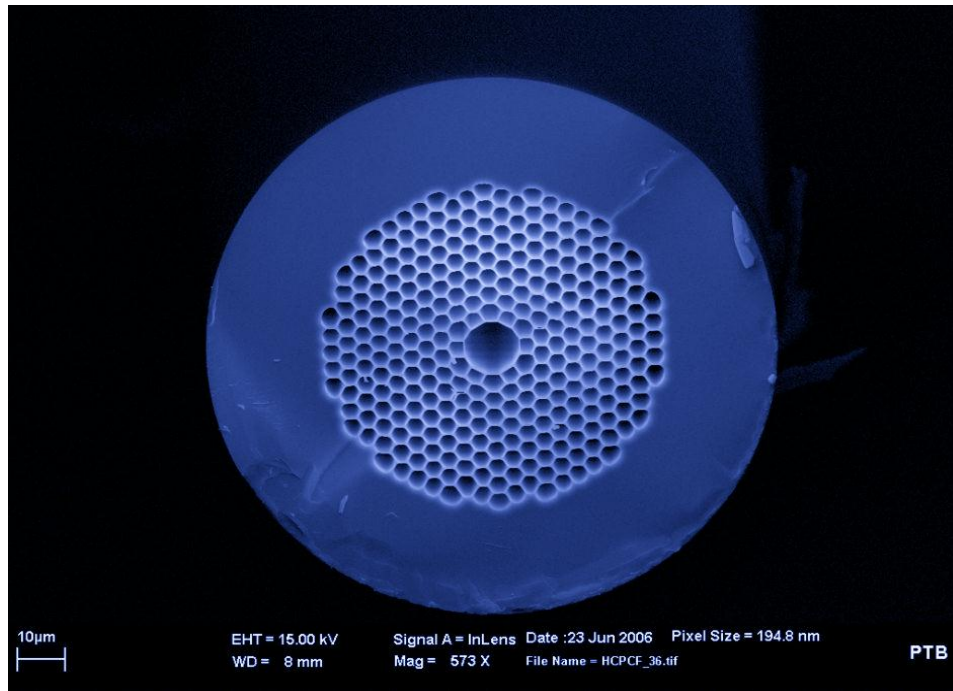


Fig. 5.2. Experimental results using ReBuS for SMF-28 fiber. A fused-silica bulk sample is shifted along the focus of the 1:1 imaged output of the SMF-28 fiber ($z=0$). Experimental results are depicted as circles. The theoretical solid curve has been calculated assuming a Gaussian beam

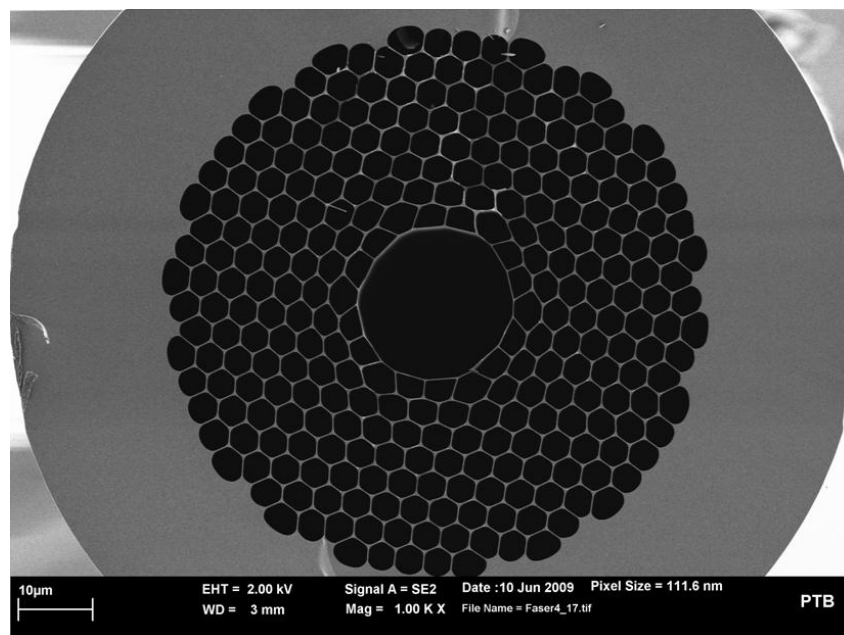
profile and confocal parameter of $110 \mu\text{m}$. The ratio 1.002 is given by $\frac{E_{\text{FWM, close}}}{E_{\text{FWM, far}}} = 1 + \frac{n_{2,b} L_b}{n_{2,w} L_w} T_{\text{tot}}$.

Experimental results for HC-PCF

The confinement of the light in the hollow-core photonic crystal fiber (HC-PCF) core is based on the photonic bandgap structure of the cladding (Fig. 5.3). The photonic bandgap is the spectral range, in which the light in the core propagates with minimal losses. The width, shape and central wavelength of the photonic bandgap change depending on the size of holes (hollow cells) in the periodic structure of the cladding, the holes' shape and distance between them (e.g. [Russ03]). Outside the bandgap, the light cannot be trapped in the core and leaks to the cladding where the attenuation is high. Within the bandgap, the light is localized within a vicinity of the core and the attenuation is small. The HC-PCFs that are shown in figures are single-mode fibers [Nktp01, Nktp02]. Scattering due to imperfections in the fiber microstructure and coupling of the fundamental mode to other confined modes, i.e. surface modes, which have a larger overlap with the core surrounding, determines a minimum level of the attenuation [Sait04]. Fig. 5.3 shows the pictures of the cross sections of two HC-PCFs with different core diameters (taken by a scanning electron microscope).



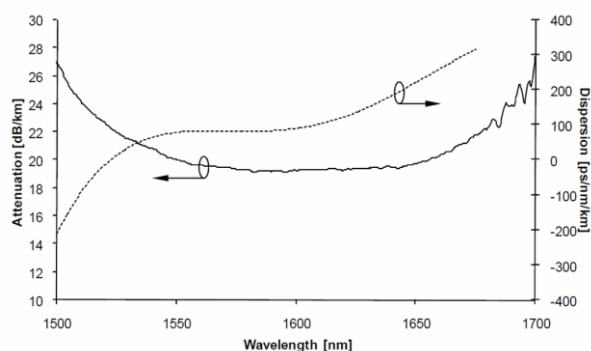
(a)



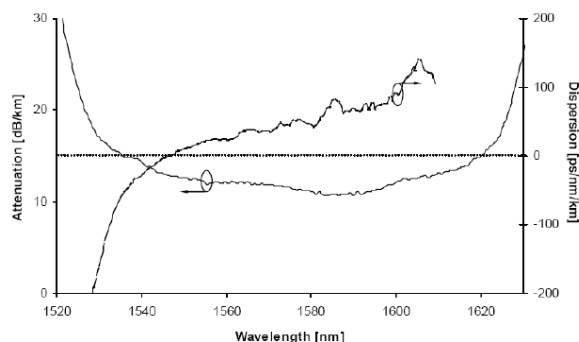
(b)

Fig. 5.3. A HC-PCF is a fiber that has a larger central hole, which is surrounded by the periodic cladding structure. A preform, from which a HC-PCF is drawn, is created by stacking together hundreds of hollow silica capillaries, so that the fiber has a 2D model of air holes along its length. The HC-PCF is produced by taking out several capillaries from the core region. (a) 7-cells fused silica made HC-PCF (HC-1550-02) with core diameter of 10 μm. (b) A fused silica made HC-PCF with 19 removed cells in the center (HC-1550-01). This corresponds to 20 μm diameter of the hollow core.

The dispersion properties of the fibers are shown in Fig. 5.4. The fiber with a core diameter of 10 μm is shown in Fig. 5.4a. This fiber guides a single mode around a wavelength of 1600 nm within its photonic bandgap. From the figure is observed that the bandgap width of the fiber is about 150 nm. The fiber with a core diameter of 20 μm is shown in Fig. 5.4b. It has a central wavelength around 1580 nm with a photonic bandgap width of about 80 nm. Around wavelength of 1580 nm the fiber with 20 μm has similar dispersion to the dispersion of a SMF-28 fiber. Also it is observable that around 1580 nm the fiber with 10 μm core diameter has a dispersion that is 5 times larger than that of the fiber with 20 μm core diameter.



(a)



(b)

Fig. 5.4. Dispersion and attenuation of the HC-PCFs. 7-cell HC-1550-02 (a) and 19-cell HC-1550-01 (b) (with permission from NKT Photonics). At wavelength 1580 nm the dispersion of 7-cell fiber is 5 times larger than of the 19-cell fiber. The dispersion of the 19-cell fiber is comparable to the dispersion of the SMF-28. Starting from wavelength of 1550 nm the dispersion of the fibers is anomalous.

Fig. 5.5 shows the experimental results for the HC-PCF with 10 μm core diameter. From the figure is observable that when the bulk sample is located outside the focal region, its contribution is negligible. In the vicinity of the focal plane (around $z = 0$), the overall FWM signal becomes larger owing to the contribution from the bulk sample. This range is given by

the overlap region between the bulk sample and the confocal parameter of the HC-PCF $L_b + N_c$. The thickness of the bulk sample is $L_b = 500 \mu\text{m}$, which is about ten times the confocal parameter ($N_c = 60 \mu\text{m}$ [Nktp01]). Therefore, this range has approximately the width of this sample, $L_b + N_c \approx L_b$, i.e. about $500 \mu\text{m}$.

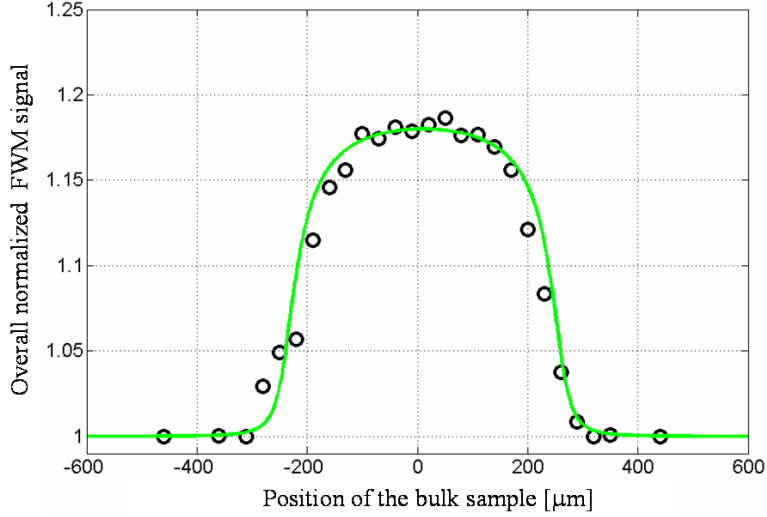


Fig. 5.5. Experimental results using the ReBuS for the HC-PCF (7-cell). A $500 \mu\text{m}$ fused-silica bulk reference sample is shifted along the focus. Experimental results are depicted as circles. The theoretical solid curve has been calculated assuming a Gaussian beam profile and the confocal parameter of $60 \mu\text{m}$. The dispersion properties have to be taken into account when measuring the nonlinearity. The nonlinearity of the HC-PCF is found to be 1300 times smaller than that of the fused silica.

Using ReBuS the nonlinearity of the HC-PCF with $10 \mu\text{m}$ core diameter is found to be 1300 times smaller than in fused silica. In this measurement, the length of the HC-PCF is 20.5 cm.

The effective length due to the high dispersion of this fiber ($D = 100 \frac{\text{ps}}{\text{km nm}}$) is

$L_{\text{eff,HC-PCF-02}} = 8.1 \text{cm}$ and is shorter than its physical length so that $L_{\text{eff,w}}$ instead of L_w is used for the calculations in Eq. (5.1), as explained below.

Effective length calculation for waveguide having high dispersion

In case of long enough waveguide samples, where the dispersion cannot be neglected, the effective length of the waveguide $L_{\text{eff,w}}$ is used in Eq. (5.1). The effective length is defined as a length at which the optical power of the generated FWM $P_{\text{FWM,eff}}$ is reduced to $1/e$ of its maximum value:

$$L_{\text{eff,w}} = z \left(P_{\text{FWM,eff}} = 1/e \cdot P_{\text{FWM,max}} \right)$$

The question is when $P_{\text{FWM,eff}} = 1/e \cdot P_{\text{FWM,max}}$? The FWM optical power is proportional to the excitation (peak) optical powers as $P_{\text{FWM}} \propto P_{1,\text{peak}}^2 P_{2,\text{peak}}$. The dispersion changes the pulse duration and the peak optical power is inverse proportional to the pulse duration: $P_{\text{peak}} \propto \frac{1}{\tau_p}$ (Eq. (3.10)). Therefore, the FWM signal is inversely proportional to the 3rd power of the pulse duration τ_p , i.e. $P_{\text{FWM,eff}} = 1/e \cdot P_{\text{FWM,max}}$ is satisfied when

$$\frac{1/e \cdot P_{\text{FWM,max}}}{P_{\text{FWM,eff}}} = \frac{1/e \cdot \left(\frac{1}{\tau_{\text{min}}} \right)^3}{\left(\frac{1}{\tau_{\text{eff}}} \right)^3} = 1$$

$$\Downarrow$$

$$\tau_{\text{eff}} = \tau_{\text{min}} \cdot e^{1/3}$$

where τ_{eff} is the pulse duration, at which the peak power of the FWM signal $P_{\text{FWM,eff}}$ is reduced to 1/e of its maximum value and τ_{min} is the pulse duration at the fiber input. By assuming nearly transform limited pulses, the temporal broadening of the pulse inside the fiber is given by [Agra89]

$$\frac{\tau_{\text{eff}}}{\tau_{\text{min}}} = \left[1 + \left(\frac{\left| \frac{D\lambda^2}{2\pi c} \right| L_{\text{eff,w}}}{\tau_{\text{min}}^2} \right)^2 \right]^{1/2} \quad (5.3)$$

where D is the dispersion parameter and c is the speed of light. From Eq. (5.3) the effective length of the waveguide $L_{\text{eff,w}}$ is calculated, since all other parameters are known.

Correction factor for the bulk sample due to waveguide having high dispersion

The dispersion has an influence not only on the waveguide's effective length, but also on the bulk sample. Therefore, a correction factor due to dispersion for the bulk sample B_p has to be taken into account, as explained below.

The peak optical power that enters the bulk sample is different from the power that enters the waveguide and is reduced due to the dispersion in the waveguide. The dispersion correction factor is given by $B_p \equiv \frac{\tau_{\max}}{\tau_{\min}}$, where τ_{\max} and τ_{\min} are pulse durations at the input and output of the fiber. The pulse duration of the pulse at the waveguide output (in front of the bulk sample) τ_{\max} is calculated using Eq. (5.3), where $L_{\text{eff,w}}$ is replaced by L_w , and τ_{eff} is replaced by τ_{\max} .

So if the waveguide's length is long enough not to neglect the dispersion, the expression from Eq. (5.1) takes form of

$$\frac{E_{\text{FWM, close}}}{E_{\text{FWM, far}}} = \frac{n_{2,w}L_{\text{eff,w}} + n_{2,b}L_bT_{\text{tot}} / \sqrt{B_p^3}}{n_{2,w}L_{\text{eff,w}}} \quad (5.4)$$

For 20.5 cm short HC-PCF with 10 μm core diameter and the pulse parameters used in the experiment, the correction factor is $B_p = 2.6$ and the effective length of the fiber is $L_{\text{eff}} = 8.1\text{cm}$.

From the discussion above we can conclude that if the length of the waveguide is long enough not to neglect the dispersion, the pulse duration at the waveguide's input and output has to be known. Hence, it is desirable that the waveguide would be sufficiently short in order to neglect the changes of the pulse duration due to dispersion effects.

5.2 Phase-resolved concept

In chapter 4 it was assumed for the sake of simplicity, that the nonlinear fields from the samples are in phase, i.e. do not have nonlinear absorption ($\beta = 0$, $n_2 \neq 0$). By heterodyning one detects the beat note amplitude $\text{Re}[E_{\text{FWM}}E_{\text{LO}}^*]$. Generally, for samples that have non-negligible absorption, i.e. $\beta \neq 0, n_2 \neq 0$, E_{FWM} becomes complex ($\chi^{(3)}$ is a complex number). Both quadrature¹¹ outputs of the lock-in, x and y , are detected. By defining: $E_{\text{FWM}}E_{\text{LO}}^* \equiv x + iy$, the information about the complex field E_{FWM} and hence about both nonlinear refractive index and nonlinear absorption is obtained, since $x = \text{Re}[E_{\text{FWM}}E_{\text{LO}}^*] = \text{Re}[x + iy]$, $y = \text{Im}[E_{\text{FWM}}E_{\text{LO}}^*] = \text{Re}[-i(x + iy)]$.

Both quadrature components of the beat note $E_{\text{FWM}}E_{\text{LO}}^*$ are phase-sensitively recorded with the help of a lock-in amplifier. The phase and the amplitude of the local oscillator are constant relative to the nonlinear field, which means both quadrature components of E_{FWM} can be determined. Hence, the heterodyne technique with lock-in enables not only efficient discrimination of the FWM field against the excitation fields, but also simultaneous detection of the nonlinear refractive index n_2 and the nonlinear absorption coefficient β . A representation of ReBuS in complex frame is depicted in Fig. 5.6. Two points (A and B) in the figure indicate two measurements: one measurement includes the FWM field from the waveguide ($E_{\text{FWM, far}} = E_{\text{FWM, waveguide}}$) and the other one contains additionally the FWM field from the bulk reference sample ($E_{\text{FWM, close}} = E_{\text{FWM, waveguide}} + E_{\text{FWM, bulk}}$). By the vector \overline{AB} in Fig. 5.6 is denoted the bulk shift toward the focal plane.

¹¹ Quadrature components: phase shifted by 90° in respect to each other.

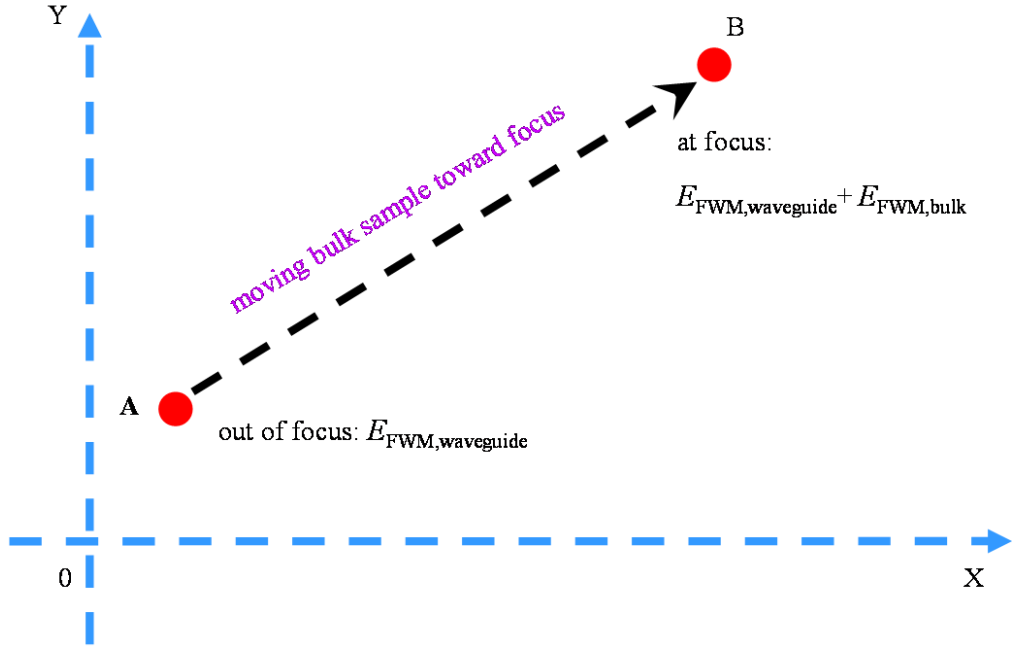


Fig. 5.6. Representation of ReBuS in the complex frame (X,Y). Two red points indicate two required measurements. The dashed vector is the complex trajectory of the bulk sample moving towards the focus (\overline{AB}).

The relative phase between the reference input and the signal input to the lock-in is constant during the measurements, but might vary due to experimental setup, e.g. when adjusting the overlap between the involved fields or due to the electronics for the RF lock-in reference input, e.g. different cable lengths between PD2 and the RF lock-in. This leads to phase offset that might change from experiment to experiment. This dependence of the uncalibrated phase offset is removed using ReBuS.

The concept for elimination of the phase offset is depicted in the complex frame in Fig. 5.7. By ReBuS, the nonlinear properties, i.e. real and imaginary parts of the reference bulk sample susceptibility are known. Therefore, the complex FWM field that is generated in the bulk sample, which is denoted by the vector \overline{AB} is also known. This allows to rotate the ‘uncalibrated’ complex coordinate frame (X,Y) such that the real and imaginary parts of $\chi^{(3)}$ are represented in ‘calibrated’ complex coordinate frame (X',Y'). It is convenient, but not mandatory, to choose the reference bulk sample with $\beta = 0$ and $n_2 \neq 0$, i.e. a purely real $\chi^{(3)}$. In this case, the coordinate frame is rotated such that \overline{AB} is parallel to the real axis (X' in Fig. 5.7). Using this procedure, the constant but hitherto uncalibrated phase offset is eliminated and the real and imaginary parts of $\chi^{(3)}$ are correctly represented in the rotated (‘calibrated’) complex coordinate system.

The projection of the FWM contribution from the waveguide sample (\overline{OA} in Fig. 5.7) on the ‘calibrated’ complex coordinate frame depicts the real and imaginary parts of the FWM for the case that the nonlinear contribution from the reference sample is purely real, i.e. does not contain the nonlinear absorption. Without ReBuS, i.e. only by heterodyning, the uncalibrated phase offset (θ) has to be known, but as was mentioned earlier, a slight modification in the setup, e.g. changing the cable connecting between PD2 and RF lock-in imposes to re-calibrate the phase, which is impractical.

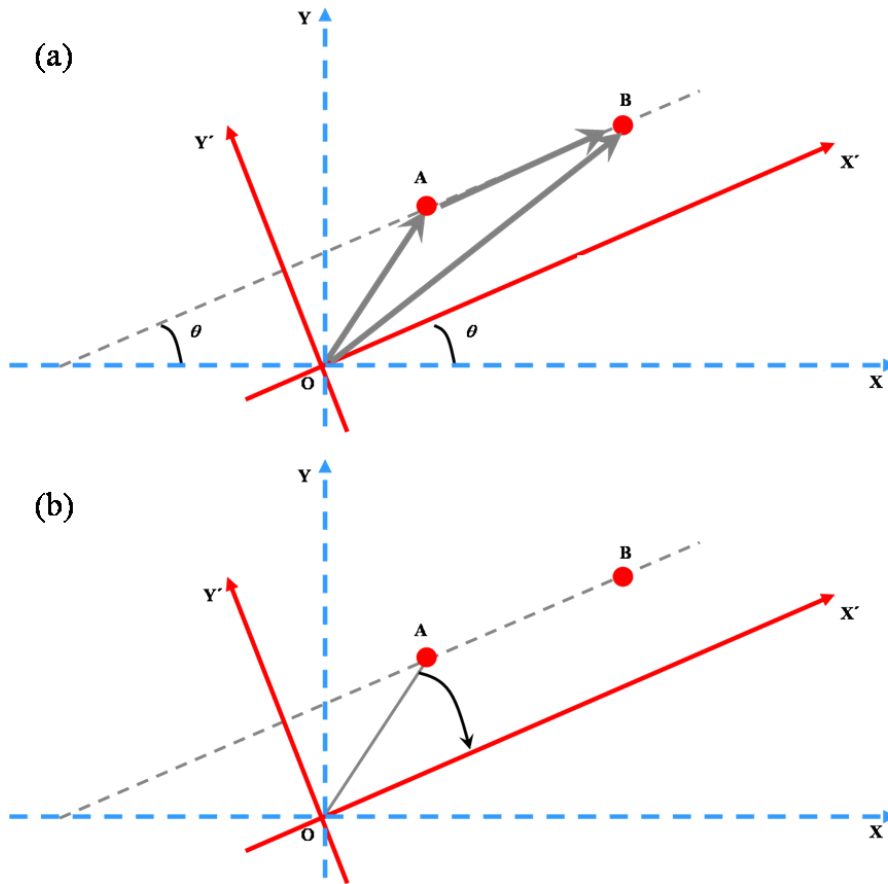


Fig. 5.7. The concept for phase calibration. (a) The value of the FWM field from both reference bulk and waveguide samples ($E_{\text{FWM,waveguide}} + E_{\text{FWM,bulk}}$) is indicated by vector \overline{OB} . The FWM signal, when only the contribution from the waveguide is measured ($E_{\text{FWM,far}} = E_{\text{FWM,waveguide}}$) is indicated by vector \overline{OA} . The original axes X, Y are rotated to the new axes X' and Y' , so that X' axis is parallel to the vector \overline{AB} . (b) The projection of the vector \overline{OA} on X' is proportional to $\text{Re } \chi^{(3)}$ for the case that the bulk sample (\overline{AB}) has negligible nonlinear absorption.

Phase-resolved detection for HC-PCF

The nonlinearity of the HC-PCF $n_{2,\text{HC-PCF}}$ can be expressed as an effective nonlinearity $n_{2,\text{eff, HC-PCF}}$. This notation is used due to the fact that the interaction between the surface modes and the fundamental mode in fiber might lead to a complex value of the FWM field that propagates in the core. This coupling between the modes may lead to complex values of $n_{2,\text{eff, HC-PCF}}$, even if the material contribution is real.

To testify this hypothesis, a short piece (21 mm) of the HC-PCF with core diameter of 20 μm and a 25 μm short piece of fused silica bulk are selected. The low dispersion of this 21 mm short HC-PCF allows to neglect the changes of the pulse duration due to dispersion effects.

Fig. 5.8 shows the experimental results. Around a wavelength of 1580 nm the nonlinear absorption of the fused silica is negligible [e.g. Mila98], i.e. $\beta = 0$ and $n_2 \neq 0$. This means, the axis that is parallel to the FWM from the bulk sample (\overline{AB}) is proportional to the real part of $\chi^{(3)}$. From the figure is observable that the vectors \overline{OA} and \overline{OB} lie on the same axis. (vector \overline{OA} depicts the complex FWM field only from the fiber). This result means that $n_{2,\text{eff, HC-PCF}}$ is a real value and the interaction between the fundamental and surface modes within the bandgap does not lead to complex nonlinearities in HC-PCF.

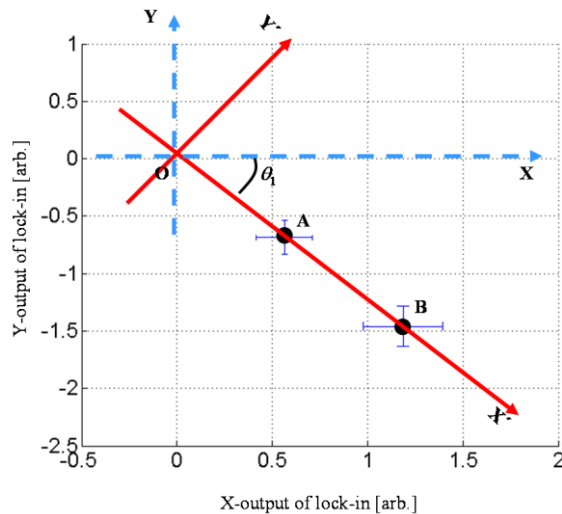


Fig. 5.8. The experimental results obtained from the HC-PCF (19-cell). Vectors \overline{OA} and \overline{OB} lie on the same axis, therefore the value of the nonlinear contribution from HC-PCF is real (θ_1 is uncalibrated phase offset).

Phase-resolved detection for bulk sample

In the following is shown that ReBuS is applicable for phase-resolved measurements in bulk samples and NFOM can be directly deduced graphically.

The roles of the sample with well-known properties and the ‘waveguide under test’ are interchanged. This configuration is depicted in Fig. 5.9, where the waveguide is the reference sample with well-known properties. Let us assume without loss of generality, that the waveguide has a purely real-valued $\chi^{(3)}$. Due to this fact, the nonlinear contribution from the waveguide ($E_{\text{FWM, waveguide}}$, vector \overline{OA}) is proportional to the real part of $\chi^{(3)}$, i.e. the coordinate system (X', Y') proportional to the real and imaginary parts of $\chi^{(3)}$. For the bulk sample under test having a non-vanishing nonlinear absorption, the vector \overline{AB} ($E_{\text{FWM, bulk}}$) is expected to lie outside the axis X' , as illustrated in Fig. 5.9. Note, that a purely real-valued $\chi^{(3)}$ is not a necessary condition for the reference waveguide sample as long as its imaginary part is known as well.

The ReBuS method can be employed to measure the nonlinearities in bulk materials. Both components n_2 and β of the bulk sample under test are compared to the value of the waveguide with well known optical properties. The use of the waveguide as reference sample ensures the same mode area in both samples. The direct comparison of nonlinearities allows a straightforward deduction of the nonlinear figure-of-merit.

The ‘in-phase’ (X') and ‘quadrature’ (Y') axes of the FWM-signal from the waveguide are proportional to $k_0 n_2$ and β (both having the same units), respectively. Therefore, NFOM can be easily deduced from the ratio of the projection of the vector \overline{AB} on the axes X' and Y' , as schematically shown in Fig. 5.9. It is interesting to note that it is sufficient to know that the waveguide does not have nonlinear absorption so that the exact value of the nonlinear refractive index of the reference waveguide does not play a role for the determination of the nonlinear figure-of-merit.

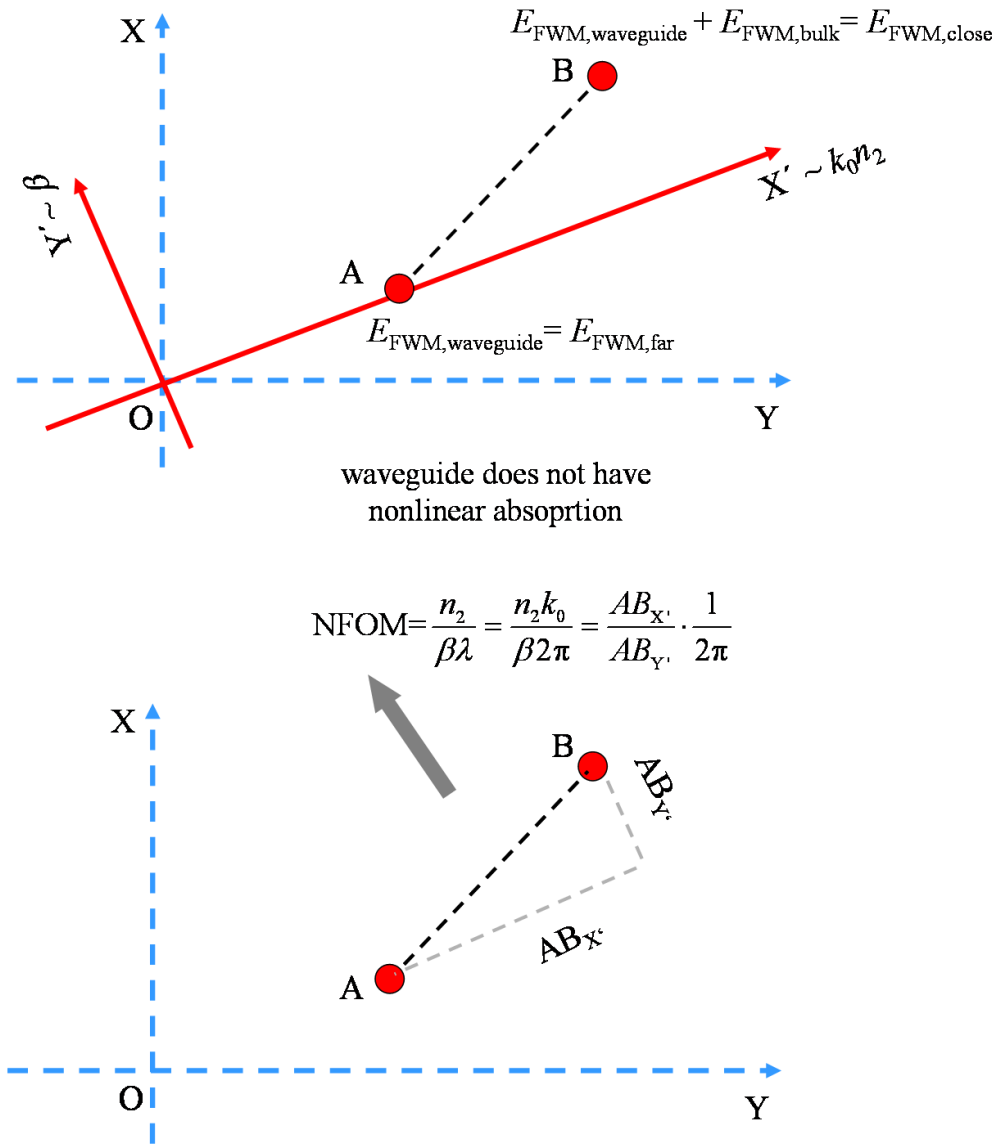


Fig. 5.9. The roles of the sample with well-known properties and the ‘waveguide under the test’ are interchanged. Vector \overline{AB} , i.e. $E_{\text{FWM,bulk}} = E_{\text{FWM,close}} - E_{\text{FWM,far}}$ is the contribution from the bulk under test. $E_{\text{FWM,far}}$ is the contribution from the reference waveguide. Assuming that the reference waveguide has a negligible nonlinear absorption, a straightforward deduction of NFOM from the graph is performed easily.

Fig. 5.10 shows the experimental results in ‘calibrated’ (X’,Y’) complex coordinate frame for the silicon bulk sample. The values are normalized to the FWM signal from the reference waveguide SMF-28. The beat note amplitude is measured twice: when the bulk is at the focal plane and when it is far from the plane. The nonlinear figure of merit of silicon is straightforwardly determined from the graph: $\text{NFOM} = \frac{n_2}{\beta\lambda} = \frac{n_2 k_0}{2\pi\beta} = 0.37$. This result is in good agreement with the results published in [Dinu03] and [Linz07].

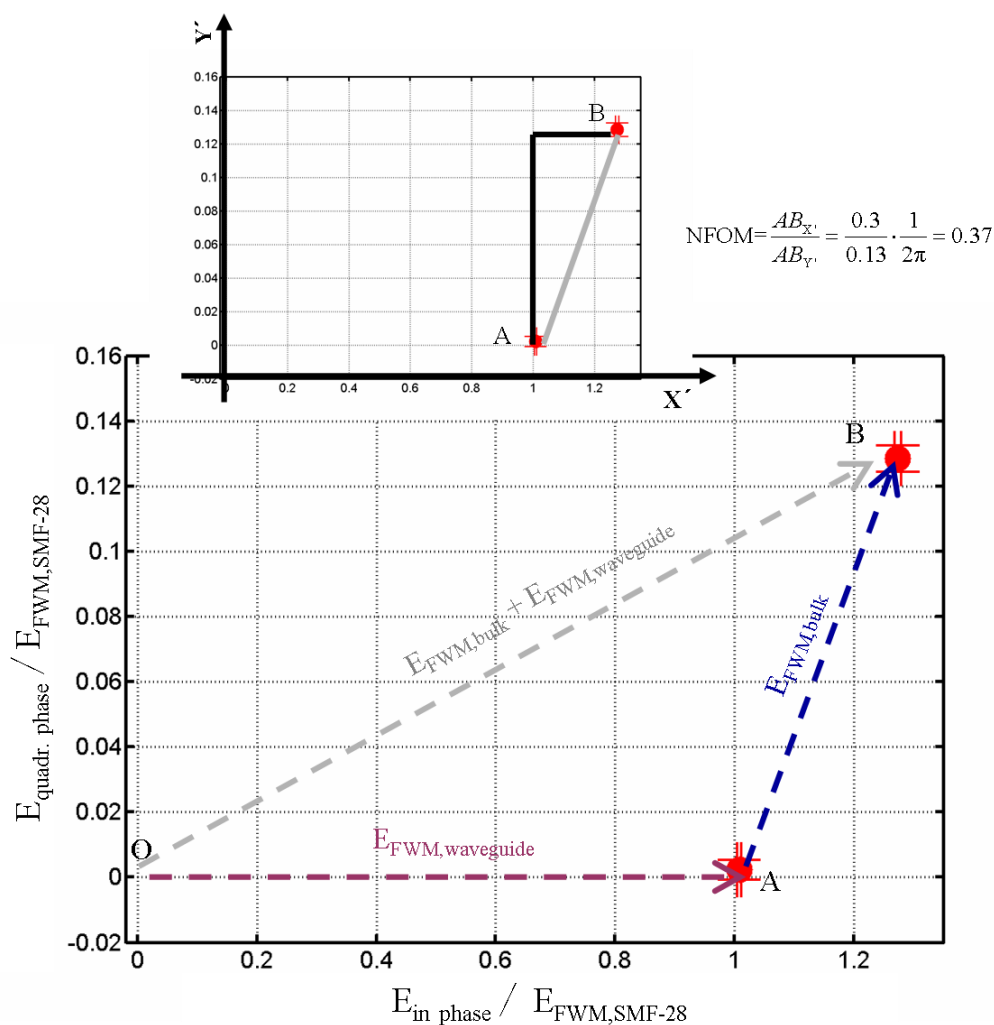


Fig. 5.10. Experimental results of the silicon bulk sample in rotated (‘calibrated’) coordinate frame. The observed values are normalized to the SMF-28 FWM-signal. The obtained nonlinear figure-of-merit is $\text{NFOM} = \frac{n_2 k_0}{\beta 2\pi} \cdot \frac{1}{2\pi} = 0.37$.

Precis

A versatile tool, Referencing-to-a-Bulk-Sample (ReBuS), for phase-resolved measurements of fast third-order optical nonlinearities in waveguides and bulk samples is proposed, built, and demonstrated. For this, dispersion properties of the sample under test have to be known. The configuration proposed here allows to characterize the nonlinearities without the need to know the laser parameters, such as incident peak amplitudes of the excitation fields or pulse shape. The observed nonlinearities are directly compared to an additional (reference) sample with well characterized optical properties. The nonlinear refractive index n_2 and the nonlinear photon absorption coefficient β are simultaneously detected. The simultaneous measurement of these parameters allows deduction of the nonlinear figure-of-merit (NFOM), which is a key criterion for selecting a suitable material for all-photonics applications.

The measurements are performed by combining a nearly degenerate FWM process with heterodyne technique. In the nearly degenerate FWM the involved fields are phase-matched due to fact that they have practically the same optical frequencies. The excitation fields co-propagate and this collinear geometry is suitable for investigation of optical nonlinearities in waveguides. The heterodyning facilitates the discrimination of the FWM signal against the excitation fields and phase-resolved signal detection. Both quadrature components are calibrated using the fact that the optical properties of the reference sample are known. In addition, heterodyne technique helps to detect mixing products that are many orders of amplitude weaker than its excitation fields. A technique for elimination of the concurrent parasitic signal arising from the photodiode is developed. Using this technique, the parasitic signal is suppressed and it enables to investigate of samples with mixing products that have 120 dB smaller power than the excitation signals.

Excitation fields and local oscillator are generated by the same laser source by slightly shifting the central frequency of the laser using acousto-optical modulators (tens of MHz). Due to the fact that the local oscillator is generated from the same source as the excitation fields, the fluctuations of the optical carrier frequency are cancelled out. Both quadrature

components of the beat note between the local oscillator and FWM field are phase-sensitively recorded using a lock-in amplifier. The reference signal to the lock-in is generated ‘all-optically’ using a photodiode and a double balanced mixer that mixes, after suitable filtering, the beat notes between the excitation and local oscillator fields. It leads to an efficient common-mode-rejection of interferometric noise, since the reference signal undergoes the same phase perturbations as the measurement signal.

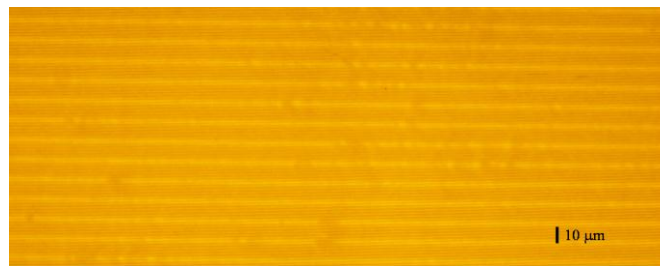
The bulk sample is located behind the waveguide in the vicinity of the focal plane using a 1:1 imaging system. Putting the bulk behind the waveguide ensures the same beam profile in both samples. The value of the overall FWM signal varies depending on the longitudinal position of the bulk in respect to the focus. Two measurements are required for determination of the optical nonlinearity of the sample under test: one is when the bulk is located at the focal plane of the waveguide’s output and contributes noticeably to the overall FWM field and the other one is when the bulk is far from the focal plane and hence the nonlinear contribution from the bulk is negligible. A length of the waveguide should be short enough to neglect dispersion. Otherwise, pulse duration at the waveguide’s input and output has to be known.

The concept developed here allows measurements of fast optical nonlinearities of the third-order in short waveguiding samples and is demonstrated for short pieces of SMF-28 and hollow-core photonic crystal fibers (lengths of 10 mm - 20 mm). The concept allows for simultaneous measurement of n_2 and β (and hence the nonlinear figure-of-merit) in different kinds of photonic devices.

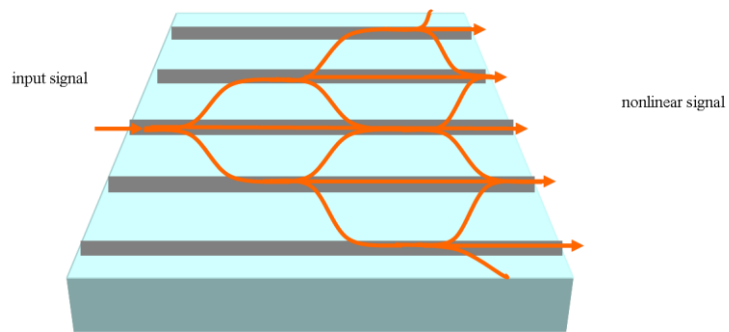
Outlook

Generally, ReBuS combined with the nearly degenerate FWM scheme and heterodyne detection can be applied for phase-resolved investigation of the nonlinear properties in different kinds of nonlinear photonic devices, e.g. routers and short waveguiding devices. Therefore, the tool developed in this work can greatly facilitate towards characterization and calibration of nonlinear properties of photonic devices.

One example for an application of the tool is a study of the nonlinear properties of a waveguide array sample. The sample includes several waveguides (array) that are parallel to each other. A part of the array and a schematic drawing of the coupling mechanism between the waveguides is shown in Fig. 6.1. The sample has been recently delivered as a part of a collaboration with the group of Prof. S. Cundiff (JILA, USA). The waveguides in the array are single-mode and fabricated from AlGaAs material [Huds08], having a size of $3\ \mu\text{m} \times 2\ \mu\text{m} \times 10\ \text{mm}$ (width, height, length) and the distance between the waveguides is $12\ \mu\text{m}$. It is interesting to study the nonlinear coupling mechanism between the waveguides. For this purpose, the excitation fields at frequencies ν_1, ν_2 (the compact setup is shown in Fig. 5.1) are launched into the waveguide and the nonlinearities, e.g. refractive index of the waveguide, can be determined as explained in this work (Fig. 6.2a). Due to the nearly degenerate FWM scheme, the nonlinear signal is discriminated against the excitation signals so that the nonlinear optical properties of the neighbouring waveguides can be investigated simultaneously (Fig. 6.2b). This allows to detect self- and cross-NFOMs. According to reference [Huds08], the nonlinear coupling coefficient changes as a function of the input optical power, i.e. nonlinear refractive index is intensity dependent ($n_2 + \Delta n_2 I$). Using tool developed in this work, heterodyning, and ReBuS, this higher order nonlinearity (corresponding to $\chi^{(5)}$) can be studied by detecting the beat note at $(3\nu_1 - 2\nu_2) - \nu_{\text{LO}}$. This can be done by a slight modification of the setup and allows the simultaneous detection under the same experimental circumstances of the nonlinearities due to $\chi^{(3)}$ and $\chi^{(5)}$ processes. From these measurements, the cascaded $\chi^{(3)}$ processes and $\chi^{(5)}$ processes can be studied separately.



(a)



(b)

Fig. 6.1. (a) A part of the waveguide array (top view, taken by CCD camera). (b) Schematic draw of the coupling mechanism between the waveguides. According reference [Huds08], the value of the coupling coefficients between the waveguide change depending on the input power.

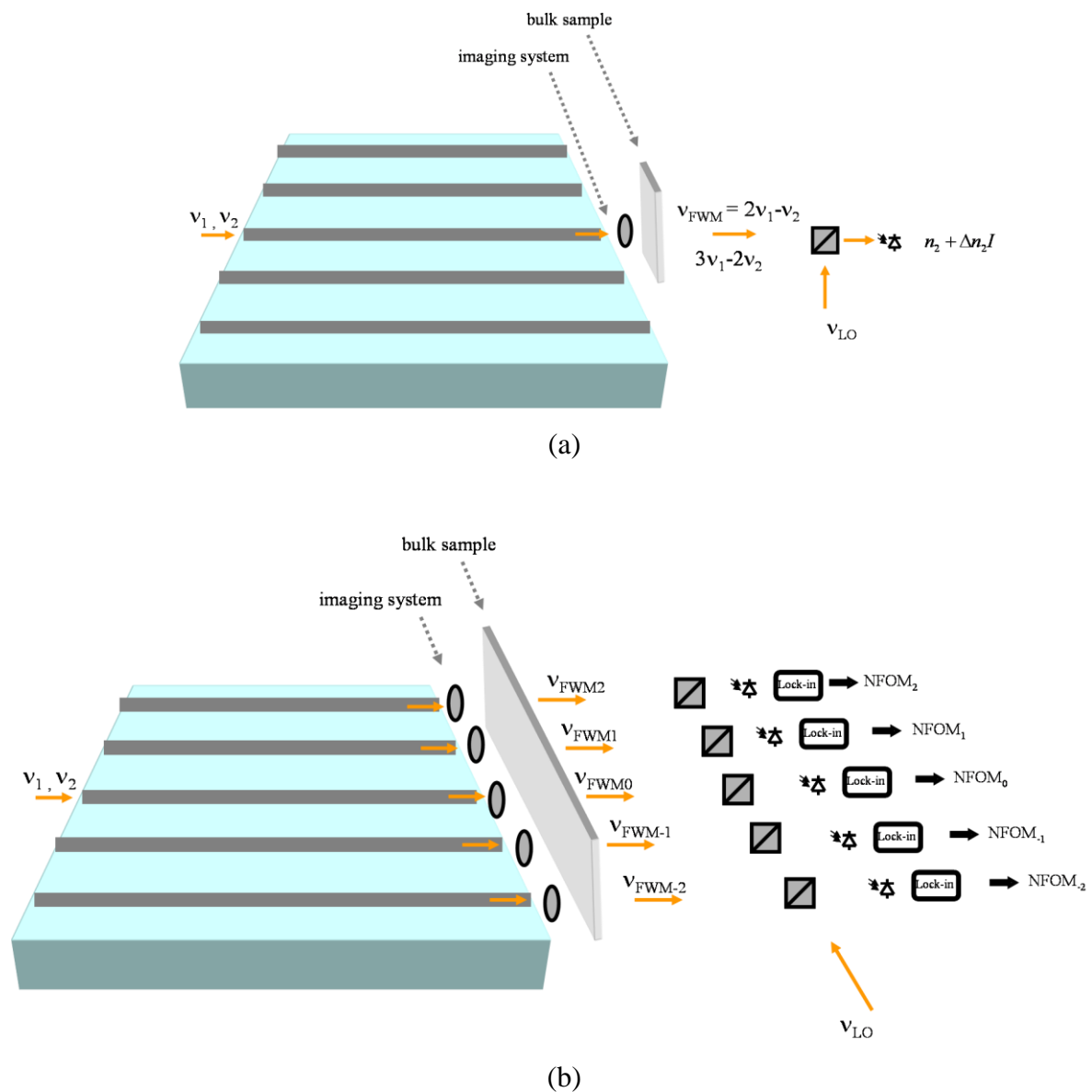


Fig. 6.2. (a) Compact experimental setup for investigation of optical nonlinearity in one of the waveguides in the array. The nonlinear coupling coefficient changes as a function of the input optical power and hence the nonlinear refractive index is intensity dependent ($n_2 + \Delta n_2 I$). It is interesting to study this higher order nonlinearity. (b) Compact experimental setup for investigation of optical nonlinearities in the array. Due to the fact that the nonlinear signal is distinguishable from the excitation signals, the nonlinear properties (e.g. NFOM) and the coupling mechanism between the waveguides can be studied.

References

- [Agra89] G. P. Agrawal, “Nonlinear Fiber Optics”, Academic Press, (1989)
- [Alme04] V. R. Almeida, C. A. Barrios, R. R. Panepucci, and M. Lipson, “All-optical control of light on a silicon chip”, *Nature* **431**, 1081-1084, (2004)
- [Argy06] A. Argyros, M. A. van Eijkelenborg, M. C. Large, and I. M. Bassett, “Hollow-core microstructured polymer optical fiber”, *Opt. Lett.* **31**, 172-174, (2006)
- [Arms62] J. A. Armstrong, N. Bloembergen, J. Ducuing, and P. S. Pershan, “Interactions between light waves in a nonlinear dielectric”, *Phys. Rev.* **127**, 1918-1939, (1962)
- [Bhag08] A. R. Bhagwat, and A. L. Gaeta, “Nonlinear optics in hollow-core photonic bandgap fibers”, *Opt. Express* **16**, 5035-5047, (2008)
- [Bjor75] G. Bjorklund, “Effects of focusing on third-order nonlinear processes in isotropic media”, *IEEE J. Quantum Electron.* **11**, 287-296, (1975)
- [Bloe82] N. Bloembergen, “Nonlinear optics and spectroscopy”, *Science* **216**, 1057-1064, (1982)
- [Bloe06] D. Blömer, A. Szameit, F. Dreisow, T. Schreiber, S. Nolte, and A. Tünnermann, “Nonlinear refractive index of fs-laser-written waveguides in fused silica”, *Opt. Express* **14**, 2151-2157, (2006)
- [Borr99] P. Borri, W. Langbein, J. Mørk, and J. M. Hvam, “Heterodyne pump-probe and four-wave mixing in semiconductor optical amplifiers using balanced lock-in detection”, *Optics Comm.* **169**, 317-324, (1999)

References

[Boyd80] R. W. Boyd, “Intuitive explanation of the phase anomaly of focused light beams”, *J. Opt. Soc. Am.* **70**, 877-880, (1980)

[Boyd92] R.W. Boyd, “Nonlinear Optics”, Academic Press, (1992)

[Burk09] J. Burke, K. Wang, and A. Bramble, “Null test of an off-axis parabolic mirror. Configuration with spherical reference wave and flat return surface”, *Opt. Express* **17**, 3196-3210, (2009)

[Corn01] Product information Corning[®] SMF-28[™] optical fiber

[Cott99] D. Cotter, R. J. Manning, K. J. Blow, A. D. Ellis, A. E. Kelly, D. Nesses, I.D. Phillips, A. J. Poustie, and D. C. Rogers, “Nonlinear optics for high-speed digital information processing”, *Science* **286**, 1523-1528, (1999)

[Creg99] R. F. Cregan, B. J. Mangan, J. C. Knight, T. A. Birks, P. St. J. Russell, P. J. Roberts, and D. A. Allan, “Single-mode photonic band gap guidance of light in air”, *Science* **285**, 1537-1539, (1999)

[Dekk07] R. Dekker, N. Usechak, M. Forst, and A. Driessen, “Ultrafast nonlinear all-optical processes in silicon-on-insulator waveguides”, *J. Phys. D: Appl. Phys.* **40**, R249-R271, (2007)

[Dinu03] M. Dinu, F. Quochi, and H. Garcia, “Third-order nonlinearities in silicon at telecom wavelengths”, *Appl. Phys. Lett.* **82**, 2954-2956, (2003)

[Eckh62] G. Eckhardt, R. W. Hellwarth, F. J. McClung, S. E. Schwarz, D. Weiner, and E. J. Woodbury, “Stimulated Raman scattering from organic liquids”, *Phys. Rev. Lett.* **9**, 455-457, (1962)

[Erdo97] T. Erdogan, “Fiber grating spectra”, *J. Lightwave. Techn.* **15** (8), 1277-1294, (1997)

[Fevr09] S. Fevrier, F. Gerome, A. Labruyere, B. Beaudou, G. Humbert, and J.-L. Auguste, “Ultraviolet guiding hollow-core photonic crystal fiber”, *Opt. Lett.* **34**, 2888-2890, (2009)

References

- [Fish83] R. A. Fisher, ed., “Optical Phase Conjugation”, Academic Press, (1983)
- [Fran61] P. A. Franken, A. E. Hill, C. W. Peters, and G. Weinreich, “Generation of optical harmonics”, *Phys. Rev. Lett.* **7**, 118-119, (1961)
- [Fros06] M. H. Frosz, T. Sørensen, and O. Bang, “Nanoengineering of photonic crystal fibers for supercontinuum spectral shaping”, *J. Opt. Soc. Am. B* **23**, 1692-1699, (2006)
- [Gior65] J. A. Giordmaine and R. C. Miller, “Tunable coherent parametric oscillation in LiNbO₃ at optical frequencies”, *Phys. Rev. Lett.* **14**, 973-976, (1965)
- [Gopi04] J. T. Gopinath, M. Soljačić, E. P. Ippen, V. N. Fuflyigin, W. A. King, and M. Shurgalin, “Third order nonlinearities in Ge-As-Se-based glasses for telecommunications applications”, *Appl. Phys.* **96**, 6931-6933, (2004)
- [Grev05] M. Greve, B. Bodermann, H. R. Telle, P. Baum, and E. Riedle, “High-contrast chemical imaging with gated heterodyne coherent anti-Stokes Raman scattering microscopy”, *Appl. Phys. B* **81**, 875-879, (2005)
- [Hama01] “Technological Advances Lead to Greater Variety of Infrared Detectors”
Hamamatsu Photonics
- [Harb02] J. M. Harbold, F. Ö. Ilday, F. W. Wise, J. S. Sanghera, V. Q. Nguyen, L. B. Shaw, and I. D. Aggarwal, “Highly nonlinear As-S-Se glasses for all-optical switching”, *Opt. Lett.* **27**, 119-121, (2002)
- [Harg64] L. E. Hargrove, R. L. Fork, and M. A. Pollack, “Locking of He-Ne laser modes induced by synchronous intracavity modulation”, *Appl. Phys. Lett.* **5**, 4-5, (1964)
- [Hase73] A. Hasegawa and E. Tappert, “Transmission of stationary nonlinear optical pulses in normal dispersion”, *Appl. Phys. Lett.* **23**, 171-172, (1973)
- [Haus00] H. A. Haus, “Mode locking of lasers”, *IEEE J. Sel. Top. Quantum Electron.* **6**, 1173-1185, (2000)

References

- [Hein97] J. Hein, M. Helbig, and S. Rentsch, “Measurements of a nonlinear refractive index with a single laser pulse”, *Appl. Opt.* **36**, 1173-1176, (1997)
- [Hens07] C. J. Hensley, D. G. Ouzounov, A. L. Gaeta, N. Venkataraman, M. T. Gallagher, and K. W. Koch, “Silica-glass contribution to the effective nonlinearity of hollow-core photonic band-gap fibers”, *Opt. Express* **15**, 3507-3512, (2007)
- [Hick86] A. P. Hickman, J. A. Paisner, and W. K. Bischel, “Theory of multiwave propagation and frequency conversion in a Raman medium”, *Phys. Rev. A* **33**, 1788-1797, (1986)
- [Hofm96] M. Hofmann, S.D. Brorson, J. Mørk, and A. Mecozzi, “Time resolved four-wave mixing technique to measure the ultrafast coherent dynamics in semiconductor optical amplifiers”, *Appl. Phys. Lett.* **68**, 3236-3238, (1996)
- [Hood01] C. J. Hood, H. J. Kimble, and J. Ye, “Characterization of high-finesse mirrors: Loss, phase shifts, and mode structure in an optical cavity”, *Phys. Rev. A* **64**, 033804-033810, (2001)
- [Huds08] D. D. Hudson, K. Shish, T. R. Schibli, J. N. Kutz, D. N. Christodoulides, R. Morandotti, and S. T. Cundiff, “Nonlinear Femtosecond Pulse Reshaping in Waveguide Arrays”, *Opt. Letter* **33**, 1440-1442, (2008)
- [Humb04] G. Humbert, J. C. Knight, G. Bouwmans, P. St. J. Russell, D. P. Williams, P. J. Roberts, and B. J. Mangan, “Hollow core photonic crystal fibers for beam delivery”, *Opt. Express* **12**, 1477-1484, (2004)
- [Hund06] H. Hundertmark, “Erbium fiber laser for a frequency comb at 1560 nm”, Ph. D. thesis, Cuvillier Verlag Göttingen, (2006)
- [Isla87] M. N. Islam, L. F. Mollenauer, R. H. Stolen, J. R. Simpson, and H.-T. Shang, “Cross-phase modulation in optical fibers”, *Opt. Lett.* **12**, 625-627, (1987)
- [Kaoh66] C. K. Kao and G. A. Hockham, “Dielectric fiber surface waveguides for optical frequencies”, *Proc. IEE* **113**, 1151-1151, (1966)

References

- [Kapr70] F. P. Kapron, D. B. Keck, and R. D. Maurer, “Radiation losses in glass optical waveguides”, *Appl. Phys. Lett.* **17**, 423-423, (1970)
- [Kato95] T. Kato, Y. Suetsugu, M. Takagi, E. Sasaoka, and M. Nishimura, “Measurement of the nonlinear refractive index in optical fiber by the cross-phase-modulation method with depolarized pump light”, *Opt. Lett.* **20**, 988-990, (1995)
- [Knig98] J. C. Knight, J. Broeng, T. A. Birks, and P. St. J. Russell, “Photonic band gap guidance in optical fibers”, *Science* **282**, 1476-1478, (1998)
- [Koos09] C. Koos, P. Vorreau, T. Vallaitis, P. Dumon, W. Bogaerts, R. Baets, B. Esembeson, I. Biaggio, T. Michinobu, F. Diederich, W. Freude, and J. Leuthold, “All-optical high-speed signal processing with silicon-organic hybrid slot waveguides”, *Nature Photonics* **3**, 216-219, (2009)
- [Lamb64] W. E. Lamb, “Theory of an optical laser”, *Phys. Rev.* **134**, A1429-A1450, (1964)
- [Lenz00] G. Lenz, J. Zimmermann, T. Katsufuji, M. E. Lines, H. Y. Hwang, S. Spälter, R. E. Slusher, S.-W. Cheong, J. S. Sanghera, and I. D. Aggarwal, “Large Kerr effect in bulk Se-based chalcogenide glasses”, *Opt. Lett.* **25**, 254-256, (2000)
- [Linz07] Q. Lin, J. Zhang, G. Piredda, R. W. Boyd, P. M. Fauchet, and G. P. Agrawal, “Dispersion of silicon nonlinearities in the near infrared region”, *Appl. Phys. Lett.* **91**, 021111-021113, (2007)
- [Lour99] F. Louradour, E. Lopez-Lago, V. Couderc, V. Messager, and A. Barthelemy, “Dispersive-scan measurement of the fast component of the third-order nonlinearity of bulk materials and waveguides”, *Opt. Lett.* **24**, 1361-1363, (1999)
- [Maim60] T. H. Maiman, “Stimulated optical radiation in Ruby”, *Nature* **187**, 493-494, (1960)
- [Mali65] I. H. Malitson, “Interspecimen comparison of the refractive index of fused silica”, *J. Opt. Soc. Am.* **55**, 1205-1208, (1965)

References

- [Malo98] C. Malouin, A. Villeneuve, G. Vitrant, P. Cottin, and R. A. Lessard, “Degenerate four-wave mixing for characterization of thin-film waveguides”, *J. Opt. Soc. Am. B* **15**, 826-837, (1998)
- [Mand66] L. Mandel, “Heterodyne detection of a weak light beam”, *J. Opt. Soc. Am.* **56**, 1200-1204, (1966)
- [Mats86] H. Matsumoto, “Synthetic interferometric distance-measuring system using a CO₂ laser”, *Appl. Opt.* **25**, 493-498, (1986)
- [Mear87] R. J. Mears, L. Reekie, I. M. Jauncey, and D. N. Payne, “Low-noise erbium-doped fibre amplifier operating at 1.54 μm ”, *Electron. Lett.* **23**, 1026-1028, (1987)
- [Mila98] D. Milam, “Review and assessment of measured values of the nonlinear refractive-index coefficient of fused silica”, *Appl. Opt.* **37**, 546-550, (1998)
- [Miya79] T. Miya, Y. Terunuma, T. Hosaka, and T. Miyashita, “Ultimate low-loss single-mode fiber at 1.55 μm ”, *Electron. Lett.* **15**, 106-108, (1979)
- [Mora75] M. J. Moran, C. Y. She, and R. L. Carmen, “Interferometric measurements of the nonlinear refractive index coefficient relative to CS₂ in the laser system related materials”, *IEEE J. Quantum Electron.* **11**, 259-263, (1975)
- [Nktp01] Datasheet: hollow-core photonic crystal fiber HC-1550-02 (NKT Photonics.)
- [Nktp02] Datasheet: hollow-core photonic crystal fiber HC-1550-01 (NKT Photonics.)
- [Nunz91] J. M. Nunzi and F. Charra, “Complex third-order phase conjugation nonlinearity of polymeric thin films”, *Appl. Phys. Lett.* **59**, 13-15, (1991)
- [Ouzo03] D. G. Ouzounov, F. R. Ahmad, D. Muller, N. Venkataraman, M. T. Gallagher, M. G. Thomas, J. Silcox, K. W. Koch, and A. L. Gaeta, “Generation of megawatt optical solitons in hollow-core photonic band-gap fibers”, *Science* **301**, 1702-1704, (2003)

References

- [Payn74] D. N. Payne and W. A. Gambling, “New silica-based low-loss optical fibre”, *Electron. Lett.* **10**, 289-290, (1974)
- [Qxus05] Q. Xu, B. Shmidt, S. Pradhan, and M. Lipson, “Micrometre-scale silicon electro-optic modulator”, *Nature* **435**, 325-327, (2005)
- [Rams09] D. Ramsey “Closing the Gap Between High-Speed Data Transmission and Processing”, DARPA, San Diego <http://ucsdnews.ucsd.edu/newsrel/science/01-09ClosingTheGap.asp>, (2009)
- [Renn99] M. J. Renn, R. Pastel, and H. J. Lewandowski, “Laser guidance and trapping of mesoscale particles in hollow-core optical fibers”, *Phys. Rev. Lett.* **82**, 1574-1577, (1999)
- [Rita04] T. Ritari, J. Tuominen, H. Ludvigsen, J. C. Petersen, T. Sørensen, T. P. Hansen, and H.R. Simonsen, “Gas sensing using airguiding photonic bandgap fibers”, *Opt. Express* **12**, 4080-4087, (2004)
- [Rubi38] A. Rubinowicz, “On the anomalous propagation of phase in the focus”, *Phys. Rev.* **54**, 931-936, (1938)
- [Russ03] P. Russell, “Photonic crystal fibers”, *Science* **299**, 358-362, (2003)
- [Russ06] P. St. J. Russell, “Photonic crystal fibers”, *J. Lightwave. Technol.* **24**, 4729-4749, (2006)
- [Sait04] K. Saitoh, N. A. Mortensen, and M. Koshiba, “Air-core photonic band-gap fibers: the impact of surface modes”, *Opt. Express* **12**, 394-400, (2004)
- [Sami10] P. Samineni, Z. Perret, W. S. Warren, and M. C. Fischer, “Measurements of nonlinear refractive index in scattering media”, *Opt. Express* **18**, 12727-12735, (2010)
- [Sarg94] L. Sarger, P. Segonds, L. Canioni, F. Adamietz, A. Ducasse, C. Duchesne, E. Fargin, R. Olazcuaga, and G. Le Flem, “Time-resolved absolute interferometric measurement of third-order nonlinear-optical susceptibilities”, *J. Opt. Soc. Am. B* **11**, 995-999, (1994)

References

- [Savc07] A. A. Savchenkov, A. B. Matsko, V. S. Ilchenko, and L. Maleki, “Optical resonators with ten million finesse”, *Opt. Express* **15**, 6768-6773, (2007)
- [Shei89] M. Sheik-Bahae, A. A. Said, and E. W. Van Stryland, “High sensitivity, single beam n_2 measurements”, *Opt. Lett.* **14**, 955-957, (1989)
- [Sher09] A. Sherman, E. Benkler, and H. R. Telle, “Small third-order optical nonlinearities detection free of laser parameters”, *Opt. Lett.* **34**, 49-51, (2009)
- [Sher10] A. Sherman, E. Benkler, and H. R. Telle, “A sensitive method for measurements of complex third-order susceptibilities in waveguides”, *Appl. Phys. B* **98**, 653-657, (2010)
- [Sieg63] A. E. Siegman, S. E. Harris, and B. J. McMurtry, “Optical heterodyning and optical demodulation at microwave frequencies”, J. Fox, ed., John Wiley & Sons, New York, (1963)
- [Smit03] C. M. Smith, N. Venkataraman, M. T. Gallagher, D. Muller, J. A. West, N. F. Borrelli, D. C. Allan, and K. Koch, “Low-loss hollow-core silica/air photonic bandgap fibre”, *Nature* **424**, 657-659, (2003)
- [Song10] Song-J. Im, A. Husakou, and J. Herrmann, “High-power soliton-induced supercontinuum generation and tunable sub-10-fs VUV pulses from kagome-lattice HC-PCFs”, *Opt. Express* **18**, 5367-5374, (2010)
- [Sore06] R. A. Soref, “The past, present, and future of silicon photonics”, *IEEE J. Sel. Top. Quantum Electron.* **12**, 1678-1687, (2006)
- [Steg89] G. I. Stegeman and R. H. Stolen, “Waveguides and fibers for nonlinear optics”, *J. Opt. Soc. Am. B* **6**, 652-662, (1989)
- [Stol78] R. H. Stolen and C. Lin, “Self-phase-modulation in silica optical fibers”, *Phys. Rev. A* **17**, 1448-1453, (1978)
- [Stol82] R. H. Stolen and J. Bjorkholm, “Parametric amplification and frequency conversion in optical fibers”, *IEEE J. Quantum Electron.* **18**, 1062-1072, (1982)

References

- [Suth96] R. L. Sutherland, “Handbook of Nonlinear Optics”, Marcel Dekker, Inc., (1996)
- [Tamu93] K. Tamura, E.P. Ippen, H.A. Haus, and L.E. Nelson, “77-fs pulse generation from a stretched-pulse mode-locked all-fiber ring laser”, *Opt. Lett.* **18**, 1080-1082, (1993)
- [Terh62] R. W. Terhune, P.D. Maker, and C. M. Savage, “Optical harmonic generation in calcite”, *Phys. Rev. Lett.* **8**, 404-406, (1962)
- [Thie01] C. W. Thiel, “Four-wave mixing and its applications”, www.physics.montana.edu/students/thiel/docs/FWMixing.pdf
- [Thor01] Product Specification Sheet of the photodiodes
- [Tsan02] H. K. Tsang, C. S. Wong, T. K. Liang, I. E. Day, S. W. Roberts, A. Harpin, J. Drake, and M. Asghari, “Optical dispersion, two-photon absorption and self-phase modulation in silicon waveguides at 1.5 μm wavelength”, *Appl. Phys. Lett.* **80**, 416-419, (2002)
- [Vinc09] L. Vincetti, “Hollow core photonic band gap fiber for THz applications”, *Microwave and Optical Technol. Lett.* **51**, 1711-1714, (2009)
- [Ward69] J. F. Ward and G. H. C. New, “Optical third harmonic generation in gases by a focused laser beam”, *Phys. Rev.* **185**, 57-72, (1969)
- [Webe78] M. J. Weber, D. Milam, and W. L. Smith, “Nonlinear refractive index of glasses and crystals”, *Opt. Eng.* **17**, 463-469, (1978)
- [West04] J. A. West, C. M. Smith, N. F. Borrelli, D. C. Allan, and K. W. Koch, “Surface modes in aircore photonic band-gap fibers”, *Opt. Express* **12**, 1485-1495, (2004)
- [Witz10] J. Witzens, T. Baehr-Jones, and M. Hochberg, “Silicon photonics: On-chip OPOs”, *Nature Photonics* **4**, 10-12, (2010)

References

[Yari96] A. Yariv, “Optical electronics in modern communications”, Oxford University Press, Fifth edition, (1996)

[Ytai04] C.-Y. Tai, J. S. Wilkinson, N. M. B. Perney, M. C. Netti, F. Cattaneo, C. E. Finlayson, and J. J. Baumberg, “Determination of nonlinear refractive index in a Ta₂O₅ rib waveguide using self-phase modulation”, *Opt. Express* **12**, 5110-5116, (2004)

Danksagung

Im Laufe meiner Promotion habe ich freundlicherweise von vielen Seiten aktive Unterstützung bekommen.

Mein besonderer Dank gilt Prof. Dr. Uwe Morgner für die unkomplizierte und sehr freundliche Weise, meine Arbeit zu betreuen. Seine jederzeit bereitwillige Unterstützung und Zuvorkommenheit während der ganzen Promotion haben mir enorm geholfen.

Ganz herzlich möchte ich mich bei Prof. Dr. Piet Schmidt für die sehr nette, problemlose und schnelle Übernahme des Koreferats bedanken.

Schönen Dank an Prof. Dr. Rolf Haug für seine Hilfe bei auftretenden Fragen und Unklarheiten.

Mein aufrichtiges Dankeschön verbunden mit viel Respekt möchte ich dem Fachbereichsleiter, Hon.-Prof. Dr. Stefan Kück, für die hervorragende persönliche Begleitung sagen. Seine immer aktive Unterstützung und Diskussionsbereitschaft haben mir ermöglicht, meine Arbeit in Ruhe anzufertigen.

Meinen Kollegen in der Arbeitsgruppe 4.53 danke ich für nachhaltig fruchtbare und aufschlussreiche wissenschaftliche Diskussionen sowie angenehmes Arbeitsklima. Mein ganz besonderer Dank gilt Dr. Harald Telle für den intensiven täglichen Gedankenaustausch und für den wissenschaftlichen und persönlichen Rat. Meinen herzlichen Dank geht an Dr. Erik Benkler für viele hilfreiche und produktive Vorschläge und wissenschaftliche Diskussionen sowie tatkräftige Unterstützung und Hilfe, besonders am Anfang meiner Akklimatisationsphase in Deutschland. Vielen Dank an Christoph Böker für interessante wissenschaftliche und nichtwissenschaftliche Diskussionen, Offenheit und Lachen.

Lieben Dank geht an die ganze Abteilung Optik der PTB für die Freundlichkeit und Zuvorkommenheit. Insbesondere danke ich Mark Rodenberger für die Englischkorrektur und Holger Lecher für die technische Unterstützung.

Frau Hünitzsch danke ich für die administrative Unterstützung.

Ich danke dem SFB 407 im Rahmen der DFG und der PTB für die bestmöglichen Bedingungen zur Anfertigung dieser Doktor-Thesis.

Dashush, für ihren Beistand und ihre Geduld, insbesondere in der letzten Phase meiner Arbeit.

Herzlichen Dank sage ich meinem lieben Bruder, Gena, der immer bereit ist, mir zu helfen!

Und zuletzt, aber am allerwichtigsten bedanke ich mich ganz herzlich bei meinen Eltern!

Allen weiteren namentlich nicht Genannten danke ich ebenfalls für die fachliche und emotionale Unterstützung, welche zur Vollendung meiner Thesis geführt hat.

CURRICULUM VITAE

Education

- 04/2007-present: Ph.D. candidate – Faculty of Mathematics and Physics
University of Hanover (LUH), Germany
- 03/2004-03/2007: M.Sc. in Electrical Engineering ('with thesis')
Technion, Haifa, Israel
- 03/1999-01/2003: B.Sc. in Electrical Engineering (regular period of study: 4 years)
Technion, Haifa, Israel
- 09/1992-09/1995: Bagrut (Matura) – Misgav High School
Mitzpe-Ramon, Israel
- 09/1985-09/1992: School number 17
Beltsy, Moldova

Work Experience

- 04/2007-present: Scientific employee – Optical Femtosecond-Metrology Group
German National Metrology Institute, PTB-Braunschweig, Germany
- 11/2004-03/2007: Scientific employee – Electrical Engineering Department
Technion, Haifa, Israel
- 10/2006-12/2006: Guest scientist – Nonlinear Photonics Group
NRW-Bursary Program, University of Münster, Germany
- 02/2001-10/2004: Researcher – On-chip T-lines Group
IBM R&D Labs, Haifa, Israel
- 03/1996-03/1999: Active service in Israel Defense Forces
- 10/1995-03/1996: Boarding school counselor
Mitzpe-Ramon, Israel

Languages German, English, Russian, Hebrew